RF and Electronic Design Perspective on Ultra-High Field MRI systems

A DISSERTATION
SUBMITTED TO THE FACULTY OF THE GRADUATE SCHOOL
OF THE UNIVERSITY OF MINNESOTA
BY

SUNG-MIN SOHN

IN PARTIAL FULFILLMENT OF THE REQUIREMENTS
FOR THE DEGREE OF
DOCTOR OF PHILOSOPHY

Anand Gopinath, Ph.D

February 2013

Acknowledgements

I would like to acknowledge Prof. Gopinath, Anand for his continuous advising and guidance as my advisor during the time of my Ph.D student and I would also like to express my sincere gratitude to Prof. J. Thomas Vaughan for supporting and giving me the opportunity to work in CMRR.

Since I came here, it has been five and half years. During my Ph.D student life, I met many people and learned a lot from them. This study would have not been possible without the help and support of Dr. Lance DelaBarre. I think what I have learned from the discussion with him would be a great source of motivation and inspiration to perform this project. Throughout my laboratory work and tests, he has been with me. I still hold on to the happy memory of works with Dr. Can eyup akgun, and I am grateful to soon-to-be Dr. Carl Snyder for helping me.

Finally, I have to thank my lovely family: My wife Sunyoung Park, my daughter Yejin Sohn, and my parents living in Korea. I love you all. This dissertation is dedicated to you.

사랑하는 가족에게 이 논문을 바칩니다...

Abstract

Magnetic Resonance Imaging (MRI) is one of the most sophisticated technologies to produce detailed images of the human body's organs and structures. There were many items of pioneering work in MRI over the last few decades. However, many challenges still remain.

This dissertation includes two studies concerning the challenges: the fully automatic matched / tuned RF head coil design and RF coil design with improved B_1 field uniformity. Both have been being considered as critical problems at ultra-high field (7T and beyond) MRI systems.

The first study aims to build a real-time, high-speed, electrically controlled, and fully stand-alone system of the impedance matched / frequency tuned RF coil that is applicable and compatible to an existing MRI system. To achieve this project, subjects including the basic background of Nuclear Magnetic Resonance (NMR) physics, MRI systems, RF/analog circuit theory. have been studied and presented in this dissertation. The 8-channel RF head coil was successfully built and tested. The fully automatic tuning and matching RF coil offers fast operation (less than 550ms per each channel), accurate impedance matching / frequency tuning (less than -20dB in the reflected coefficient, S_{11}, at the Larmor frequency) resulting in the high power efficiency (4%~21% improved at each channel), and higher Signal-to-Noise Ratio (SNR) in MR images (about 3% in the whole object region).

In the second study, the double trapezoidal-like shape along the length of the microstrip resonator is proposed to obtain the gradual impedance variation and flatten the near field distributions. The conventional and proposed 8-channel volume coils have been built and investigated with a phantom in 7T MRI scanner. The results show successful flat field distributions with about 35% increased local transmission magnetic field strength at the ends of the RF coil as well as about 13% improvement at its center. The quality factor ratio between unloaded and loaded is also increased about 45% (from 1.46 to 2.13) compared to the conventional structure.

The proposed and demonstrated approaches are a meaningful step in order to overcome difficulties at ultra-high field MRI systems, and one critical contribution to the area.

Table of Contents

List of Tables

List of Figures

Chapter 1. **Introduction**

1.1 The recent trend of RF design for MRI

Magnetic Resonance Imaging (MRI) is a modern and versatile device to obtain the best information about the anthropotomy in the medical imaging domain that can be obtained with the existing diagnostic medical devices, e.g. X-ray, CT (Computed Tomography), and ultrasound scanner. There were many items of pioneering work in MRI over the last few decades [1-4]. Among the various developments, although most are complicatedly interwoven with each other, three dominate: high image quality, fast image acquisition, and improving the MRI in RF (Radio Frequency) / electrical performance.

Figure 1-1 shows simple diagrams to understand MRI systems. From RF and electronic devices perspective, the hardware engineering of the MRI is conceptually similar to a device using RF wireless technology to carry signals such as voice, text, music, or pictures between two points. In the same manner, RF circuits and systems in MRI send RF signals into the human body and receive RF signals through the RF coil (commonly, the antenna is called RF coil in the MRI domain), and then the MRI system generates MR images using received RF signals.

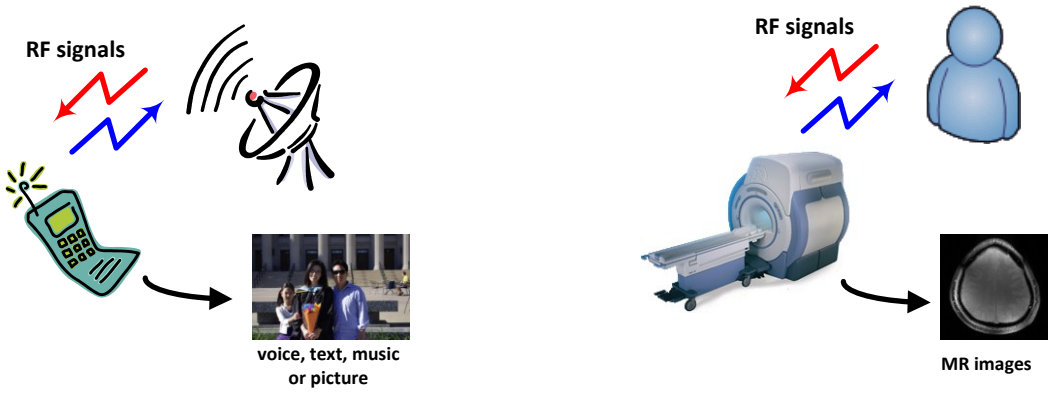

Figure 1-1. Simple diagrams to show the role of (a) wireless handset device and (b) MRI scanner

The current trend in MRIs is the move to higher static magnetic field strength, B_0, (e.g. 1 Tesla = 10,000 Gauss and the gravity = about 0.5Guass) [2,5-7]. The traditional clinical 1.5T magnets are being replaced by 3T in hospitals for diagnostic and clinical purposes. In addition, 7T, 9.4T, and 11.74T (called ultra-high fields) systems are developing and being used for animal or human images because of higher signal-to-noise ratios (SNR) which can be used to improve the spatial resolution and contrast in MR image quality. It correlates in linear fashion with the field strength and is roughly twice as great at 3T as at 1.5T. In ultra-high fields, 7T is widely used for research with approximately 40 of these systems installed currently in the world. Above this, four 9.4T systems exist, and one 11.7T, 68cm bore (head only) system is being installed at the National Institutes of Health (NIH), while whole body a 10.5T is being installed at the University of Minnesota Center for Magnetic Resonance Research (CMRR), and 11.7T is being installed at the Atomic Energy Commission (CEA) in France. The clinical ability and promise in ultra-high field MRI systems have already begun to be exploited in human body studies. However, there are substantial engineering challenges.

The next trend is the fast MR image using parallel imaging [8,9] combined with the signals of several coil elements in a phased array to reconstruct MR images. Parallel imaging technique also offers a better SNR because each element of multi-channel RF coil is sensitive to a specific region of the entire field of view (FOV) and associated with a dedicated RF front-end channel whose output is processed and combined with the separate outputs of the other channels with the signals acquired by the other coil elements. Multi transmit and receive can compensate shorter wavelength effect and optimize the distribution of RF signal because a small dimension of RF coil has lower coil loss. Parallel imaging of MRI systems utilizes the multiple channels of a phased array coil system. The signal chains of multi-channel RF front-end and optimal pulse coding of parallel imaging have been being combined to complete the entire parallel MR imaging system which has benefited from the cooperation between hardware and software. In this aspect of RF design of parallel imaging, the complexity of RF front-end design is interconnected with the number of multiple channels.

The other recent trend of MRI systems are the various electronic approaches for implementing versatile systems including power monitoring RF/circuits, wireless MR signal transmission, on-coil power amplifier, automatic impedance tune/match for better image quality and fast image acquisition [10-14]. The complexity and the number of RF front-end components are increased, and the system integration is now under way to improve image quality with fast image acquisition and to reduce the dimension of RF coil structure for assuring patient's comfort as higher multi-channel applications become more popular. For example, Philips (one of the major MRI companies) recently announced the dStream that manipulates the signal chain integration from low noise pre-amplifier to analog-to-digital converter (ADC) into the RF coil using the integrated and miniaturized circuitry to get better image quality, faster image processing results in higher patient throughput [13]. In hardware engineering, the most significant engineering challenge caused by the first trend (ultra-high fields) is shorter wavelength issue. The wavelength for MR operation is smaller than the dimension of objects being scanned since higher magnetic strength needs higher operating frequency. Another challenge caused by the second trend (parallel imaging) is the complex circuits in supporting multiple RF transmit and receive chains. In addition, various demands for particular functions are increased as MR devices become commercialized. Recently, some researchers and institutes try to find solutions by using electronic approaches, such as electrically RF/analog signal control and the integrating of circuits. Another benefit from the electronic approach is the integration of MRI systems. Although the size of magnet is a burden, NMR equipment for analyzing chemical material components is remarkably miniaturized, and the integration of RF circuits / systems contributes as the system integration.

1.2 Motivation

In the aforementioned trends, MR imaging at higher strength of magnetic fields and fast image acquisition using multi-channel of parallel imaging present certain challenges in RF coil circuit design.

The radio frequency (RF) coil (antenna-like) is an essential part of hardware in MRI systems and the microstrip transmission line (TEM) RF coils have been used for high-fields applications to excite and receive the nuclear magnetic resonance signals in the subject. These coils are typically terminated by capacitors. On one end two variable capacitors, the matching capacitor (Cm) and tuning capacitor (Ct), and on the other end a fixed value capacitor (Cf) form a capacitively tuned, matched, and foreshortened half-wave resonator. These RF coils elements usually have narrow bandwidth due to their high quality factors (Qs) associated with coil's performance. Resonant structures have an inevitable characteristic, loading (body) effects causing detuning. Broadband design reduces the loading (body) effect to the minimum, but it is not suitable for RF coil of MRI applications because MR images are obtained at defined frequencies by Larmor frequency formula and high Q resonant element increases the magnetic field by a factor Q for the same input power. In general, the loaded resonance frequency is shifted 1~3%, and 5~20% power loss is produced when the human body is loaded into the RF coils. Such variation depends on the shapes, sizes and tissue components of the human body, and it is hard to estimate the variations accurately. High transmit power efficiency and signal-to-noise (SNR) in the receiver are dependent on a well-tuned and matched coil element to the human body. Conversely, variable body loading of these coil elements can adversely impact both tuning and matching associated with power efficiency, and SNR of transmit/receive signals. In other words, loading (body) effects are problematic, and manual tuning is a time-consuming adjustment that needs a few minutes per channel. It, however, is the only method to avoid loading problems at present. Consequently, this problem is a critical drawback in higher field strength systems and the larger number of channels of the RF coil. This study focuses on the development and verification of a high-speed, electronically switched, automatic impedance matching and frequency tuning technique for optimal coil efficiency and SNR over a range of patient coil loading conditions.

Additionally, another obstacle at high fields is that RF wavelengths become shorter than the dimensions of the object to be imaged. This leads to significant B_1 (magnetic field component of the RF field) distortions, which are dependent on tissue

electromagnetic properties and geometry. Although several approaches for overcoming this obstacle have been suggested, it is hard to compensate for the disproportion of current-carrying elements based on the geometric and structural problem of RF coil. In this dissertation, a new approach for reducing the inhomogeneity of B_1 distribution was also studied and evaluated.

1.3 Objectives and scope of this dissertation

This dissertation aims to research and develop new approaches for resolving the problems in ultra-high magnetic field applications. Among critical problems, loading (body) effect and B1 field inhomogeneity have been chosen for this dissertation because both are still obstacles in ultra-high field MRI systems to meet the demands of the recent trends of RF / electronics for MRI systems. Merits and demerits of ultra-high fields of magnetic resonance imaging have been being studied, and novel approaches have been proposed and evaluated to overcome loading (body) effect and B1 field inhomogeneity of ultra-high magnetic fields. In this dissertation, automatic tuning and matching circuits have been proposed to eliminate loading (body) effect, and the double trapezoidal microstrip TEM resonator has been proposed to improve B_1 local field uniformity.

The system of magnetic resonance imaging is a complex device encompassing a wide range of subjects, e.g. the basic physics and chemistry, electrical and computer engineering as well as mathematics, mechanics, and medical science. The scope of this dissertation is RF and electronic approaches in the electrical domain to solve the challenges in ultra-high fields of loading (body) effects and local B_1 field inhomogeneity of RF coils design. Electrically controlled auto-tune/match device has been proposed, designed, and verified in 7T MRI machine, and every RF/electronic component has been built with the microstrip resonators. In addition, a modified microstrip TEM resonator has been proposed to obtain uniformity of B_1 local fields and compared with the existing conventional structure.

Novel concepts, circuits, electromagnetic simulations, design, fabrication, and evaluation have been supported and accomplished in the department of Electrical and

Computer engineering and CMRR (Center for magnetic resonance research) of University of Minnesota for this dissertation.

1.4 Dissertation organization

This dissertation is organized in six chapters discussing the projects. Most of this dissertation covers practical designs in order to build new ideas and verify their performance.

Chapter 1 describes the introduction of this dissertation. Motivation and objective are also presented.

Chapter 2 briefly explains the principles of a MRI system for this study to understand the relationship between NMR basic phenomenon and the purpose of RF circuits.

Chapter 3 introduces RF and electrical issues that occur in ultra-high fields MRI systems. Two projects associated with these issues are selected for this dissertation.

Chapter 4 demonstrates the design procedures to build multi-channel RF head coil with automatic impedance matching and frequency tuning. In the first part, RF systems of MRI and the impedance matching network are discussed, and the Pi matching network for RF coils is proposed. The middle of this chapter explains the basic knowledge to understand RF concepts of the RF coil of MRI systems and the results of the circuit and electromagnetic simulation are shown to validate the hardware design. The design and results of 8-channel head coil with automatic tune/match are discussed after each part of hardware components is described. In addition, some design issues are presented in the last part of this chapter.

Chapter 5 provides the implementation of the electromagnetic simulation for modeling of a new microstrip resonator based on TEM element design to reduce the effect of B1 local field inhomogeneity.

Finally, Chapter 6 summarizes the achievements of this dissertation and presents some areas for future work.

Chapter 2. **Principles of MRI**

This chapter reviews the principles and basic concepts of MRI in order to understand the relationship between RF/analog circuits and the nuclear magnetic resonance (NMR) phenomenon. The introduction about quantum or classic physics and pure theory is skipped, and indispensable parts of the basic NMR physics are explained. For a more complete description, please refer to the list of references [15-17].

2.1 Basic MRI physics

The principle of NMR phenomena is the basis of MRI systems. The structure of an atom is an essential component of the NMR phenomena, and it consists of three fundamental particles: protons (positive charge), neutrons (no charge), and electrons (negative charge) as seen in Figure 2-1 (a). The nucleus is at the center of the atom and contains the protons and neutrons. In the basic NMR physics, individual nucleus has a natural property, and the behavior of nuclei (simply protons) becomes at the center of attention. Because even a tiny piece of biological tissue in a human body contains billions of billions of atoms, the NMR phenomenon can be derived when the fundamental reaction of atom can be extracted and utilized against excessive external energy artificially made by RF signals (pulses).

2.1.1 Spin and magnetization

According to quantum mechanics and Felix Block's nuclear magnetic resonance theory [18,19], the electrons and nucleus (the combination of protons and neutrons) possess the fundamental quantum mechanical characteristic that is the intrinsic angular momentum (spin angular momentum, or simply spins) of a given particle such as electrical charge or mass. As shown in Figure 2-1 (a), a nucleus consists of protons and neutrons. NMR phenomena focus on the behavior of the nucleus than that of electrons because the spin of the nucleus or simply proton constitutes the foundation of NMR phenomena. The spin is determined by the spin quantum number, and it is represented by symbol, S, in (2-1).

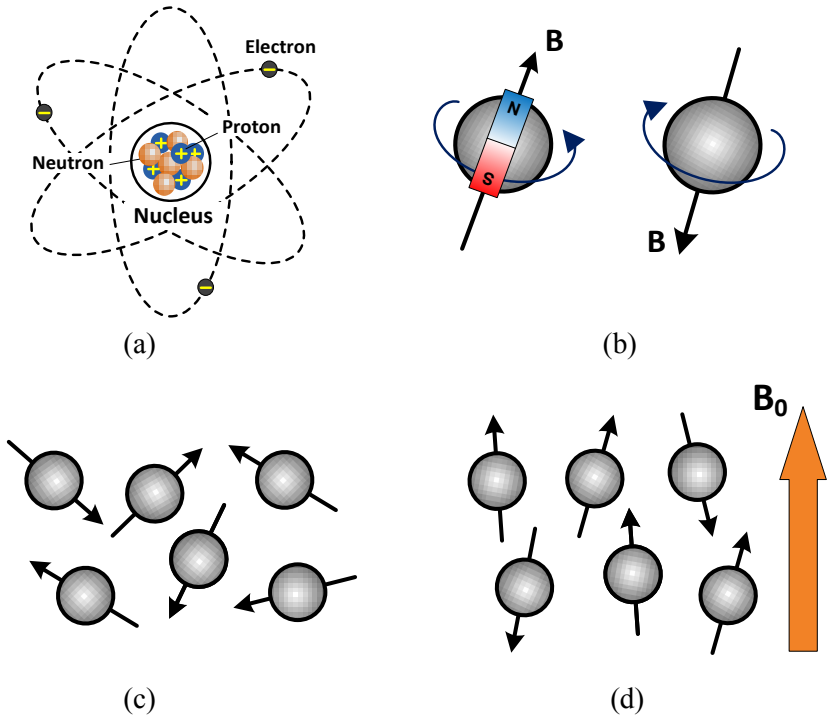

Figure 2-1. (a) The atomic model. (b) A rotating particle (nucleus), spin, with a positive charge generates a magnetic moment (μ) oriented parallel to the axis of rotation and the direction of the generated magnetic moment depends on the direction of rotating of the spinning particle. (c) With no external magnetic field, the spins have their axes oriented randomly. (d) When an external magnetic field (B_0) is applied, the spins align with the direction of the magnetic field with two ways, parallel or anti-parallel.

This property is related to the specific energy levels that each given particle can take. If the number of both the protons and neutrons in a given nucleus are even then S=0, i.e. there is no overall spin because two or more particles with opposite spins can pair up thereby cancelling the spin effect in NMR phenomenon. However, the nucleus can have spin property when the total number of protons and neutrons is odd, or the total number of protons is odd (Figure 2-1 b). As atomic nuclei are charged, the spinning motion causes a magnetic field in the direction of the spin axis like a tiny bar magnet shown in Figure 2-1 (b). This magnetic field is termed the magnetic moment, μ, and it is vector quantity as follows.

$$\vec{\mu} = \gamma \vec{S} \tag{2.1}$$

The proportional constant, γ, is called the gyromagnetic ratio for the particular spinning object. The unit of angular-frequency is divided by magnetic field or radians per second per Tesla. The magnetic moment (μ) is produced with a rotating nucleus with a charged particle (protons) in motion, and its intensity is related to the mass, charge, and rate of spin of the nucleus. Consequently, the role of protons is important to NMR phenomenon because the fundamental property of a proton is the production of a small but noticeable magnetic momentum (field), positive electric charge, and spin. These protons inside the human body act like a great number of tiny bar magnets.

From now on, the protons of hydrogen nuclei will be discussed in this dissertation except any other nuclei because approximately 63% of the human body is composed of hydrogen atoms as seen in table 2-1. Due to its abundance in the human body, the hydrogen nucleus, ^{1}H, is a primary candidate for MRI signal measurements.

In the absence of an externally applied magnetic field (B_0), the magnetic moments have random orientations. Each proton has a spin individually with an arbitrary direction. Therefore, the sum of total magnetic moments associated with a nuclear spin is zero (Figure 2-1 (c)). When an external magnetic field is applied, the magnetic moments of the protons align themselves with the axis of the externally applied magnetic field. Approximately half of them are in the parallel to the field direction, and the other almost half of them align with anti-parallel to the magnetic field in Figure 2-1 (d). It can be considered there are two different energy levels from the quantum physics, and this energy difference is linearly proportional to the strength of the external magnetic field. A lower energy level is associated with the parallel state, and a higher energy level is associated with the anti-parallel state. Under the thermal equilibrium condition, the number of nuclei in the higher energy level (anti-parallel) is fewer than the number of nuclei in the lower energy level (parallel). This preference makes a small but very significant difference in population between the two energy levels. Eventually, the sum of all tiny magnetic fields of each proton in the human body points at the same direction along the external magnetic field, and it is nonzero. In other words, the piece of a tissue is magnetized in the presence of the external magnetic field. This is called the net magnetization and symbolized as M. This net magnetization accurately reflects the

behavior of each individual nucleus and magnetic moment. The net magnetization is simply the sum of the nuclear magnetic moments, $\Sigma\mu$ [18-20].

In general, there are three axes (X, Y, and Z) perpendicular to one another in describing the coordinate MRI system. An externally applied magnetic field is parallel to the Z direction, and the magnetization of this axis is referred to as M_Z. In the X-Y plane, the magnetic moments of the proton are cancelled out because the spins of X and Y directions are randomly oriented and out of phase in XY plane. However, the magnitude of M along Z direction, M_Z, is proportional to the proton density, the strength of the external magnetic field, and the gyromagnetic ratio. When the magnetization exists only in the part aligned along the external magnetic field with no net magnetizations in the X-Y plane, such state of the net magnetization is called equilibrium, and it is symbolized as M_0. By equations in (2-1), (2-2), and (2-3), the net magnetization (M) is determined by gyromagnetic ratio, the number of nuclei, the strength of external magnetic field (symbolized B_0 at equilibrium), and magnetic susceptibility symbolized as χ in (2-3).

$$M = \Sigma\,\mu \tag{2-2}$$

$$M = \chi B_0 \tag{2-3}$$

$$M_Z = M_0,\ \ M_X = M_Y = 0 \text{ at equilibrium}$$

The left side of Figure 2-2 (a) shows the coordinate system of MRI with no external magnetic field. In this case, there is no net magnetization at each axis, and the protons are oriented randomly inside the human body. However, Figure 2-2 (b) depicts a human body lying on the bed in MRI scanner with the externally applied magnetic field, B_0. The net magnetization is only generated along the direction of B_0, Z-axis if any other external signal is not applied.

In this configuration (Figure 2-2 b) of magnetization by spins, the entire energy state is stable, which means the lowest energy level, and it is the arrangement to which the protons will naturally try to return following any perturbations, such as energy absorption in the name of equilibrium. The induced magnetization, M_0, is the basic source of NMR signal for all of the MR experiments. Consequently, all other things being equal, the

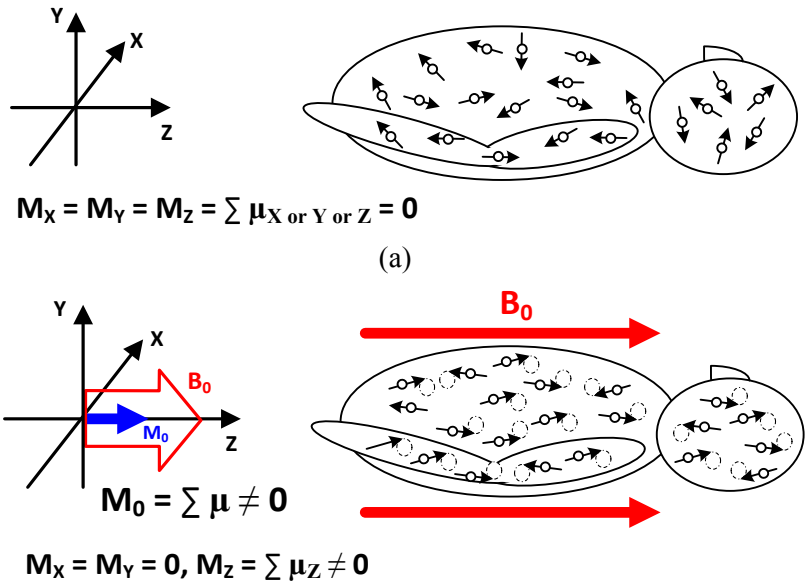

Figure 2-2. The coordination system of MRI and the net magnetization: (a) when no external magnetic field, there is no net magnetization. (b) when a strong external magnetic field, B_0 is applied, the human body has net magnetization, M_0.

larger the strength of external magnetic field (B_0), the larger value of the net magnetization (M_0) [15].

2.1.2 Larmor precession and frequency

As described in the previous part, the net magnetic moment of the protons aligns with the direction, Z axis, of the magnetic field and presents the net magnetization inside the tissue due to the external magnetic field at equilibrium condition. This alignment is not perfect due to the quantum spin states. This builds torque, (2-4), which causes a change in angular momentum with the particular angular frequency. Namely, the proton not only spins around its own axis, but also "precesses" around the axis of the external magnetic field (B_0) as seen in Figure 2-3. The projection of the Z axis is the constant component with same magnitude and direction as the proton precessses, but the projections of the X and Y components vary with time at a constant rate that is given by an equation (2-7) called the Larmor equation or frequency. When the angular motion analysis is applied to

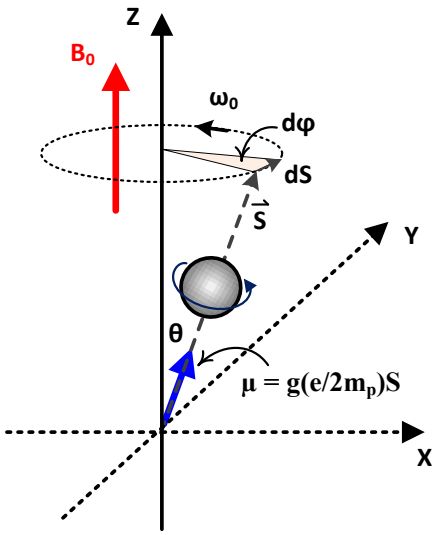

Figure 2-3. A proton precesses, not only rotates about its own axis but also wobbles about the axis of magnetic field, in the presence of an external magnetic field, B_0.

describe the rotating object, this angular frequency is proportional to the strength of the external magnetic field, B_0. To derive the Larmor frequency, the torque, $\vec{\tau}$, on the spin is given by

$$\vec{\tau} = \vec{\mu} \times \vec{B} \tag{2-4}$$

When the equation (2-1) is recalled and Figure 2-3 is referred, the equation of motion of the spin is expressed by

$$\vec{\tau} = \vec{\mu} \times \overrightarrow{B_0} = \frac{d\vec{S}}{dt} = \frac{S \sin\theta d\varphi}{dt} \tag{2-5}$$

$$\mu = g\frac{e}{2m_p}S,\ \gamma = g\frac{e}{2m_p}$$

$$\vec{\tau} = \vec{\mu} \times \overrightarrow{B_0} = \mu B_0 \sin\theta = \gamma S B_0 \sin\theta$$

$$\frac{S \sin\theta d\varphi}{dt} = \gamma S B_0 \sin\theta \tag{2-6}$$

where S is the spin quantum number, q is the charge of the proton, m_p is the proton's mass, g is the constant known as correction factor, and the gyromagnetic ratio, γ, is

defined between the magnetic momentum and spin, and it has a constant value for each nucleus. From equation (2-6), the angular momentum changes the orientation of the rotational axis of a rotating particle without changing the magnitude. Therefore, the proton precesses around the external magnetic field (B_0), and its frequency, "Larmor frequency", is derived by

$$f_{\text{Larmor}} = \frac{d\varphi}{dt} = \frac{\gamma S B_0 \sin\theta}{S \sin\theta} = \gamma B_0 \, [MHz] \tag{2-7}$$

This is the most important equation of NMR phenomenon, and it relates the magnetic field to the resonance frequency in MRI system. The gyromagnetic ratio ($\gamma/2\pi$) and Larmor frequency are tabulated in Table 2-1 with several nuclei for MRI experiments. Normally, MRI experiments are most interested in a hydrogen proton, ^{1}H ($\gamma/2\pi$ = 42.57 HMz/T), for imaging because biological tissues are predominantly ^{1}H, ^{16}O, ^{12}C, and ^{14}N, and the hydrogen atom is the major species that is MR sensitive and the most abundant atom in the human body.

2.1.3 Excitation (RF transmission) and relaxation (RF reception)

As mentioned at the beginning of the introduction, MRI hardware is almost the same as wireless communication systems. The principle of RF system for MRI is that RF circuits

Table 2-1. Nuclei of medical interest and their NMR properties.

Element	Symbol	Nuclear moment, μ.	Gyromagnetic ratio, γ/2π. [MHz/T]	Sensitivity (% vs. ^{1}H)	Biological abundance [%]
Hydrogen	^{1}H	2.79	42.58	100	63
Oxygen	^{17}O	1.89	5.77	0.03	26
Carbon	^{13}C	0.7	10.71	1.59	9.4
Nitrogen	^{14}N	0.4	3.08	0.001	1.5
Phosphorus	^{31}P	1.13	17.25	6.63	0.24
Sodium	23Na	2.28	11.27	0.09	0.04

transmit RF signal (commonly called RF pulse in MRI applications) into the human body to excite the nuclei as energy absorption and then receive RF signal as energy release including anatomical information generated by the proton's response against RF signal transmitted as shown in Figure 2-4. The transmitted RF signal from the power amplifier has a high power level (generally ~kW range), but the received RF signal from the human body is a very small power level (~μW range) through the RF coil (antenna-like device in MRI applications) and the low noise pre-amplifier. By convention, RF transmit involved in the stimulation of nuclei is called "excitation" and RF receive involved in the detection of released RF signal is called "relaxation" in MRI system.

2.1.3.1 Excitation (RF transmission)

Under the equilibrium condition with the external static magnetic field (B_0), any NMR signal cannot be measured because every condition is stable. The basic concept of using the RF signal (pulse) emerges to detect the MR signal by the behavior of protons in this part. When the net magnetization with a different axis or plane can be used, MR signals are detectable by the sum of vectors from individual protons. In other words, the net

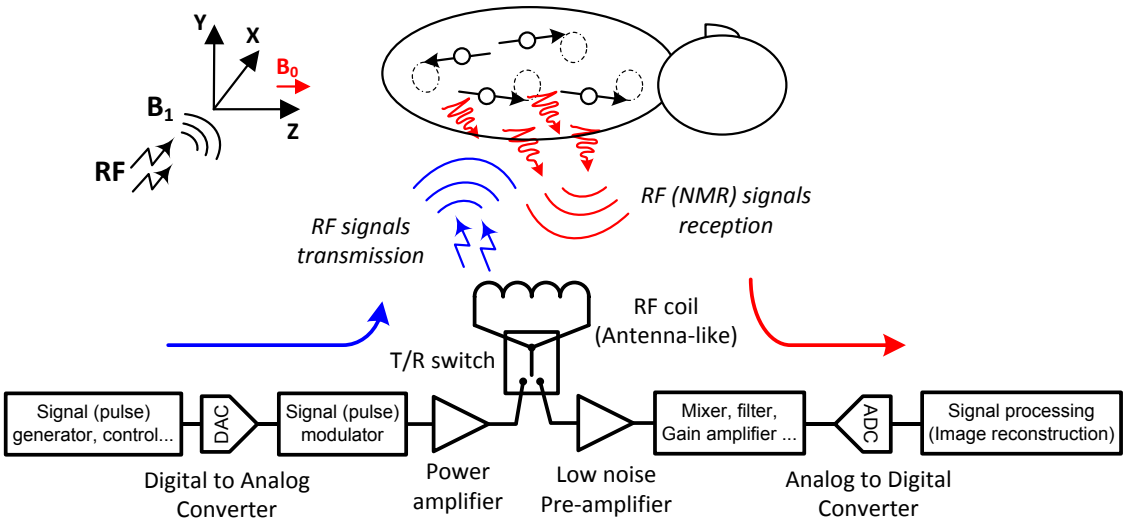

Figure 2-4. RF system of MRI: the RF transmission path is for exciting the nuclei in the human body and RF reception path is for detecting the RF (NMR) signal including anatomical information to generate MR image.

magnetization must be flipped away from the B_0 direction, Z axis. In general, the net magnetization of XY plane, M_{XY}, can be utilized as seen in Figure 2-5. The RF front-end consisting of a power amplifier, a RF coil, and a low noise pre-amplifier is required to excite the objects, generates the XY plane magnetization, and then detects MR signals. Figure 2-5 (a) shows that there is no net magnetization in XY plane and only Z component is with its value, M_0, at equilibrium. However, the net magnetization in XY plane, M_{XY}, is created after a RF signal (pulse) is applied with the same angular frequency of the protons, the Larmor frequency, as shown in Figure 2-5 (b). The present situation of this interaction between RF pulse and the proton spin is called "resonance", that is, it makes the resonance condition that the frequency of the RF pulse matches the frequency of the precession of the protons in human body. RF energy transfer is always the most efficient at resonance condition, and only the protons spinning with the same frequency with the RF pulse absorb the RF energy and respond to the RF pulse.

RF energy is transferred to the proton by applying a RF electromagnetic field (denoted by B_1) generated by the RF coil in the transverse plane, XY plane, whose frequency equals to the Larmor frequency to meet the resonance condition. As the proton absorbs energy created by the RF excitation (transmission), the net magnetization tilts from Bo axis to XY plane with the flip angle, α, as seen in Figure 2-5 (b), and then the net magnetization in XY plane will gradually disappear. The behavior of the proton recovers the equilibrium condition, which is the most stable and lowest energy state, after RF energy by the excitation is turned off. The B_1 field generated by the RF coil is relatively much smaller (~μT) than B_0, but it makes a significant flip angle. The flip angle in the range from 1° to 180° depends on the application of a designed timing and intensity of RF pulse. The XY component of the net magnetization has the maximum magnitude that is equal to the magnitude of M_0 when the flip angle is 90°. Therefore, RF pulse design and the efficiency of the RF hardware of MRI systems are essential parts to extract the MR signal accurately.

Consequently, RF pulse using the resonance condition is utilized to stimulate the hydrogen proton either absorbing or releasing RF energy. Therefore, RF circuits as the front-end of MRI systems are essential parts to derive the source of the MR signal.

2.1.3.2 Relaxation (RF reception)

After RF pulse is turned off, the magnetization in the XY plane dose not precess

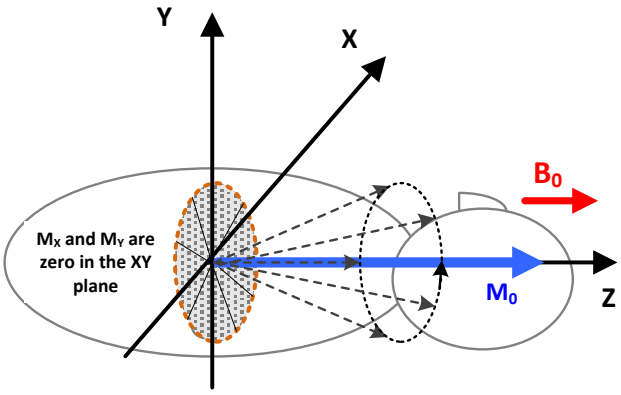

(a)

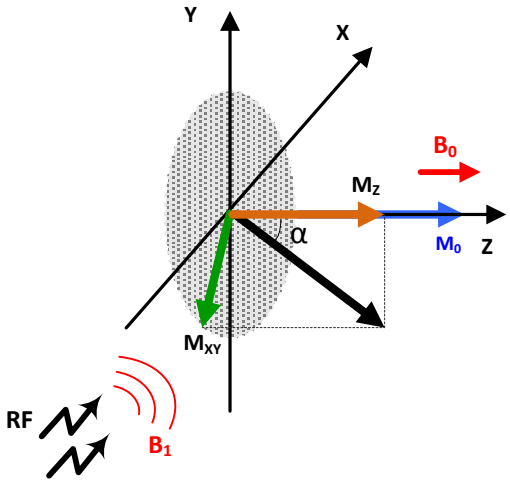

(b)

Figure 2-5. (a) The main static magnetic field (B_0) with spin precession, and (b) after RF pulse is applied, the net magnetization vector is partially flipped toward XY plane (M_{XY}) with a flip angle, α form the Z axis.

infinitely but gradually turns back to the equilibrium state having the lowest energy level. This process is known as relaxation, and it makes the MR signal detectable. Although it is the individual reaction (absorbing or releasing RF energy) of each proton, the relaxation process can be statistically quantified for an entire object. The main point is that the protons emit RF signals matched to the Larmor frequency, and then the RF circuits detect them during RF relaxation (reception).

Figure 2-6 shows the magnetization components. During the relaxation time, only Z component (M_Z) of the net magnetization is shown in Figure 2-6 (a) and the M_{XY} of the transverse (XY) plane is in Figure 2-6 (b). The net magnetization for the relaxation roughly looks like a spiral motion toward the Z direction as the composition of both M_Z and M_{XY} in Figure 2-6 (c). In the procedure of the relaxation, there are two types: longitudinal relaxation (T_1) and transverse relaxation (T_2) as shown in Figure 2-7. Both are the two different mechanisms by which this occurs. T_1 is the relaxation time constant at which the longitudinal magnetization (M_Z) returns to its equilibrium state (M_0), and it is described by equation (2-8). T_2 is the relaxation time constant at which the transverse magnetization, M_{XY}, decays to zero at a rate characterized by equation (2-9).

$$M_Z(t) = M_0\left(1 - e^{-t/T_1}\right) \tag{2-8}$$

$$M_{XY}(t) = M_0 e^{-t/T_2} \tag{2-9}$$

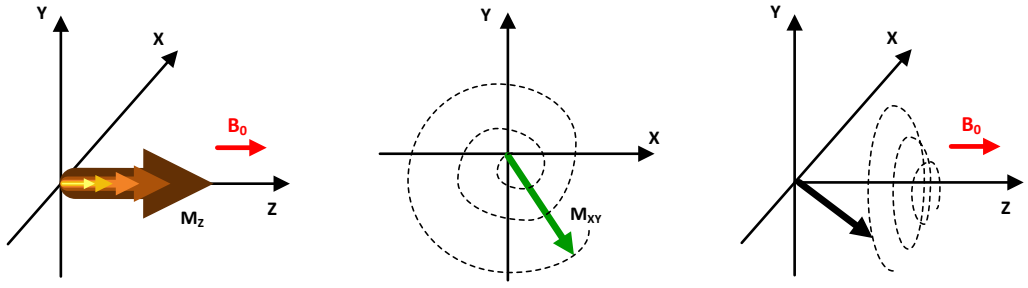

(a) (b) (c)

Figure 2-6. the magnetization components during the relaxation. (a) Z component (M_Z), (b) XY component (M_{XY}), and (c) the net magnetization component.

The recovery time (T_1) of longitudinal magnetization and the decay time (T_2) of transverse magnetization occur simultaneously but have a different time constant by the Bloch equations (referred to [15]).

The mechanism of T_1 relaxation is that the protons release the excess energy absorbed from RF pulse to the surrounding lattices (molecule) inside a tissue of the human body in order to return to their equilibrium state. Therefore, T_1 is also called the spin-lattice relaxation time and energy loss process. The rate of T_1 relaxation is depicted as shown in Figure 2-7 (a). The curve is exponentially increasing by (2-8) from no magnetization in the Z direction right after 90° RF pulse. The T_1 is defined as the value when M_z reaches to 63% of M_0.

The mechanism of T_2 relaxation is slightly more complicated. During the RF excitation, the spins maintain phase coherence in XY plane because the RF field B_1 is larger than the individual magnetic moments of each proton spin. Therefore, the protons rotate in phase and result in magnetization in the XY plane. After the RF pulse terminates, however, the M_{XY} dephasing occurs for two reasons: the proton spins have slight different magnetic moment, and the external magnetic field is not homogeneous. T_2 relaxation time is a parameter that is a characteristic of a specific tissue and characterizes the rate of dephasing of the protons associated with that tissue. The curve of decay is drawn in Figure 2-7 (b) and T_2 is defined as the time that it takes for the spins to dephase to 37% of

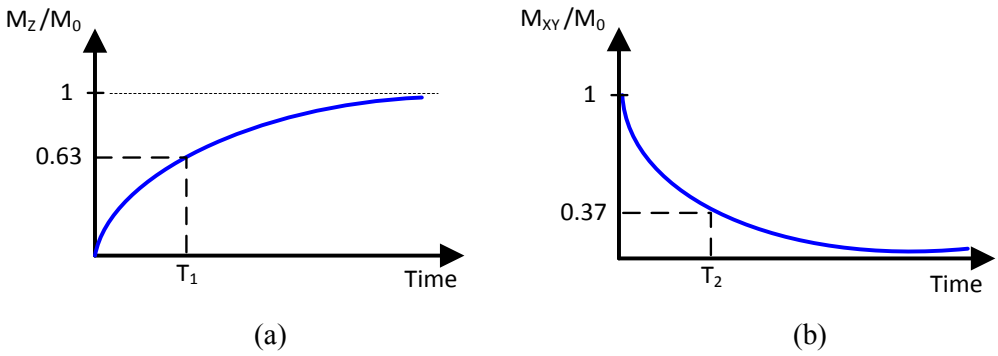

Figure 2-7. The relaxation time constants. (a) T_1 by RF energy releasing of protons and (b) T_2 by precessing protons out of phase over time.

Table 2-2. T1 and T2 relaxation time for various tissues at 1T and 3T

Tissue	1 T		3 T	
	T1 [ms]	T2 [ms]	T1 [ms]	T2 [ms]
Fat	180	90	382	68
Liver	270	50	570	45
White matter	390	90	832	80
Spleen	480	80	1514	65
Gray matter	520	100	1331	110
Muscle	600	40	898	29
Blood	800	180	1932	275

the maximum value.

It is necessary to differentiate and classify the components of the human body, and the different tissues have different relaxation times shown in table 2-2 which vary with the field strength of the external magnet. The MR signal intensity and image contrast are generated by the combination of the density of the protons, field strength, and realization time constants.

In practice, Figure 2-8 shows how RF circuit detects the MR signals and how the

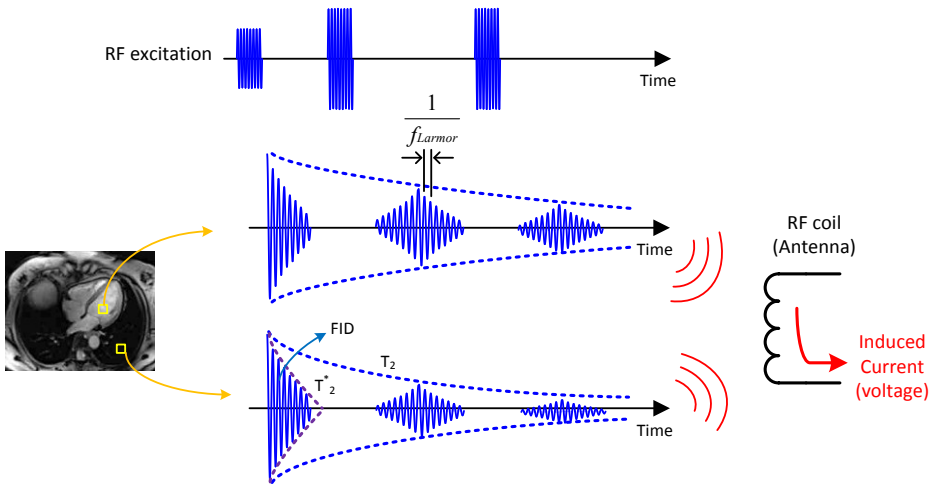

Figure 2-8. The practical NMR signals with different response time, $T^*_2{}'$ and $T^*_2{}''$ relaxation time constants, and RF coil inducing current (or voltage) associated with these NMR signals.

relaxation times affect to the RF receiver. When the protons release the excessive energy, they emit RF signals with the electromagnetic radiation. The decaying RF signal itself is oscillating at the Larmor frequency and described mathematically as

$$M_{XY}(t) = M_0 e^{-t/T_2^*} \ (\cos \omega_0 t) \tag{2-10}$$

T^*_2 is based on T_2 relaxation time, and it is added with the effect of the external magnetic field inhomogeneity. This NMR signal is called free induction decay (FID) and T^*_2 is always less than T_2 relaxation time. T_2 is commonly measured through sequences of one 90° pulse and several subsequent 180° pulses. As shown in Figure 2-8, different tissues makes different MR signals, and the T_2 relaxation time can be measured from the envelope of multiple spin echoes with the maximum response against the multiple RF pulses using various pulse sequence techniques.

The most important fact is that this decaying RF signal induces current in the RF coils. The induced current is directly associated with the response of the protons and follows the pattern of FID. This detected MR signal is amplified, down-converted to a baseband frequency region, digitized, and digitally processed (FFT) to reconstruct the MR image.

2.2 MRI hardware system

The schematic diagram of the hardware system of a MRI scanner is shown in Figure 2-9. The main components: a magnet, shim coil, gradient coils, and a RF coil including an impedance matching block are placed in a shielded room. To control and drive these components, coaxial cables connect gradient amplifiers and RF transmit/receive blocks. In addition, computers are used to control the components, generate the RF pulse, store the data, and reconstruct the MR images. The m magnet produces a strong, static, and homogenous magnetic field (B_0) along with shim coils that compensate for the filed inhomogeneity produced by the main magnet. It is accomplished by producing corrective magnetic fields in various directions. The gradient coils generate linear location-varying and time-varying weak extra magnetic fields (30 ~ 40 mT/m) superimposed on the main magnetic field (B_0) by sets of current loops as shown in Figure 2-10. A set of three gradient coils in x, y, and z directions is necessary in order to provide the spatial

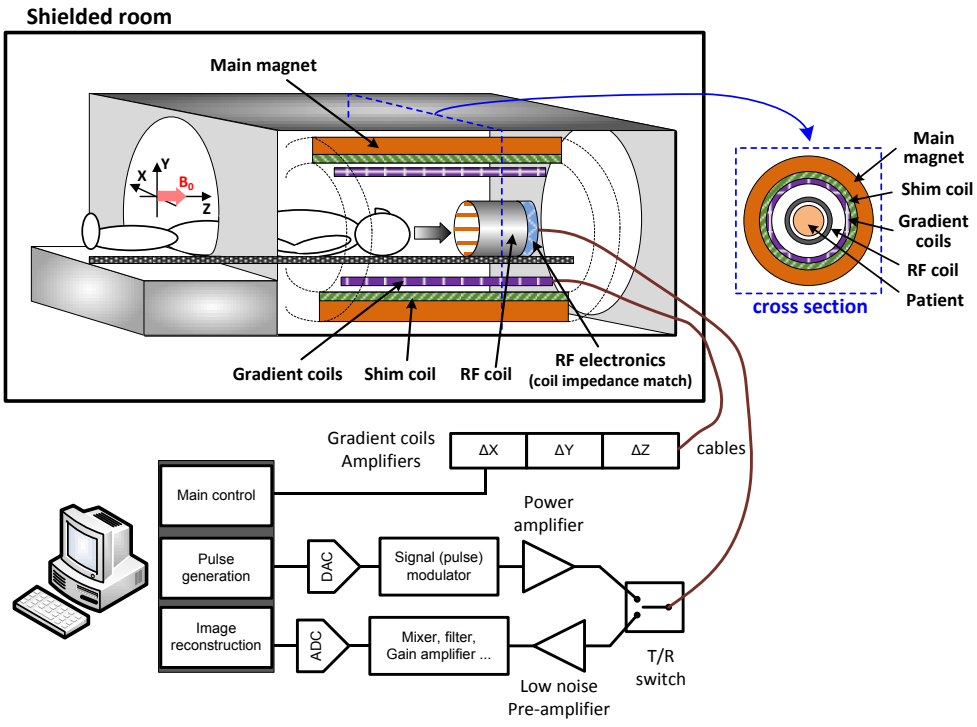

Figure 2-9. A schematic diagram of a general MRI system and a cross section inside of MRI scanner

information needed to reconstruct MR images. The gradient coils identify which part of the MR signal belongs to each slice and a pixel within its slice. The set of slice orientations is defined in Figure 2-10. Each coil needs an individual amplifier to drive it independently. During the operation of gradient coils, eddy current may appear, and it causes reduction of the RF performance and results in distortions of the MR Images.

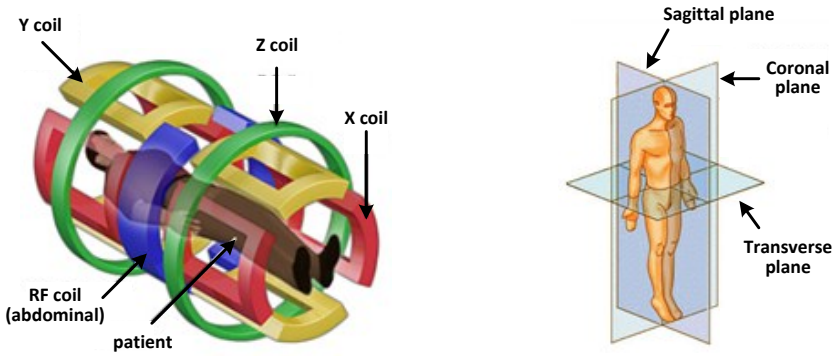

(a) (b)

Figure 2-10. (a) gradient coils (x-, y-, or z-direction), (b) slice orientations (sagittal, coronal, or transverse)

The RF oscillating local magnetic field (B_1) is generated by RF coils (transceiver or transmit only) and is coupled to the human body. It transports RF energy into the body and excites the protons in the form of an electromagnetic wave. RF coils (transceiver or receive only) are also used to receive the induced MR signals from the body. The impedance between RF coil and RF transceiver circuits must be matched to carry RF signals efficiently, and this requires the impedance matching block as seen in Figure 2-9. The detailed RF coil will be featured in the following parts.

The shielded room is required to prevent exterior RF interferences. Every RF source such as radios or TV broadcasts, mechanical/electrical devices outside MRI room can produce artifacts in MR images if these have RF signals near the Larmor frequency. Copper foil laminates cover an exam room entirely, and the shield is connected to an electrical ground at a single point to reduce grounding effect. There are some MRI electronics such as amplifiers and filters outside of the MR shielded room to drive coils

Figure 2-11. Active shielded 7T 90cmbore magnet (left), (b) RF head coil (right top), and (c) MRI electronics (right bottom): Power amplifiers, digital receiver, etc. (CMRR in University of Minnesota)

and to receive the induced MR signals that are amplified and digitized to reconstruct MR images. Figure 2‑12 presents the 7T MRI system established in Center for Magnetic Resonance Research (CMRR), University of Minnesota. The 7T magnet designed for examining the human body with a multi-channel RF head coil and peripheral electronics such as power amplifiers, receivers, controllers, etc. are also shown in this figure.

2.2.1 RF circuits and systems

To excite the protons, RF transmitter should amplify RF signals from mW to kW range (a few hundred volts in RMS in a 50Ω impedance) using multiple stage power amplifiers (see Figure 2-12), e.g. 0.5 ~ 2kW (peak power) for the legs or arms, 4 ~ 8 kW

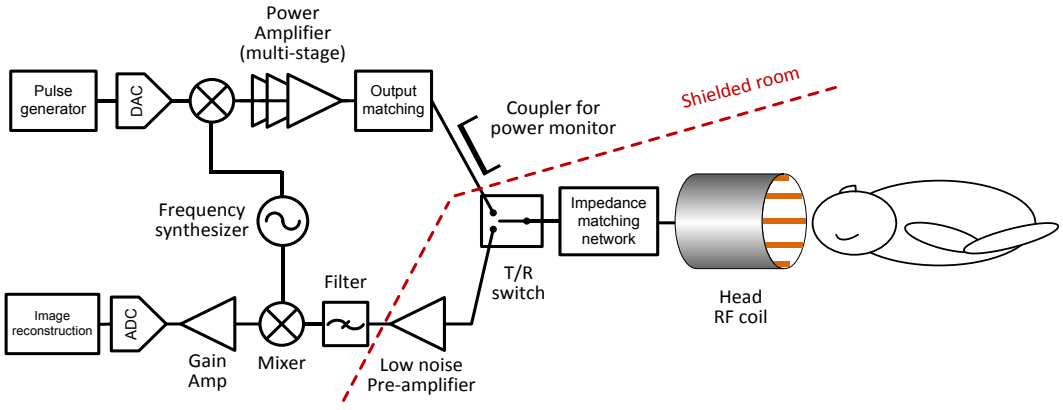

Figure 2-12. RF front-end diagram.

for the head, and up to 35kW for the whole body are commonly utilized. For multi-channel coils, around 1kW (60dBm) per channel is generally employed [21]. Modern RF transmitter configures power-monitoring block using a RF coupler to check the system performance or safety. The up-converted frequency for the transmitter and the down-converter for the receiver are identical to the configuration of a general wireless transceiver. The RF signal is up-converted using a frequency synthesizer to the Larmor frequency in the transmit side, and the RF coil creates an oscillating magnetic field (B_1) with this frequency. As shown in Figure 2-12, Low noise pre-amplifiers are currently being integrated into the RF coil's side in the receiver. It enhances image qualities by improving the Signal to Noise Ratio (SNR) by avoiding the measured signal loss, noise pickup, and interconnection loss. The bandwidth of the received MR signal is small (less than 20kHz typically) and depends on the gradient field strength. One of the modern technologies is the direct sampling of the received signals because the performance of the recent Analog-to-Digital Converters (ADC) with the sampling frequencies of over 100MHz obtains 12 ~ 16 bits digitized data. This high performance ADCs allow bypassing the mixer in the receiver unlike a conventional MRI receiver structure or one chip solution for multi-channel parallel imaging by time multiplexing. The output voltage of the low noise pre-amplifier having about 15dB ~ 20dB gain is generally a few tens of millivolts. The bandpass filter allows only the Larmor frequency range, while blocking lower and higher frequencies. Since the magnitude of the received signals is still low, signals should be amplified again before quantization. To switch the signal path from the transmitter to the receiver and vice versa securely, some characteristics such as fast switching, high isolation between transmit and receive ports, low insertion loss, high power capability are required. Additionally, very high signal level difference between transmitter (60dBm) and the receiver (-50dBm) make the design of the T/R switch unit challenging.

2.2.2 RF coils

As mentioned earlier (referred to Figure 1-1 and Figure 2-9), the configuration of RF front-end for MRI systems is almost the same as the structure of RF transceiver for general communication systems except for the exclusive factors: a RF coil, high power (~ kW) capability, and the requirement of non-magnetic property. Although the role of RF coils is also almost the same as common antennae, there are additional characteristics. RF coils should generate RF magnetic fields (B_1) in the near-field and be optimized for the particular regions of the human body. RF coils generate a time varying magnetic field which has the Larmor frequency. Therefore, a RF coil is a RF resonator that needs a driving circuit consisting of a power amplifier, a frequency tuning, and an impedance matching block. The resonating RF signal is transmitted from the power amplifier to the RF coil through the well-tuned and matched driving circuits using inductive and capacitive components. Inductive and capacitive components make the resonator. The inductive components are made of wire (coil-like) or metallic (usually copper) strip-line with low resistance, and the capacitive components are made of a gap between conductors or a discrete capacitor. When both inductive and capacitive components are combined and adjusted, RF resonator produce the proper resonance frequency (i.e. the Larmor frequency) and form the local B_1 field. The generating magnetic fields in the near-field can be a major difference between a RF coil and a common antenna that transmits an electromagnetic wave to the desired region, usually in the far-field [21].

Obviously, RF coils are critically important pars, not only in the RF front-end but also in the entire MRI scanner. It means the performance of RF coils directly affects the MR image quality as the final output of MRI systems. Thus, various types of RF coils have been proposed and applied to optimize the respective application and obtain the highest possible SNR.

2.2.2.1 Types of RF coils

In this part, TEM vs. birdcage coil with the quadrature driving, transmit & receive vs. transmit-only + receive-only coils, single vs. multi-channel coil, and surface vs. volume coil, and are presented consecutively. A variety of RF coils (see Figure 2-15) has been

developed and applied to maximize the efficiencies associated with SNR, resolution, and local field distributions. TEM and birdcage coils are widely used for the modern MRI systems. Thus these coils are first presented. An example of the modern RF coil design is shown in Figure 2-13 using the combination of a transmit & receive and receive-only coils based on the transverse electromagnetic (TEM) and multi-channel structure [22].

(a) (b) (c)

Figure 2-13. An example of the latest RF coil design: (a) 16-channel transceiver coil, (b) 16-channel receive-only coil, and (c) the combination of 16-channel transmit and 32-channel receive coil. (image captured from [22])

TEM vs. birdcage

In the initial state of RF coils for a human body, large inductance and capacitance of RF resonators limited the range of the resonance frequency. Therefore, a demand for a new coil appeared to produce the uniform B_1 field surrounding an entire head or a body in higher frequency regions. After many studies and evaluations, two types of the modern RF coils, Transverse Electromagnetic Mode (TEM) coil (also known as transmission line coil) and birdcage coil, are widely researched in high field MRI systems.

The TEM resonator (Vaughan et al., 1994) [27] is the modern and popular RF coil design as illustrated in Figure 2-14 (a). A single element consists of a conductor strip and its shield as seen in Figure 2-14 (b) [28]. The rungs and end rings of a birdcage resonator limit the resonance frequency because the inductance and capacitance of the rungs and end rings are too large to build the desired operating frequency. However, the TEM coils can be free from the limitation of the resonance frequency. The current's paths of a TEM and birdcage coil are the root cause.

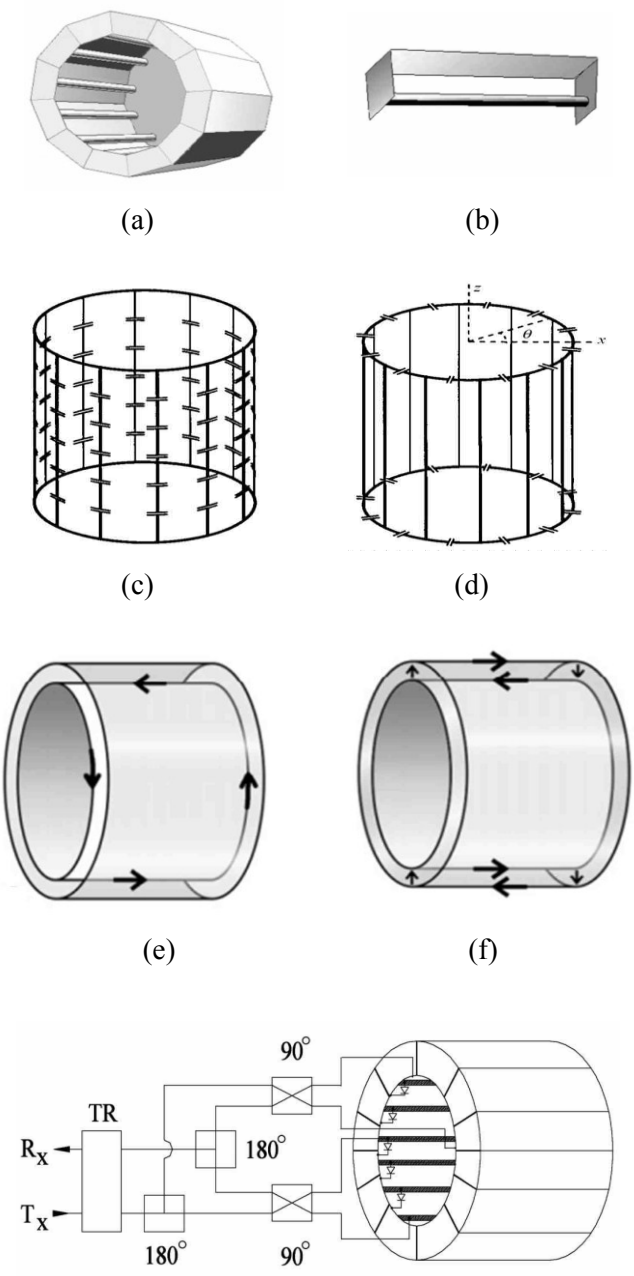

Figure 2-14. (a) Segmented TEM volume resonator coil, (b) single element of TEM resonator, (c) a low-pass birdcage resonator, (d) a high-pass birdcage resonator, (e) a current flow of a birdcage resonator, (f) a current flow of a TEM resonator, and (g) TEM transmit and/or receive volume coil based on quadrature drive and detection.

The current's returning path flowing the rungs and end rings (see Figure 2-14 (e)) of a birdcage resonator affects the resonance frequency. Therefore, the size of end ring becomes problematic in a volume coil design at ultra-high fields which have higher operating frequencies. The TEM resonator, however, provides very flexible design to achieve higher frequency operations because it has an individual current's returning path by the shield plane as seen in Figure 2-14 (f) [28]. Therefore, the operating resonance frequency of the TEM resonator has no concern with the diameter of the coil. Although the structures between a TEM and birdcage resonator look similar, the aforementioned frequency responses make a significant difference. As a result, The TEM coils have a predominant role at ultra-high field applications. Figure 2-14 (g) shows an example of TEM volume coil based on quadrature drive and detection structure [29].

The birdcage coil (Hayes et al., 1985) [25] was designed to avoid the field's non-homogeneity of the early coils, e.g. saddle coil. It generally consists of multiple legs with some capacitors and circular end rings. Figure 2-14 (c) and (d) show the structure diagram of the low-pass and high-pass birdcage resonators. In the low-pass type, metallic legs with multiple capacitors on each segment are evenly around the cylinder. The high-pass birdcage resonator, however, has the configuration of the inductive leg components and the end rings with multiple capacitors to generate a uniform local field at higher frequencies [25,26]. Thus, the positions of the capacitors decide the low-pass or high-pass types. Additionally, the symmetric location of rungs and capacitors helps the uniformity of B_1 field. The birdcage resonator is well tuned and matched using the driving circuits and typically excited at two ports which are driven in the quadrature mode. RF shield, the external shield of birdcage resonator, is required to prevent the interference between the RF coil and the outside effects, e.g. gradient coil [26].

Quadrature coil

When the quadrature (90 degree out of phase) RF pulses are applied in a pair of orthogonal RF coils, it produces circular polarized magnetic fields with the same magnitude, and it is orthogonal to each other in a local field [21]. The symmetrical RF coil and its quadrature method allow the reduction of the power requirements by about

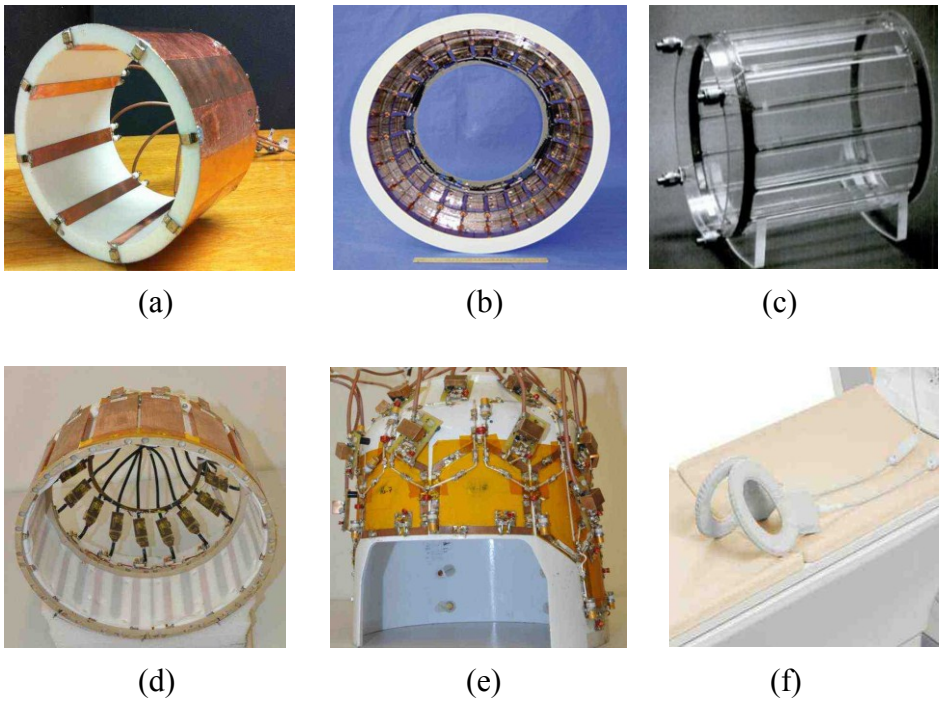

Figure 2-15. Various RF coil types: (a) head coil (transceiver, multi-channel, and TEM), (b) body coil (transceiver, multi-channel, and TEM, image captured from [21]), (c) head coil (birdcage and quadrature, image capture from [24]), (d) head coil (transmit only, multi-channel, and TEM), (e) head coil (receive only and multi-channel), and (f) surface coil (receive only and single channel, image captured from Philips website).

half and increase the signal level resulting in the improved SNR over a linear one by a factor of $\sqrt{2}$ [23]. Namely, $SNR_{quadrature} = SNR_{linear} \times \sqrt{2}$. This quadrature concept is commonly used in both TEM and birdcage coils. To support the quadrature transmission and detection, the RF front-end employs cosine- and sine- quadrature modulation to identify two signals.

Transmit & receive vs. transmit only + receive only coil

Transmit & receive coils generate RF local magnetic fields, B_1, within the objects being examined and then receive the MR signal in the same coils. This configuration can be used to image a whole body, a head, or other parts of interest of a human body in MRI. On the contrary, the transmit-only coil transmits the RF pulse, and then the receive-only

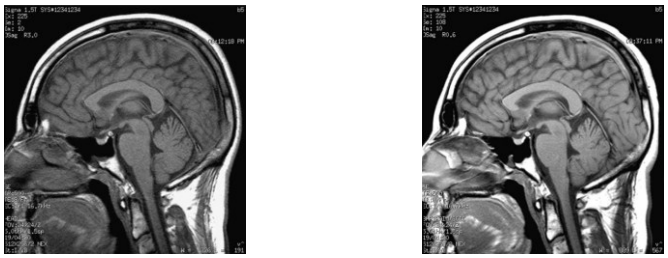

(a) (b)

Figure 2-16. (a) 1-channel receive coil and (b) 8-channel receive coil.
(images captured from [23])

coil receives the MR signal separately. An independent receive-only coil obtains better SNR and resolution for a specific region of the human body. Receive-only coil can approach closely to the sample of interest and maximize the reaction of the protons by different shapes, sizes, and configurations,. As a result, the combination of transmit-only and receive-only coils can improve MR image quality despite the burden of two coils.

Single- vs. multi-channel coil

A major trend of RF coils is multi-channel coil design. In spite of the design complexity and difficulty, modern RF coils pursue the multi-channel RF coils to improve the MR image quality. Figure 2-16 clearly shows the reason why the multi-channel RF coils are necessary. 8-channel coil provides a better image than 1-channel coil by about 40% SNR improvement [23]. Furthermore, the configuration of multi-channel RF coils is essential to the latest MRI technology, the parallel imaging. It, however, is hard to say more channels always bring better MR image quality. There is a trade-off among the number of channels, the size of the RF coil, and the complexity of circuits.

Surface vs. volume coil

A volume coil surrounds an entire sample being imaged, but a surface coil covers or become close to the local interest regions. Figure 2-15 (a) and (b) show the head and body RF coils based on the TEM structure for the example of volume coils [21]. The surface coil is also shown in Figure 2-15 (f). Although an surface coil can cover only

small regions of interest, the surface coils offer relatively higher SNR than the volume coils because the surface coils can become close to the source (protons) of MR signals. In addition, the small size of coils provides the reduction of the RF coil loss. Due to technical limitations such as the non-uniformity of B_1 fields and a strong demand for higher channel number of the multi-channel, a configuration of surface coil usually is the receive-only coil. To take MR images of the head or the whole body of a patient, a volume coil is required. The electrical wavelength is close or shorter than the dimension of the human body when higher operating frequencies are used in ultra-high field MRI systems. Therefore, a volume coil design becomes more complex and difficult to overcome the relatively short wavelength issues. Generally, the TEM and birdcage coils are commonly used for volume coils.

2.2.2.2 Characteristics of RF coils

Research and development of a variety of RF coils is still ongoing, and the performance of these coils is characterized by Q factor, Q ratio, SNR, loss, magnetic field distribution, etc. Resonance circuits, Q factor, frequency tuning, impedance matching, SNR, and field homogeneity are discussed in this part to understand the characteristics of the RF coils.

Resonance circuits and Q factor

The property of resonance circuit is first reviewed. A resonance circuit is one in which equal amounts of energy are stored in the electric and magnetic fields, with the energy exchanging repeatedly between the electric and magnetic fields. Typically, when a capacitance and an inductance component are joined together, they form a resonance condition. A simple RF resonator, e.g. a single loop, can be modeled by a series RLC circuit as seen in Figure 2-17 (a), and the input impedance is given by

$$Z_{Series} = \mathrm{j}\omega\mathrm{L} + \frac{1}{j\omega\mathrm{C}} + R = R + j\left(\omega\mathrm{L} - \frac{1}{\omega C}\right) \tag{2-11}$$

When the inductive component (L) is resonant with the capacitive component (C), the impedance of this series RLC resonance circuit is purely real, $Z_{Series} \approx R$. Therefore, the resonance condition is $\omega L = 1/\omega C$, and the resonance frequency is given by

$$f = \frac{1}{2\pi\sqrt{LC}} \tag{2-12}$$

The resistance R and the inductance L are determined by the geometrical structure of the resonator and not significantly changed. The accuracy of the resonance condition is typically characterized by the quality factor (Q) expressed by (2-13). There are various definitions about Q according to points of view and applications. Conceptually, it is defined as the ratio of the peak magnetic energy (field) stored by the coil divided by the average energy (field) dissipated per second by the coil. It is measured as (2-14) with -3dB bandwidth associated with half power loss around the resonance frequency (ω_0). Likewise, it can be seen as the ratio of the reactive impedance ($\omega_0 L$) over the pure resistance (R_{coil}) given by (2-15) in the series RLC circuit. A high Q coil indicates a coil with a low loss.

In terms of RF coils, the Q of the RF coil depends on the circumstances under which it is measured whether it is unloaded without a sample (or patient) or loaded with a sample (or patient). The quality factor ratio, Q_{ratio}, given by (2-16) is important to decide the RF coil's performance, and this value indicates how much a sample is dominant in a loss term (R_{sample}) in the experiments. After the object is loaded on the RF coil, the frequency and Q lower. It means the losses are dominated by the sample loaded. A higher Q_{ratio} means that RF coils efficiently couple with a sample and the sample absorbs the power induced by the RF coil.

$$Q = \omega \frac{average\ energy\ stored}{energy\ loss / second} \tag{2-13}$$

$$Q_{\omega_0} = \frac{\omega_0}{\Delta\omega_{-3dB}} \tag{2-14}$$

$$Q_{\omega_0} = \frac{\omega_0 L}{R_{coil}} = \frac{1}{\omega_0 RC} \tag{2-15}$$

$$Q_{ratio} = \frac{Q_{unloaded}}{Q_{loaded}} = \frac{\omega_0 L / R_{coil}}{\omega_0 L / (R_{coil} + R_{sample})} = \frac{R_{coil} + R_{sample}}{R_{coil}} \tag{2-16}$$

In practice, most modern TEM resonators for RF coils are modeled by a RLC parallel equivalent circuit as shown in Figure 2-17 (b). The parallel resonance circuit has the same resonance frequency by (2-12) because the resonance condition is that the capacitive and inductive reactance are equal in magnitude, resulting in purely resistive impedance [17]. Q of a parallel resonance circuit is given by (2-17) from the definition of (2-13).

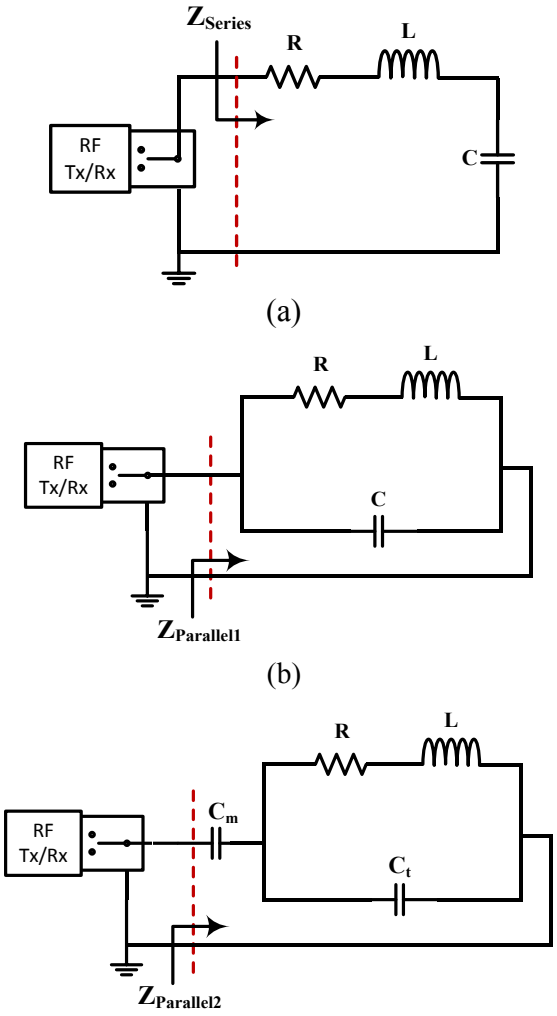

Figure 2-17. Resonance equivalent circuits: (a) a series resonance circuit, (b) a parallel resonance circuit, and (c) a practical equivalent circuit with tuning capacitor (C_t) and matching capacitor (C_m).

$$Q_{\omega_0} = \omega_0 RC = \frac{R}{\omega_0 L} \tag{2-17}$$

The calculation of a parallel equivalent circuit to find the input impedance in (2-18) is considerably more difficult than that of the series equivalent circuit.

$$Z_{Parallel1} = \frac{\sqrt{R^2+\omega^2L^2}\sqrt{\frac{1}{\omega^2C^2}}}{\sqrt{R^2+\omega^2L^2}+\sqrt{\frac{1}{\omega^2C^2}}} = \frac{(R+j\omega L)\left(-\frac{j}{\omega C}\right)}{R+j\left(\omega L-\frac{1}{\omega C}\right)} \Rightarrow R_{Parallel} + jX_{parallel} \tag{2-18}$$

Simply, the input impedance of the parallel resonance equivalent circuit has the real (resistive) and imaginary (reactance) part after the equation is rationalized. Ideally, $Z_{parallel}$ become infinite at the resonance condition. More detailed analysis of a TEM resonator is featured in the following chapter 4.2.

Frequency tuning and impedance matching

Impedance matching commonly involves frequency tuning in the basic RF theory. However, more detailed study about both impedance matching and frequency tuning is necessary in a dominant resonating circuit.

Once the inductance L is fixed by the dimensions of the resonator, the well-tuned capacitance C allows the resonance frequency of the RF resonator that is identical to the Larmor frequency. The variable discrete capacitors are usually utilized for this capacitive component in the RF coil design. This capacitor is called "tuning capacitor (C_t)".

When the resonance frequency is equal to the Larmor frequency, the reactance is cancelled, and the input impedance of the RF coils becomes a pure resistance. Since most RF devices are initially matched to 50Ω at the input and output ports, the resonators for RF coils must be matched to 50Ω to deliver the maximum power from a RF source to a RF coil. Adjusting the tuning capacitor, however, hardly satisfies these two conditions, the frequency tuning and impedance matching, simultaneously. As a result, another component using passive components is required for the impedance matching. Most practical RF coil design uses several capacitors around the resonator for this reason.

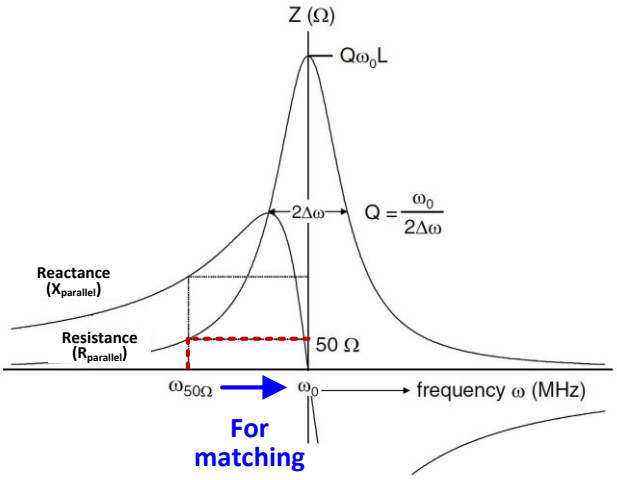

Figure 2-18. The impedance of a parallel RLC resonance circuit versus frequency.

Figure 2-18 explains the aforementioned content with the graph of the impedance variation of a parallel RLC resonance circuit as a function of frequency. The tuned resonance frequency (ω_0) which has the maximum pure resistance may not be equal to the frequency for 50Ω ($\omega_{50\Omega}$). This resonance circuit state is not yet completed, and it must have one more step the tuned resonance frequency is matched to the frequency for 50Ω [17]. In other words, the input impedance of resonance circuit should be equal to 50Ω with one more step: impedance matching procedure. As seen in Figure 2-17 (c), a capacitor, "matching capacitor (Cm)", is usually used in the RF coil design, and the input impedance is expressed by (2-18).

$$Z_{Parallel2} = \frac{(R^2+\omega_0{}^2L^2)\left(R-j\left((R^2+\omega_0{}^2L^2)\omega_0C_t-\omega_0L\right)\right)}{R^2+\left((R^2+\omega_0{}^2L^2)\omega_0C_t-\omega_0L\right)^2} - \frac{j}{\omega_0C_m} \qquad (2\text{-}18)$$

Therefore, at least, two capacitors are required for the frequency tuning and impedance matching, respectively in the RF coil design.

In addition, the combination of these capacitances affects the balance of the local magnetic field distribution, and it should satisfy the electrical condition to create the symmetric field shape at the same time. It will be discussed in the following part in detail.

Field homogeneity

When the wavelength becomes short, the local magnetic field generated by RF coils doesn't have a uniform distribution, but it can be a symmetric shape as illustrated in Figure 2-19 (a). It is the fundamental RF effect in the microstrip structure terminated with capacitive load. In respect of RF coils, the electrical unbalanced condition makes worse as shown in Figure 2-19 (b) and (c) if capacitor values at the ends of a coil element are not balanced. Since the main object being imaged is placed at the center point, the unbalanced field distributions make MR images out of focused. After the frequency

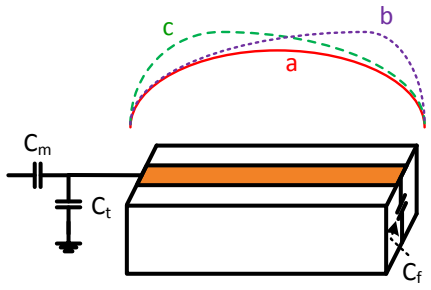

Figure 2-19. Local magnetic field (B_1) distributions of a single TEM element: a general balanced condition (a), and unbalanced conditions (b) and (c).

tuning and the impedance matching, one more step remains to generate the symmetric magnetic field. Therefore, the combination of the tuning and matching capacitors should be balanced with the end capacitor (C_f). In the bench test, these unbalanced distributions can be checked by using a pick-up probe and a network analyzer.

Signal-to-Noise Ratio (SNR)

Signal-to-Noise Ratio (SNR) is one of the most important factors of image quality in MRI system. It decides spatial resolution, temporal resolution, and contrast in MR images. Simply, the SNR is a means to quantify the relative contributions of the measured MR

signal versus the randomly superimposed intrinsic noise [21]. The SNR is a function of square of the magnetic strength, and it is given by

$$\text{SNR} \propto \frac{B_1}{\sqrt{R_\Omega + R_r + R_{sample}}} \tag{2-19}$$

where B_1 is the local magnetic field strength made by a RF coil. Therefore, it is a critical point how well B_1 associated with the RF coil's performance is created. R_Ω, R_r, and R_{sample} represent the coil's resistive loss, the radiation loss, and the coupled sample loss, respectively. R_Ω is the resistance and the loss of the inductive and capacitive components in the RF coil. Typically this value cannot contribute the entire loss compared to the sample loss since most copper foils to build the conductor of a RF coil have less than 0.5Ω. R_r is the radiation loss of a resonance circuit. Ideally, this term is negligible at low frequency applications, but this can affect the coil's performance in real circumstances. R_{sample} is the resistive coupling between the RF coil and the sample.

Chapter 3. **RF/electrical issues in ultra-high field MRI systems**

3.1 Benefits of ultra-high field MRI systems

The ultra-high magnetic field (7T and beyond) MRI systems are advantageous because they increase Signal-to-Noise Ratio (SNR) which can be used to improve the spatial resolution and contrast in MR image quality. The SNR linearly correlates with the static magnetic field strength (B_0). Therefore, the traditional clinical 1.5T (Tesla) magnets are being replaced by 3T. In addition, research magnets of 7T, 9.4T, and 11.74T are being used for animal and human images. The race for higher static magnetic fields was chosen as one of the recent trends in the first chapter. It is no wonder that higher magnetic fields bring the fundamental way to enhance the quality of MR images characterized as SNR. Although several parameters, such as RF coil selection, coil loss, noise level of electronic components, magnetic field strength, and acquisition time, can affect SNR as expressed by (3-1). One of the dominant factors is the strength of a static magnetic field (B_0) given by (3-2) [51]

$$SNR \propto (coil\ factor) \times (magnetization\ factor) \times (sampling\ factor) \quad (3\text{-}1)$$

$$SNR \propto \frac{B_0^2}{\sqrt{\alpha_s B_0^2 + \alpha_c B_0^{1/2}}} \implies SNR \propto B_0 \quad (3\text{-}2)$$

where α_s and α_c are constants depending on the geometry of the sample, the coil, and their conductivities. In equation (3-2), the sample's resistance becomes larger than that of the coil as the strength of the main magnetic fields (B_0) increases. Therefore SNR becomes proportional to B_0 [51].

However, as the ultra-high fields drive MRI technology, engineering challenges and difficulties emerge from the design steps in the use of the higher frequencies.

3.2 Loading (Body) effect

RF coils have an inevitable characteristic, the loading (body) effect, as shown in Figure 3-1. Figure 3-1 (c) and (d) show the loading (body) effect resulting in the change of the resonance frequency and the quality factor (Q) from the pre-set condition due to the impedance mismatch when a human body is loaded (see Figure 3-1 (b)). The major reason for this degradation is the variation of the current flow on the RF coil due to the loading (body) effect [37,38]. After loading, the reflected power level becomes significantly high unless re-tuning/matching is done, and it provides less RF excitation causing low image qualities as well as system safety issues due to high power reflections. Broadband design reduces the loading (body) effect to the minimum, but it is not suitable

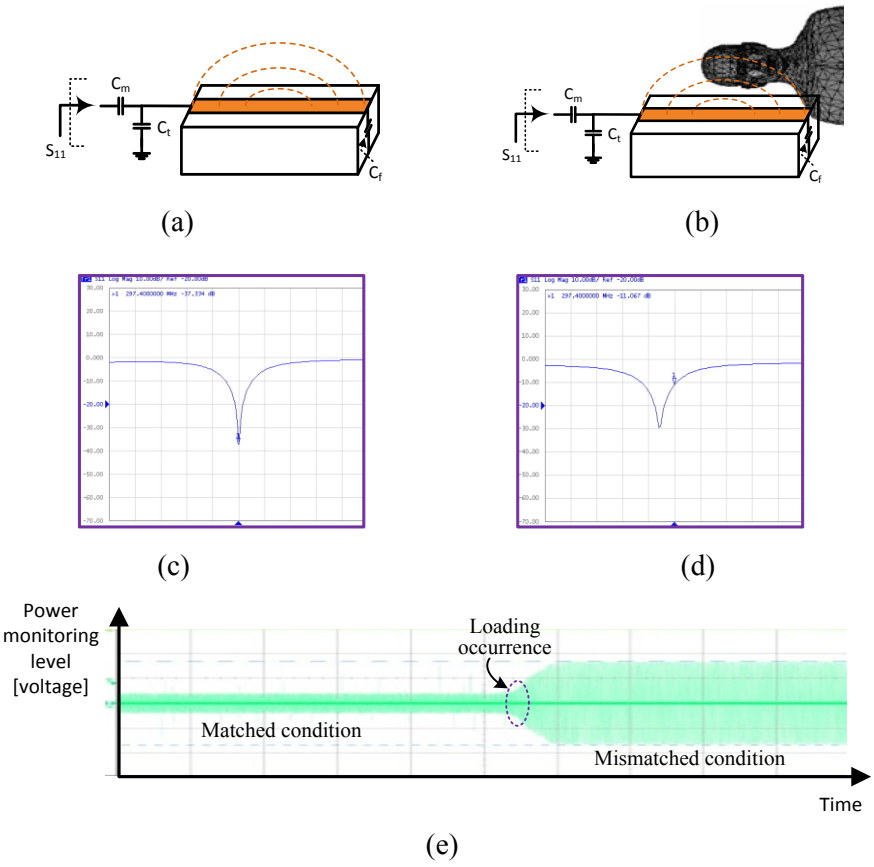

Figure 3-1. (a) Unloaded condition and (b) loaded condition: (c) reflection coefficient S_{11} in unloaded condition, (d) loaded condition, and (e) the reflected power level over time associated with unloaded and loaded conditions.

for the RF coils of MRI applications because MR images are obtained by very finely defined frequency by the Larmor frequency formula. In addition, RF coils must resonate at the same frequency. The resonance frequency is shifted down about 1~3%, and the corresponding power loss of 5~20% occurs when the human body is loaded on the RF coils. Such variation depends on the shapes, sizes and tissue components as well as the distance between the RF coil and the sample. Most importantly, it is hard to estimate before the loading and observation. Figure 3-2 shows the reflection coefficient (S_{11}) by varying the sample's condition considered different phantoms and placements. For example, -30dB is almost zero power loss, -20 causes about 1%, and -10dB causes about 10%, respectively. In the high power system, the reflected power with the 10% cannot be ignored.

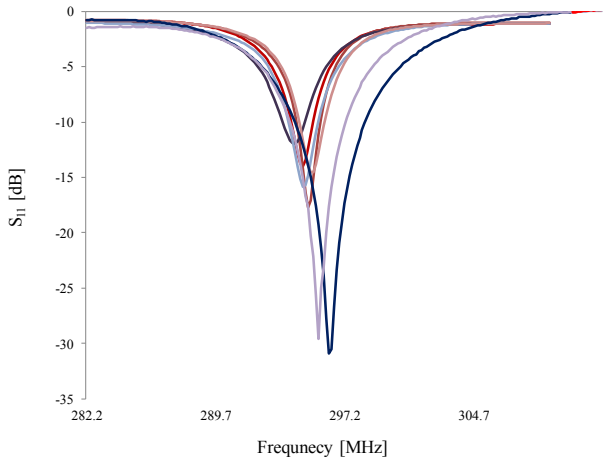

Figure 3-2. Reflection coefficient (S_{11}) according to the various loading (body) conditions for 7T (f_{Larmor} = 297.2MHz).

Figure 3-3 shows the loading (body) effects at the low frequency range in (a) and at the high frequency range in (b) with the reflection coefficient (S_{11}). As seen in S_{11}, the loading (body) effects can be a serious problem at the high frequency range because even little frequency shifts make a significant change of the reflection coefficient associated with the RF power efficiency and its safety. For example, when approximately 3~9MHz of the resonance frequency is shifted down from the initially tuned and matched

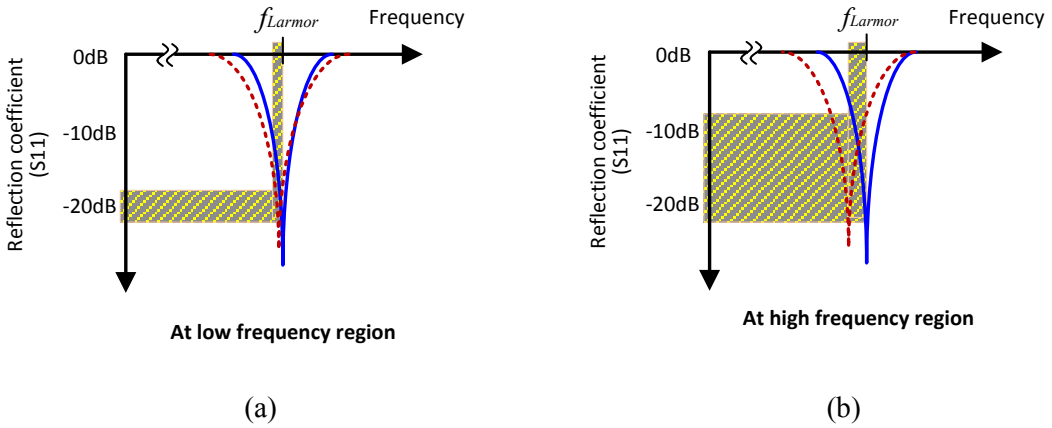

(a) (b)

Figure 3-3. Loading (body) effects with reflection coefficient: (a) at low frequency range, (e.g. 1.5T) and (b) at high frequency range, (e.g. 7T or 9.4T).

condition at 7T, it causes over 10dB differences in S_{11} and 50~200W RF power loss in case of the RF input power of 1kW. However, when roughly 1MHz frequency shift down occurs at 1.5T, it can be in the acceptable range of RF coil's performance.

Consequently, RF coils cannot efficiently generate the local magnetic fields without re-tuning and re-matching after a patient is loaded in the ultra-high field MRI systems. To avoid this problem, the manual re-tuning and re-matching by adjusting trimmer capacitors is the only method, and it takes a few minutes per channel. This, therefore, is a critical drawback in the high fields and high Qs applications of the modern MRI systems. Most works in this dissertation concentrate on finding the solution to prevent this loading (body) effect.

3.3 RF effect in MR images

Although higher static magnetic fields can improve the MR image quality, one of the major problems in ultra-high fields is the intrinsic non-uniformity in the MR images. RF coils generate the local magnetic fields (B_1) by the current distribution in its conductor of the resonator, e.g. the copper strip on the low loss dielectric substrate. When the wavelength by the Larmor frequency formula (referred to equation 2-7) becomes shorter than the dimension of the object, the current distribution on the conductor follows the

wavelength pattern, and the overlapped phases of RF signals make a bright or a dark spot in the MR images. Therefore, B_1 produced by the RF coil has the inhomogeneity in the image as shown in Figure 3-3. As the wavelength becomes shorter, the inhomogeneity in the images can be identified at the magnetic fields higher than 4T [8]. Furthermore, the human body has several ten times higher effective permittivity (ε_{eff}), e.g. ε_{eff} = 50 ~ 100, compared to that in the air, so it results in much shorter wavelength, $\lambda_{in\ vivo}$, in vivo and the severe RF effects in vivo by equation (3-3). For example, wavelength is about 1m in the air, but it is about 11cm in vivo at 7T.

$$\lambda_{in\ vivo} \propto \frac{\lambda_0}{\sqrt{\varepsilon_{eff}}} \tag{3-3}$$

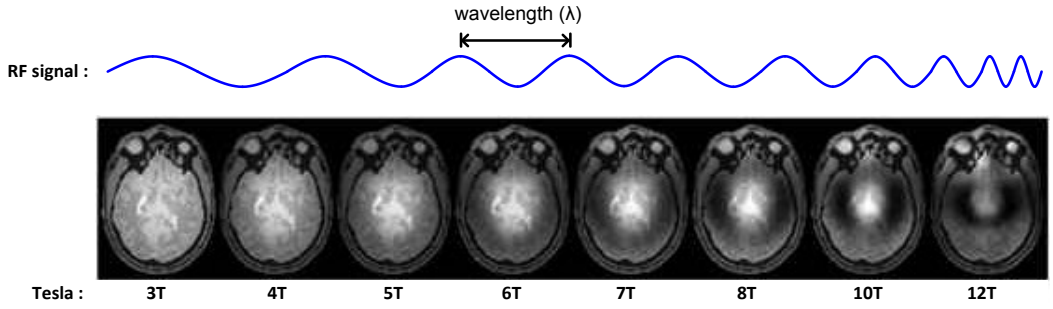

Figure 3-4. Wavelength effects are increased according to the strength of static magnetic fields (B_0). (image captured from [8])

3.4 RF effect in RF/electronic circuits

In the same way of the RF effect in MR images, the short wavelength affects the use of RF/electronic components for the design of RF coils. The wavelength of the Larmor frequency becomes significantly shorter and approaches the dimensions of RF/electrical devices, such as the block of RF Tx/Rx switches and low noise pre-amplifiers in the RF receiver. In high frequency applications, circuit elements such as PCB trances, cables, connectors, IC's can act as antennae [37,38]. These unintentional transmitter or receiver can cause problems. Although the region of interest is inside the RF coils, and the use of

the near-field applications is utilized in MRI systems, RF electromagnetic interferences caused by RF coils is no longer negligible in respect of RF/analog circuit design to build versatile functions to meet the recent RF/electrical demands. Every component can be a receptor receiving RF signals from the RF coil or can be a transmitter making electromagnetic interferences coupled with adjacent components. Furthermore, as mentioned earlier, various new approaches with RF/electronic circuits have been being examined. For example, a new technology allows a part of the RF receiver in nearby RF coils, and some special circuits such as power monitoring or automatic control of impedance have been being implemented inside the RF coil part. Moreover, multi-channel coils need a few of circuits affected by RF interferences. Therefore, protection or compensation for electromagnetic interference should be considered. It, however, is very hard to build the environment for RF immunity in the design of RF/electronic circuits supporting RF coils.

In addition, Table 3-1 presents the cable loss according to the cable length and the magnetic field strength. A few tens of meters are usually required to connect between the RF coils and amplifiers. Since the cable loss is a linear function of the length and frequency, even a coaxial cable is perfectly matched to 50Ω (VSWR = 1), a long coaxial cable with 20m has approximately 4~5dB signal loss, and it lowers power efficiencies. For example, the power efficiency is just approximately 35% when a 20m cable is used at 7T. Moreover, the loss term of a cable is increased if there are impedance bumps (mismatches) in the cable connections. In other words, any connection between the components should be matched very carefully to desired impedance, typically 50Ω, at higher frequencies.

Table 3-1. The loss data of the coaxial cables.

	1.5T		7T	
	5m	20m	5m	20m
Cable loss [dB] @ load SWR:1 (the perfect match condition)	0.49	1.95	1.16	4.63
Cable loss [dB] @ load SWR:2	0.6	2.26	1.38	5.08

Chapter 4. **RF coil design with automatic impedance tuning and matching**

4.1 Overview

This chapter is the main project of this dissertation concerning the automatically controlled frequency tuning and impedance matching for the RF head coil design. As mentioned in the introduction chapter, the loading (body) effect is something we definitely have to deal with in ultra-high field MRI systems, and the present method, manual tuning and matching, needs a long period of time to restore the impedance and frequency condition to the pre-set condition. To avoid these problems and find the best solution, the RF coil design based on the TEM structure, the connectivity to the existing MRI system, the impedance matching circuits, the RF power measurement circuit, the PIN diode switching circuit / driver, the digitally controlled capacitor arrays, the main

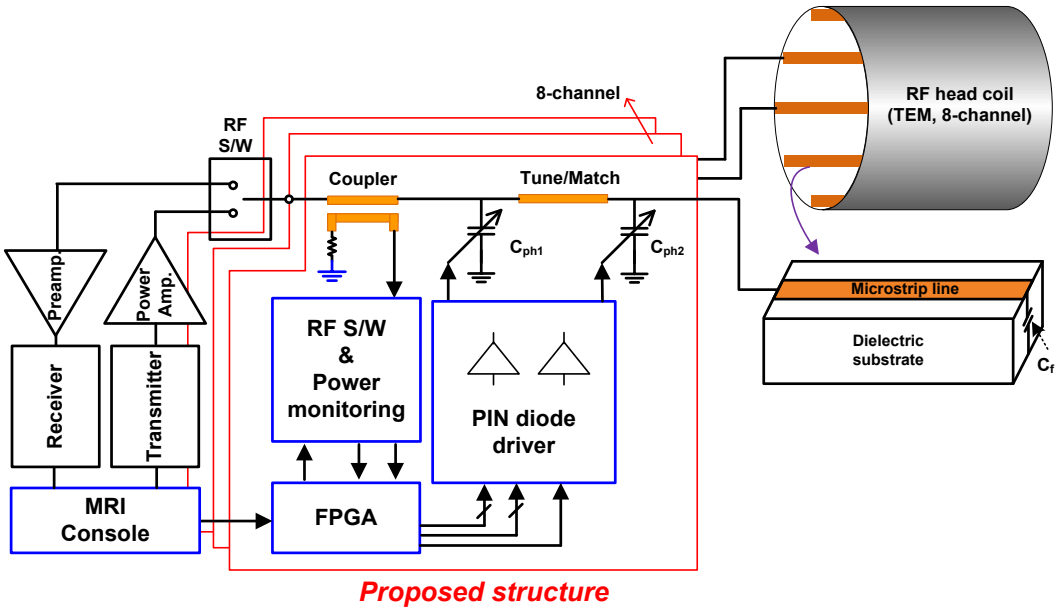

Figure 4-1. System schematic diagram with the automatic matching and tuning unit supporting the 8-channel RF head coil.

control logic design based on the FPGA, etc. have been studied. Figure 4-1 shows the proposed system schematic diagram containing the above-mentioned units with an existing MRI console and RF front-ends. From now on, each unit will be introduced in detail.

4.2 Microstrip transmission line (TEM) element

The microstrip transmission line (TEM) element becomes a popular element for multi-channel RF volume coil designs in ultra-high field MRI systems because the TEM structure can overcome the limitation of the use of the birdcage volume coils in high frequency applications. In multi-channel transceiver coils, the TEM element allows for bi-directional current path and a simple structure due to a short electrical length.

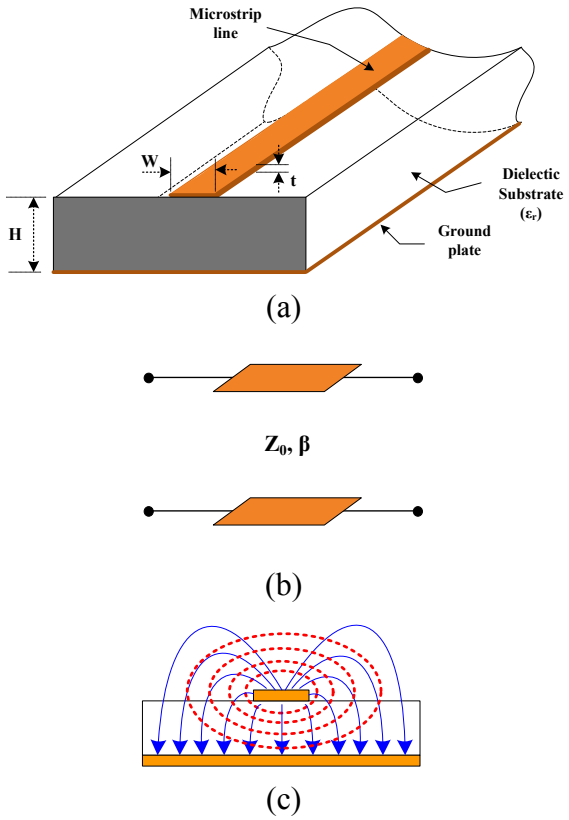

Figure 4-2. (a) Sectional diagram of a single TEM element, (b) a simple equivalent model, and (c) electric (solid-line) and magnetic field (dotted-line) lines.

4.2.1 Characteristics of the mircostrip transmission line

The TEM element is formed by a low loss dielectric substrate between a microstrip line and a ground plate as illustrated in Figure 4-2 (a) where H is the height from the microstrip line to the ground plate, and W is the width of the TEM element, and a simple equivalent model of the TEM element is depicted in Figure 4-2 (b) where Z_0 and β are the line's characteristic impedance and the propagation constant, respectively. Due to its specific semi-open transmission line structure, substantial electromagnetic energy is stored in the area near the strip conductor line. This results in reducing the radiation losses and preserving the current uniformity in circuits exceeding of one-tenth the wavelength of its operating signal at high fields. The rule of thumb for any resonant circuit in the electronic circuits and systems is: "when circuit length exceeds 0.1λ, use a transmission line." The characteristic impedance, Z_0, and the propagation constant, β, of the TEM resonator element can be calculated according to the equations (4-1) and (4-2). The characteristic impedance is an important specification that needs to be determined. Traditionally, the microstrip width is minimized to decrease the overall dimensions as well as to suppress higher order modes [43]. However, in the design of RF coils, this design criterion is not needed because the primary purpose of the RF coil involves coupling the magnetic energy (H-field) to the human body in the near-field, so the characteristic impedance can be varied to obtain optimal magnetic field propagation. In designing these transmission lines, the synthesis of design revolves around the ratio between width (W) and height (H). The TEM element has an asymmetric structure between the microstrip line and the ground plate as shown in Figure 4-2 (a). Therefore, the effective dielectric constant, ε_{eff}, of the TEM element should be considered in characterizing different parameters related to the TEM resonance element instead of the relative dielectric constant, ε_r, of the substrate. In addition, most TEM elements have the ratio W/H is less than unity. The expression of the effective dielectric constant and the characteristic impedance in unloaded case can be given by

$$\epsilon_{eff} = \begin{bmatrix} \frac{\varepsilon_r+1}{2} + \frac{\varepsilon_r-1}{2}\left[\frac{1}{\sqrt{1+12\left(\frac{\mathrm{H}}{\mathrm{W}}\right)}} + 0.04\left(1-\frac{W}{H}\right)^2\right] & if\ \frac{\mathrm{W}}{\mathrm{H}} < 1 \\ \frac{\varepsilon_r+1}{2} + \frac{\varepsilon_r-1}{2}\left(1+\frac{12\mathrm{H}}{\mathrm{W}}\right)^{-0.5} & \text{otherwise} \end{bmatrix} \quad (4\text{-}1)$$

$$\mathrm{Z_o} = \frac{Z_f}{2\pi\sqrt{\varepsilon_{\mathrm{eff}}}} \ln\left(8\frac{\mathrm{H}}{\mathrm{W}} + \frac{\mathrm{W}}{4\mathrm{H}}\right),$$

$$\text{where } Z_f = \sqrt{\mu_0/\varepsilon_0} = 376.8\Omega \text{ in free space} \quad (4\text{-}2)$$

If there is distributed capacitive termination (C_f) on a TEM element for reducing the length of the TEM element, the characteristic impedance and other parameters should be modified as equation (4-3) where CF is the correction factor depending on a termination capacitance, a capacitance of a TEM per unit length, C_0, and the effective length, L_{eff}, considered fringing effect .

$$\mathrm{Z_{o_{capacitive\_termination}}} = \frac{Z_0}{\mathrm{CF}} \quad (4\text{-}3)$$

$$\text{where } \mathrm{CF} = \sqrt{1+\frac{\mathrm{C_f}}{\mathrm{C_0 \cdot L_{eff}}}},\ \mathrm{C_0} = \frac{2.6378\times10^{-11}(\epsilon_{\mathrm{eff}}+1.41)}{\ln(\frac{5.98\mathrm{H}}{0.8\mathrm{W}+\mathrm{t}})},\ \mathrm{L_{eff}} = \mathrm{L} + 2\Delta\mathrm{L_m},$$

$$\text{and } \Delta\mathrm{L_m} = 0.412\mathrm{H}\frac{(\epsilon_{\mathrm{eff}}+0.3)\left(\frac{\mathrm{W}}{\mathrm{H}}+0.264\right)}{(\epsilon_{\mathrm{eff}}-0.258)\left(\frac{\mathrm{W}}{\mathrm{H}}+0.8\right)}$$

If λ_o is the free-space wavelength, the wavelength of the wave component along the microstrip is given by

$$\lambda = \frac{\lambda_0}{\sqrt{\varepsilon_{\mathrm{eff}}}} \quad (4\text{-}4)$$

4.2.2 A configuration of the TEM resonator element for RF coils

In the RF coil design, a TEM resonator is useful and has the best B_1 field distribution if the length of the microstrip line is closing to the half-wavelength. When the half-

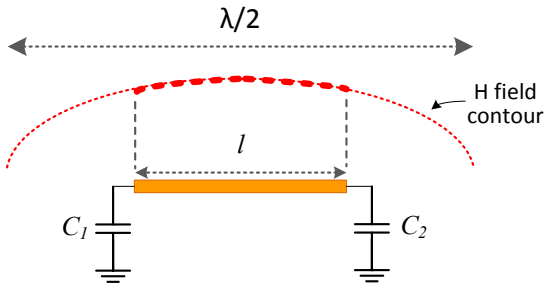

Figure 4-3. B_1 field distribution of a capacitively terminated microstrip line.

wavelength TEM resonator element has open-circuit terminations, the maximum voltage occurs at the ends and the maximum current occurs at the center of the microstrip line. This length, however, is impractical to build a practical RF coil. Therefore, Figure 4-3 introduces the capacitive termination method to reduce the electric length resulting in the reduction of a practical size of a TEM resonator, and it also provides more uniform B_1 field distribution [21]. The input impedance of the capacitively terminated microstrip resonator is given by

$$Z_{in} = \frac{Z_{C_1} Z_0 (Z_{C_2} + jZ_0 \tan(\beta l))}{Z_0 (Z_{C_1} + Z_{C_1}) + j(Z_{C_1} Z_{C_2} + Z_0^2) \tan(\beta l))} \tag{4-5}$$

where β (=2π/λ) is the phase constant, l is the length of the microstrip line, Z_0 is the characteristic impedance of microstrip line, Z_{C1} is $1/j\omega C_1$, and Z_{C2} is $1/j\,\omega C_2$.

To meet the resonance condition ($Z_{in} \rightarrow \infty$), a denominator should become an infinite. In case both capacitances are identical ($C = C_1 = C_2$), the capacitance value can be derived from equation (4-5)

$$C = \frac{\cos(\beta l) + 1}{\omega_0 Z_0 \sin(\beta l)} \tag{4-6}$$

From this equation, (4-6), a tuning capacitor value can be estimated when the dimensions of the microstrip line associated with β, l, and Z_0 are first fixed.

4.3 Impedance matching and frequency tuning of TEM resonator element

By the fundamental RF theory, the impedance matching is the mandatory criterion in RF circuit design. The impedance matching results in the maximum power efficiency from a power source to a load and the minimum noise figure vice versa in general wireless systems. The impedance matching commonly involves the aforementioned frequency tuning.

Figure 4-4 shows the basic conjugate impedance matching method. The maximum power is transferred from a source to a load only if the impedance from the signal source, $Z_{Conj} = R_L - jX_L$, is equal to the complex conjugate of the load impedance, $Z_{Load} = R_L + jX_L$ as shown in Figure 4-4 (a). This is called the complex conjugate matching. In the same manner, Figure 4-4 (b) is also valid if matching network is ideal conditions meaning the use of ideal passive components. In such case, the direction of the power is an insignificant matter. It ideally implies a good impedance matching block allowing both low power loss in RF transmitter and high SNR in the RF receiver in the RF front-end of MRI system [37,38]. In reality, all passive components have loss terms, e.g. internal series resistance, and it bring the difficulty of the design in matching network

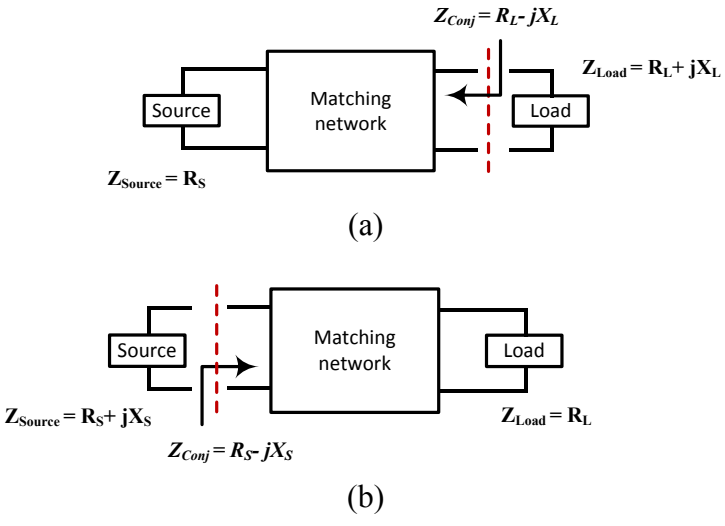

Figure 4-4. The conjugate impedance matching: (a) between a resistive source and a complex load and (b) between resistive load and a complex source.

circuits. When RF coil is connected to power amplifier or low noise pre-amplifier as shown in Figure 4-5 (a), the impedance between both sides must be matched (generally 50Ω) to enable the delivery of maximum power efficiency from the source to the load or it must be matched to minimize reflection

A mentioned above, the use of a term 'matching' and 'tuning' is often confused, or they mean the same thing. The matching, however, is defined as the impedance matching, and the tuning is defined as the frequency tuning, respectively, in the RF coil analysis. RF coils based on the TEM resonator also follows this processes.

The roles of the impedance matching is to deliver the maximum power from a source (power amplifier) to a load (RF coil) for RF transmitting, and improve the signal-to-noise (SNR) from a load (RF coil) to a receiver (Low noise pre-amplifier) during RF receiving as seen in Figure 4-5 (a). In addition, the impedance matching can protect RF devices (passive and active elements, e.g. capacitors or RF T/R switch circuits) from the reflected high RF power (typical a few Watt range in RF coils) that builds standing waves containing the phase and amplitude (i.e. voltage or current). The amplitude of waves can be either subtracted or added due to the different phases. If the standing wave with the maximum of amplitudes is positioned and applied to a certain device, the device may be destroyed.

The frequency tuning is for adjusting the resonance frequency rather than the impedance matching. The process of this frequency tuning may affect the impedance matching condition, but the impact is certainly lower than the one of the impedance matching process.

Figure 4-5 (a) shows the typical TEM element containing an L matching network circuit with two capacitors. As seen in Figure 4-5 (b), the input impedance (Z_{coil}) of the RF coil element including matching (C_m) and tuning (C_t) capacitors should be placed on the center of Smith chart for the impedance matching. The trace of impedance rotates about two third of outer circle from the open status with almost lossless property, and a fixed value capacitor (C_f) takes a share of this trace. There are two different dominant functions (tuning and matching), and two processes are not independent. However, both

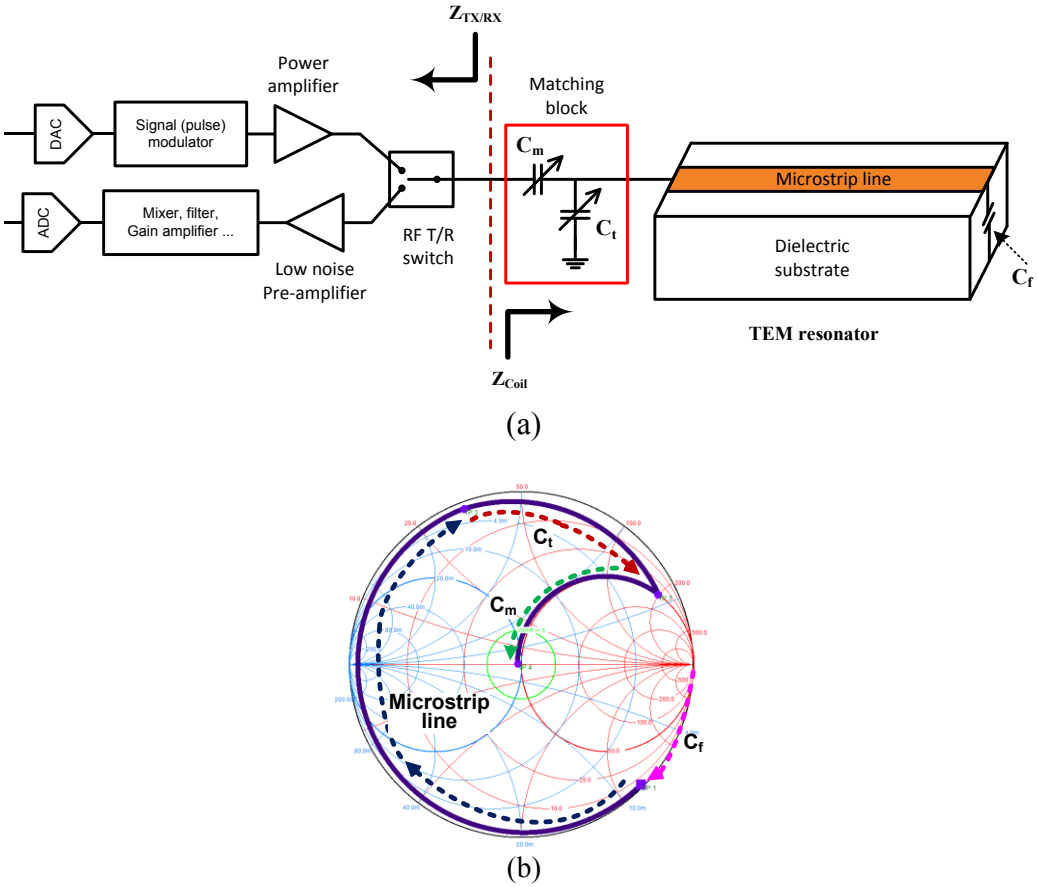

Figure 4-5. (a) A typical TEM element and RF front-end circuits and (b) impedance matching and tuning steps of the typical TEM resonator.

effects can be seen as the same in the reflection coefficient (S_{11}), but a degree of the influence is significantly different as shown in Figure 4-6 (a) and (b). The impedance matching and the frequency tuning of most RF coils follows these two procedures, and the combination of both makes the commonly called impedance matching status. Furthermore, by comparing Figure 4-6 (a) and (b), it is clear that the adjustment of the tuning capacitor (C_t) has the priority because the error in the tuning capacitor's manipulation make worse.

There are various configurations to build matching network circuits. An L matching network, in general, is popular in the RF coil design. Two capacitors are employed. One dominantly plays a role in the impedance matching process, and another is in charge of

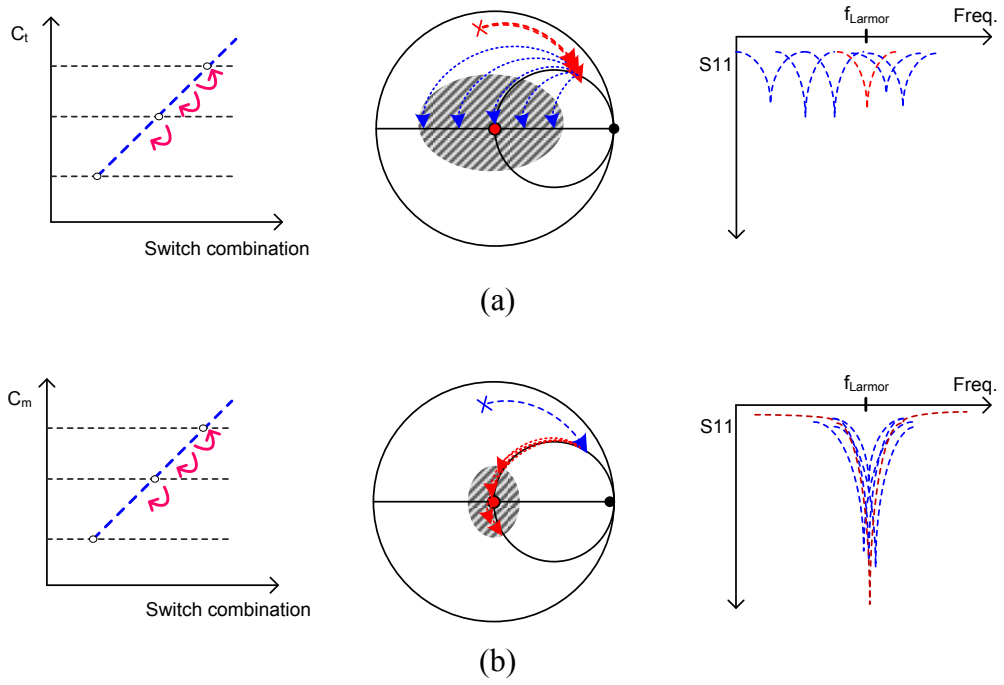

Figure 4-6. The conceptual (a) frequency tuning and (b) impedance matching procedure: adjusting capacitances and corresponding reflection coefficients (S_{11}).

the tuning process. A discrete inductor element is barely used in RF coil designs due to the loss and radiation issues. This simple L matching network successfully has accomplished the matching and tuning in the existing RF coils, but it can be problematic when additional functions are tried.

The next part explains the reason why the proposed microstrip Pi matching circuit has been utilized instead of the traditional L matching circuit.

4.4 microstrip Pi matching network for the RF coil design

In this project, the microstrip Pi matching network has been chosen to reduce the physical size and increase the performance supporting capacitor arrays of the final automatic matching and tuning unit. Before applying this Pi matching circuit with capacitor arrays, the simple Pi matching without capacitor arrays has been manufactured and evaluated for a RF coil matching circuit [56].

4.4.1 Microstrip Pi matching network

Each element in a TEM coil is a half-wavelength transmission line, fore-shortened by adding capacitors shunt at both ends, and these capacitors are presented in a TEM coil element shown in Figure 4-7. The traditional RF coil element that is terminated to the two trimmer capacitors: matching capacitor (C_m) and tuning capacitor (C_t) at one end and a fixed value capacitor (C_f) at the other as shown in Figure 4-7 (a). This creates a distributed LC resonant circuit whose natural frequency can be adjusted with the trimmer capacitors to accommodate changes in the loading of the microstrip line by the sample, the human body. In Figure 4-7 (b), Pi matching circuit consists of two capacitors connected to the ground in parallel and microstrip line between the capacitors to obtain the optimal inductance. It is clear that the Pi matching network should be applied when additional functions are required because L matching for adding function blocks like

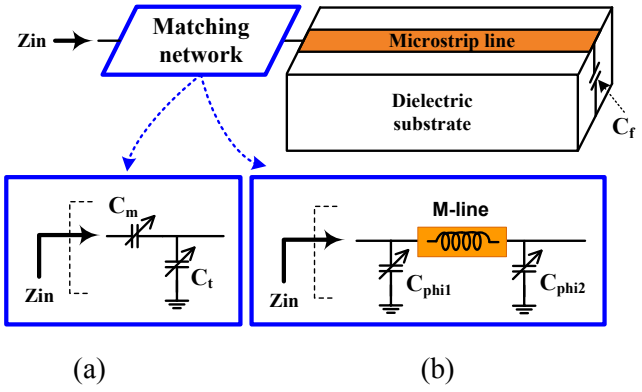

Figure 4-7. The RF microstrip transmission line coil element with (a) the conventional L-matching technique and (b) proposed Pi matching network.

capacitor arrays for the auto-tuning and matching become bulky and large loss part in the main signal path as shown in Figure 4-8 (a) and (b). Since the substrate has relatively high loss tangent (δ), e.g. δ=0.0021 (Rogers RO4003C material), in dielectric material, the microstrip line is also lossy. However, series connected components (e.g. capacitors and PIN diodes) on a microstrip line can be a more significant loss and mismatch term in a RF resonant circuit [58]. Equivalent series resistance (ESR) of capacitors used in the

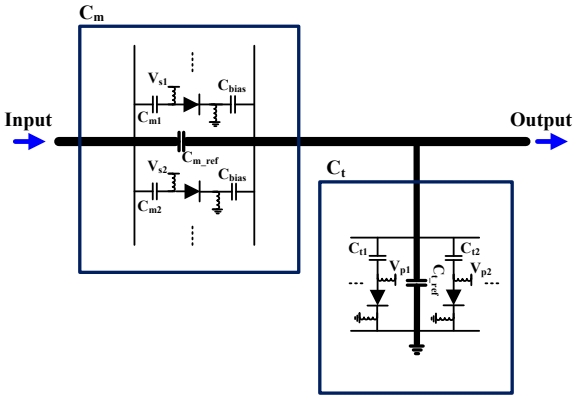

(a)

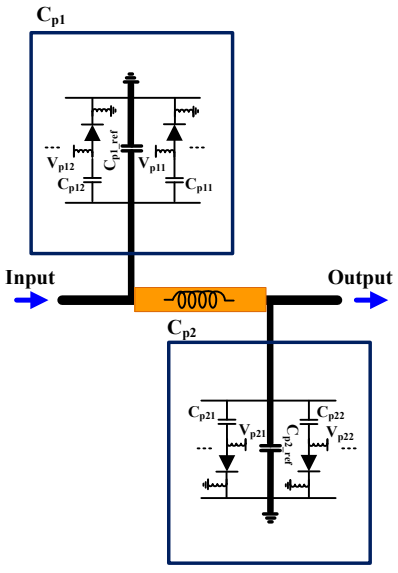

(b)

Figure 4-8. Matching and tuning network applied capacitor array using (a) a traditional L network and (b) microstrip Pi network.

RF coil design is about 0.3Ω to 0.5Ω. Because the quality factor (Q) of capacitors is smaller, and equivalent series resistance becomes larger as the operating frequency is higher, the series connected capacitor is disadvantageous at higher operating frequencies [58]. The size and physical construction of a capacitor also may disturb the electromagnetic field distribution on a transmission line as to cause an impedance bump or mismatch at that point. This, and the series resistance internal to the capacitor, changes the impedance of the line at the input to the capacitor. Moreover, the range of capacitances of a series connection in L-matching is about 1pF to 5pF generally. This range is too small values to implement the capacitors array bank due to parasitic capacitances and inductances. Microstrip Pi matching network, however, doesn't have any component on the main signal line, so it can reduce the physical size from the signal input to output. Therefore, there is not any impedance bump or connection loss in the microstip Pi matching network circuits.

4.4.2 Impedance matching and tuning steps of the Pi network

Figure 4-9 (a) shows the TEM element using the mircrostrip Pi matching networks,

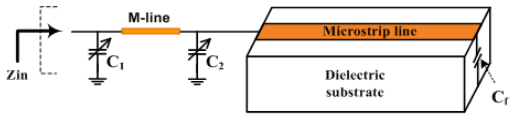

(a)

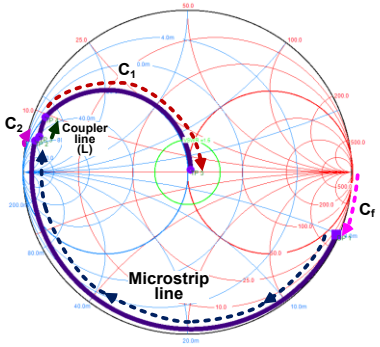

(b)

Figure 4-9. (a) A TEM element with Pi matching network and (b) impedance matching and tuning steps

and (b) present the steps of impedance matching and tuning on the Smith chart. By circuit simulation using ADS (Agilent), capacitor values are calculated as well as the dimensions of microstrip line that will serve as an inductor in this Pi matching network. These values are directly dependent on the choice of the dimensions of the microstrip TEM resonator element.

4.4.3 Evaluation of the microstrip Pi network circuit at 7T

4.4.3.1 Volume head coil design with the microstrip Pi network

An 8-channel 7T RF head coil was built in Figure 4-10. To find the optimal coil parameters, S_{11} and S_{21} using decoupling probe are measured and checked the symmetric propagation along with the length of the conductor on the TEM resonator in the test bench with a network analyzer. From S_{21} measured data, the tail capacitances (C_f) have been varied. All results were acceptable as the alternative matching method of RF coil with lower loss and lower sheath current as well as homogeneity.

4.4.3.2 Experimental setup and results

Experiments to obtain the S-parameters and B_1^+ maps were performed with a cylindrical phantom with 8 liter sucrose / saline (ε_r = 58.1and σ = 0.539 S/m) that was positioned at the same location for each experiment. Figure 4-11 shows the performance of the RF coil element with the proposed Pi matching network. Q is measured with two single coil elements applied the standard L and proposed Pi matching structure. The Q of the standard coil with the traditional L matching was 70.7 and another coil with the

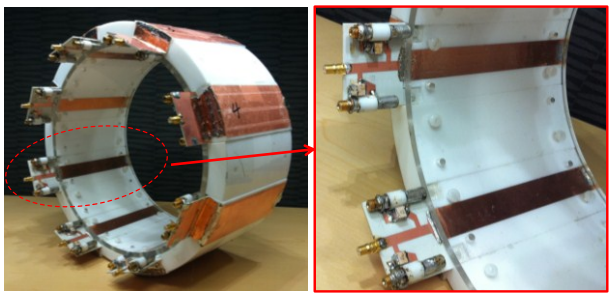

Figure 4-10. 8 multi-channel RF coil with Pi matching network and (b) highlighted RF coil element.

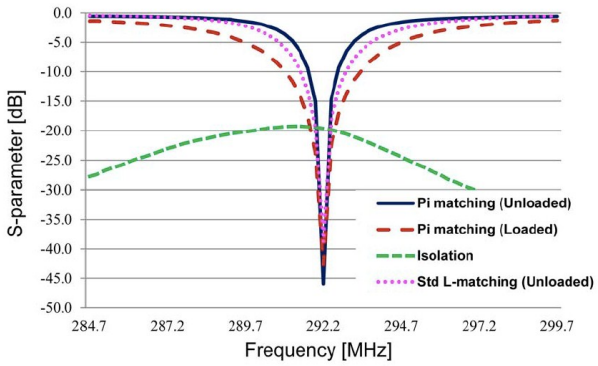

Figure 4-11. Experimental results of S-parameters

proposed Pi matching was 106.2. It demonstrates that the transmission loss of Pi matching is less than the traditional structure because of no components on the RF signal line. The Q value of the loaded condition was 39.1, so the ratio between unloaded and loaded condition was 2.72. It means this RF coil couples with the sample well. Isolations between coil elements are -17dB ~ -22dB without a decoupling method between adjacent coil elements. Additionally, Pi matching network can significantly reduce sheath current

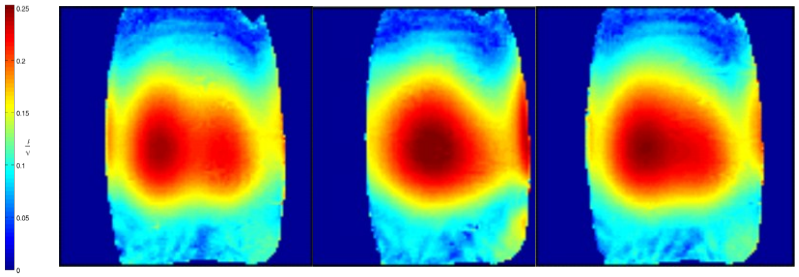

(a)

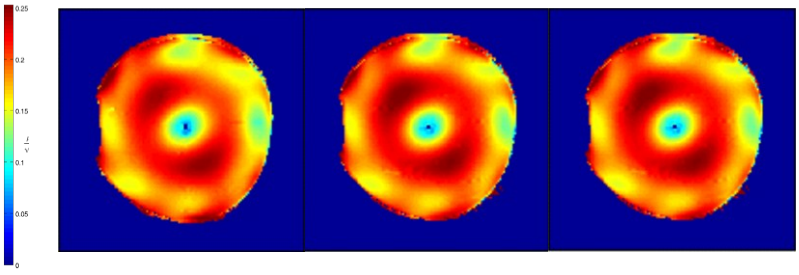

(b)

Figure 4-12. Experimental results: Series of central (a) coronal and (b) axial B1+ map (μT/sqrtW) slices.

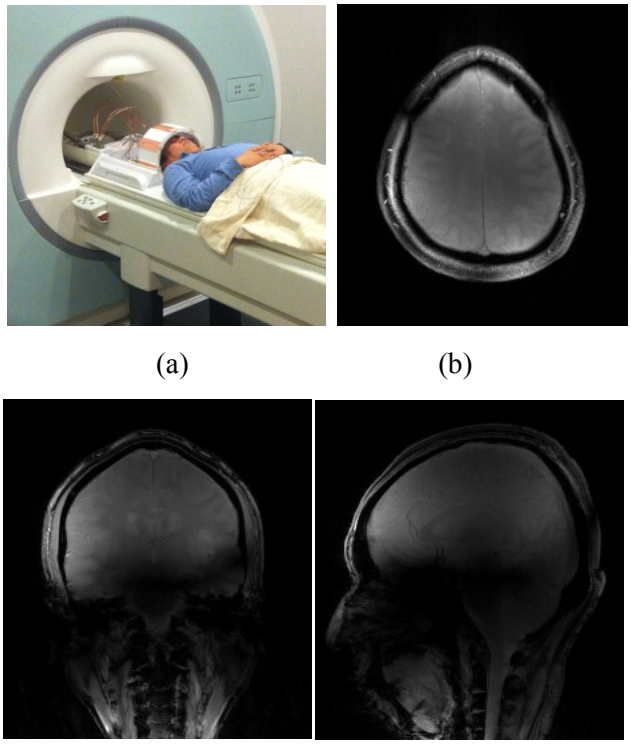

(a) (b)

(c) (d)

Figure 4-13. Experimental setup and Gradient Echo image results: (a) MR scanning setup, (b) axial view, (c) coronal view, and (d) sagittal view of MR images

compared to L matching network due to the balanced circuit configuration, thus it was easier to adjust matching and tuning capacitances when a load was changed.

Figure 4-12 shows the experimental MR image results of the series slices in the central region of the phantom. Homogeneity and symmetric field distribution were searched. Figure 4-13 (a) show an experimental setup of 7T MRI scanner (f = 297.2MHz, Siemens Magnetom 7T) to take the human head images and MR imaging performance was evaluated using Gradient Echo pulse protocol, resolution = 1x1mm, TR (repetition time) / TE (echo time) = 175/4 ms, slice thickness = 5mm to acquire MR image slices in axial, coronal, and sagittal view in Figure 4-13 (b), (c) and (d), respectively. The images demonstrate good penetration and coverage. It shows very symmetric and homogeneity so these results validate that the microstip Pi matching network in RF coils design can be acceptable to ultra- high field MRI systems with the high RF power.

4.5 PIN diode switch application

4.5.1 PIN diode switch

Switches that control the path of the RF high power for MRI applications (64MHz ~ 500MHz) are the most common application of PIN diodes. PIN diodes are three layer diodes, comprised of a heavily doped P-type layer (anode) and a heavily doped N-type layer (cathode) separated by a virtually undoped intrinsic layer. Under forward bias, charge carriers from the P and the N layers are forced into the intrinsic layer, which reduces its RF impedance. When a reverse bias, voltage bias is applied across the PIN diodes, all free charge carriers are removed from the intrinsic layer, thereby causing its RF impedance to increase. This variable RF impedance versus DC bias allows the diode to be used in RF switching circuits, in which the PIN diode is either heavily forward-biased or reverse-biased. Therefore, the PIN diode is essentially a variable resistor. Figure 4-14 shows a simple PIN diode switch circuit that can provide reasonably low insertion loss (I_L) depending on the series resistance (R_S) of the PIN diode by (4-5). This is one of the major issues in the RF coil design with electrically controlled capacitor array (referred to Figure 4-8) because many PIN diodes are used, and the overall loss must be low. Another contribution of PIN diodes is high isolation (I_{SO}) property in the reverse bias state in (4-7). It allows keeping the constant capacitances according to the combination of the PIN diode switches to turn on or off capacitor branches. Overall, the maximum RF power rate considered as the limiting factor is defined by (4-8) [65].

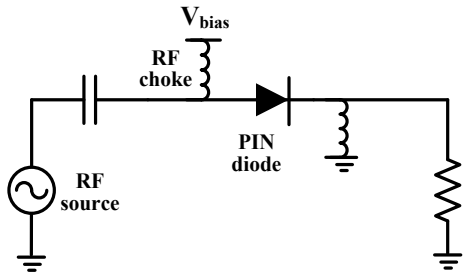

Figure 4-14. Simple PIN diodes switch circuit.

$$I_L = 20\log\left(1 + \frac{R_S}{2Z_0}\right), \qquad I_{SO} = 10\log\left(1 + \frac{1}{(4\pi f C_t Z_0)^2}\right) \tag{4-7}$$

$$P_d = \left(\frac{4R_S Z_0}{(2Z_0 + R_S)}\right)^2 P_{av} \quad [Watt] \tag{4-8}$$

where Z_0 is the characteristic impedance (typically 50Ω) of the input power source, f is the operating frequency, Ct is the diode total capacitance, and P_{AV} is the maximum available power, $V_g^2 / 4Z_0$ (watt). These equations are under the matched condition. In addition, a peak RF voltage and current applied at the PIN diode switch is given by

$$I_P = \sqrt{\frac{2P_{av}}{Z_0}} \ [A], \qquad V_p = \sqrt{8Z_0 P_{av}} \ [V] \tag{4-9}$$

PIN diodes, like all diodes, are nonlinear devices in their response characteristics, and as a result, they produce harmonics and intermodulation distortion (IMD). Fortunately, these products are usually at very low levels in a PIN diode switch because the diodes themselves are either in a saturated, forward-biased condition or are reversed-biased.

As mentioned above, components to be used in MRI systems need severe requirements: high power handling capability (~ kW range), non-magnetic property. Thus, it is so hard to find a proper component in the market. Fortunately, M/A-COM technology solutions Inc. provides a PIN diode (MA4P7470F-1072T) with the non-magnetic property, the high power capability, and the low series loss. This diode is designed for 53dBm RF continuous wave input power, 150mA forward DC current driving, -800V reverse DC voltage, 0.7pF maximum total capacitance, and 0.8Ω maximum series resistance. These electrical specifications are not out of our demands to build capacitor arrays adjusting capacitances for the automatic matching and tuning unit.

4.5.2 PIN diode driver

A fundamental property of PIN diodes is their ability to control large RF signals with much lower values of DC current and voltage using two states of PIN diode driving circuits in which either a forward bias current or a reverse bias voltage. Therefore, pull up driving circuit for the positive bias (+V) and pull down driving circuit for the negative bias (-V) are designed as shown in Figure 4-15. Both driving circuits should be toggled between +V and –V without the overlapped time. In reverse bias condition, the instantaneous voltage (both RF and DC bias) across the PIN diode must not exceed its reverse breakdown voltage supplied by manufacturers. If the RF voltage swing exceeds this voltage, the driver should have sufficient reverse bias current capability to achieve

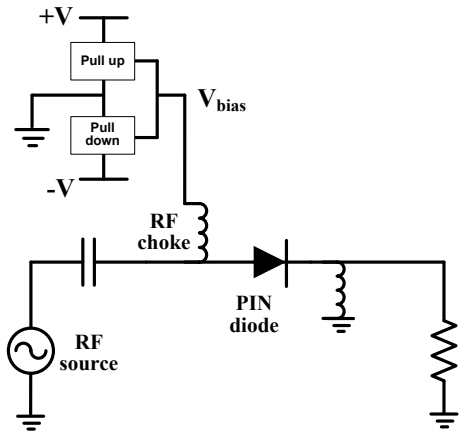

Figure 4-15. PIN diode driver and switching circuit

the desired switching speed, but it must also provide the excess reverse current required during the high power RF pulse. Under this reverse biased leakage condition, the PIN diode may heat appreciably causing an increase in the leakage current. If the leakage current is large enough, thermal runaway will cause the PIN diode to be destroyed [65].

In many applications, high applied reverse bias voltages are often problematic part to implement. Fortunately, the practical reverse bias does not require a full reverse bias (V_{bias}) condition to keep the safe switching region by equation (4-9) [66].

$$|V_{bias}| = \frac{|V_{RF}|}{\left[1+\left[\frac{0.0142\, f_{MHZ}\ (25W_{\mu m})^2}{V_{RF}\sqrt{D}\left[1+\sqrt{1+\left[{}^{0.056V_{RF}\sqrt{D}}/_{25W_{\mu m}}\right]^2}\right]}\right]^2\right]^{0.5}} \quad (4\text{-}9)$$

where V_{RF} is the RF voltage level, D is the RF pulse's duty cycle, and W is the intrinsic layer width.

By the equation (4-9), the requirement of the reverse bias voltage is less than the peak RF voltage, and the relationship between the reverse bias voltage and the intrinsic layer of PIN diode is depicted in Figure 4-16 [64]. From this graph, the PIN diode (MA4P7470F-1072T) used in this project has 140μm (≈ 5.5mil, 1mil = 25 μm) width of the intrinsic layer, and if 1kW (≈ $316V_{Peak}$) RF signal with low duty ratio and the 300MHz operating frequency are considered, the reverse bias voltage requires about $30V_{peak}$ instead of about $316V_{peak}$.

In PIN diode switching applications, diode's switching speed is the time required to either fill or remove charge from the intrinsic region between P-type and N-type layers. The switching speed depends both on the driver circuit's operating conditions for specific switching states and on the diode's equivalent circuit parameters, such as forward current, initial reverse current, and carrier lifetime. Fortunately, this project's requirement for the switching time is the milli-second (ms) range, and it can be ignored because most PIN diodes have a few micro-second (μs) ranges.

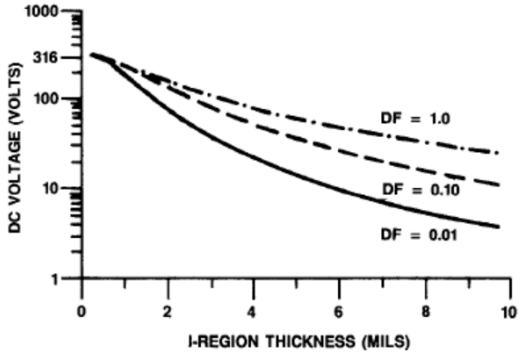

Figure 4-16. Requirement of DC reverse bias voltages vs. the intrinsic region (I layer) thickness and duty cycle for a 1kW RF signal at 1GHz [64].

4.6 RF power monitoring

To build the automatic matching and tuning system, RF power measurement is essential part. The main control circuit uses the information made by sampling RF power from the main RF signal path, and manipulates matching and tuning capacitor arrays based on PIN diode switch circuits to find the optimal switching combination in this study.

4.6.1 Reflection coefficient and VSWR

In the power measurement, the first term for the reflected power measurement is a reflection coefficient, usually denoted by the symbol gamma (Γ), given by (4-10)

$$|\Gamma| = \frac{V_{reflected}}{V_{forward}} = \frac{Z_L - Z_0}{Z_L + Z_0} \tag{4-10}$$

It is the ratio of the reflected signal voltage to the forwarded signal voltage, and also expressed by the impedances between the load and source. In last Figure 4-5 (a), some RF power is reflected and Γ becomes greater than zero if Z_{in} is not matched the impedance of the RF source (power amplifier), typically 50Ω.

Two more useful expressions are commonly used to describe the reflection measurement: VSWR (Voltage Standing Wave Ratio) and Return Loss (RL) in (4-11) and (4-12).

$$\text{VSWR} = \frac{V_{max}}{V_{min}} = \frac{1 + |\Gamma|}{1 - |\Gamma|} \tag{4-11}$$

$$\text{RL} = -20\log|\Gamma| = -20\log\frac{VSWR - 1}{VSWR + 1} \tag{4-12}$$

The ratio of the maximum to minimum voltage is known as VSWR, and a measure of how well matched a RF source (power amplifier) is to a RF coil element with a simple unit. The return loss is the measurement in dB of the ratio between the forward and reflected power. For example, a RF coil element with a VSWR of 2:1 would have a

Table 4-1. VSWR, return loss, % of power/voltage loss, and reflection coefficient vs. mismatch loss

VSWR	Return loss [dB]	% of power / voltage loss	Reflection coefficient	Mismatch loss [dB]
1	∞	0 / 0	0	0
1.15	-23.1	0.49 / 7	0.07	0.21
1.25	-19.1	1.2 / 11.1	0.111	0.54
1.5	-14	4.0 / 20.0	0.2	0.177
1.75	-11.3	7.4 / 27.3	0.273	0.336
2	-9.5	11.1 / 33.3	0.333	0.512
3	-6.0	25.1 / 50	0.5	1.25
4	-4.4	36.3 / 60	0.6	1.94
5	-3.5	44.7 / 66.6	0.666	2.55
10	-1.7	67.6 / 81.8	0.818	4.81
∞	0	100 / 100	1	∞

reflection coefficient of 0.33, a return loss of 9.5dB, and about 11% of power loss by table 4-1. If 1kW (60dBm) is applied to this RF coil element, the return loss would be 9.5dB. Therefore, 111 watts would be reflected and the rest 889 watts would be transmitted to generate B_1 fields. In this case, the reflected 111 watts cannot be ignored, and needs an impedance matching to reduce the reflection power. In general, RF coils of MRI system should have at least VSWR of 1.2 (≈ -20dB in the reflection coefficient) to keep the proper matching condition. The VSWR can be easily checked on the Smith chart by S_{11} measurements in a network analyzer as shown in Figure 4-17 (a). The main source of the RF power detector is the detectable VSWR level (green-colored dotted line) according to the load conditions as shown in Figure 4-17 (b) (VSWR = 1) and (c) (VSWR = 3), respectively. One thing that becomes obvious is that the ratio of Vmax to Vmin becomes larger as the reflection coefficient increases. That is, if the ratio of Vmax to Vmin is one, then there is no variation in VSWR, and the impedance of the RF coil is perfectly matched to the RF source. If the ratio of Vmax to Vmin is greater than unity, then there is a signal fluctuation that makes the VSWR. In the power measurement circuit respect, these VSWR signals are used to generate DC output voltages with a rectifier circuit. In other words, the RF power detection circuit offers the reference level when VSWR = 1, and the DC output of this circuit is a linear function with the VSWR levels.

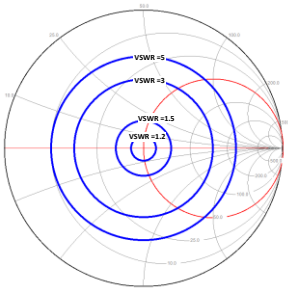

(a)

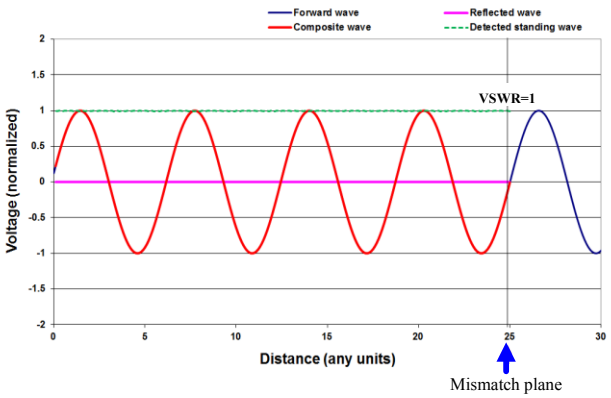

(b)

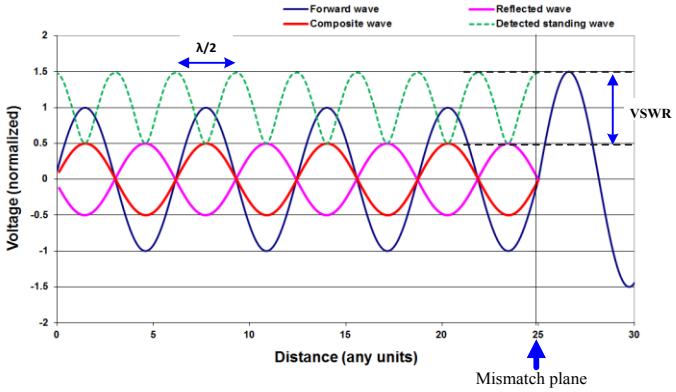

(c)

Figure 4-17. (a) VSWR circles on the Smith chart (b) forward, reflected, and detectable VSWR in the normalized voltage level (VSWR=1), and (c) VSWR=3.

4.6.2 Power measurement

RF input signals (i.e. VSWR signals in case of the power monitoring circuit) enter the power detect circuit that is consisted of a diode (typically Schottky diode), a capacitor, and a resistor as seen in Figure 4-18. Schottky diodes are characterized by fast switching times, low forward voltage drop, and low junction capacitance. This Schotty diode detector is a basic simple rectifier circuit which produces an almost DC output current or voltage that is proportional to the magnitude of the alternating input signal. In this circuit, the Schottky diode rectifies the input alternating signal and charges the output capacitor. In this project, a commercialized RF power detector package (LTC5507 by Linear technology) is used to reduce circuit size and get a stable power detection condition. It has wide input power range (-34dBm to 14dBm), wide input frequency range (100 kHz to 1GHz), and internal buffered output. Most specifications of this detector satisfy the demands of this project.

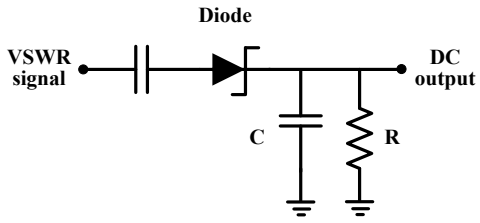

Figure 4-18. A simple diode power detection circuit

4.6.3 Coupler design

A coupler is necessary to tap off a sample signal of the input power without significantly affecting the main signal path. Coupler typically has 4 ports as seen in Figure 4-19, and some parameters are defined as follows.

$$\text{Coupling factor} = 10\log\frac{P_{port3}}{P_{port1}}\ [dB] \tag{4-13}$$

$$\text{Directivity} = 10\log\frac{P_{port4}}{P_{port3}}\ [dB] \tag{4-14}$$

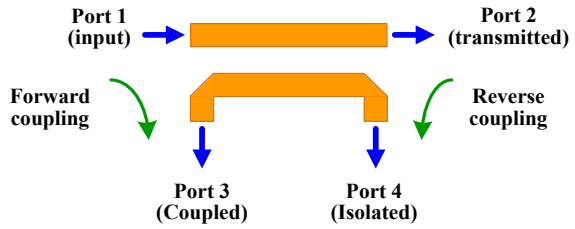

Figure 4-19. A schematic of a general bi-directional coupler

$$\text{Isolation} = 10\log\frac{P_{port4}}{P_{port1}}\ [dB] \tag{4-15}$$

The coupling factor is the ratio of the coupled output power to the input power. This is a negative number in dB, and the fundamental specification of couplers. In scattering matrix, this is S_{13}=S_{31} in the forward direction and S_{24}=S_{42} in the reverse direction. The directivity is the ratio of the power out of the coupling port to the power out of the isolation port, in dB. This is how effective the coupler has the independency between the coupled and an isolated port. Higher directivity is better performance of couplers. The isolation is the ratio of the input power to the power out of the isolation port, in dB. It indicates S_{14}=S_{41} in the forward direction and S_{23}=S_{32} in the reverse direction. In practice, it is impossible to build a perfect coupler, and some amounts of unintended power exist in all ports.

To support a power monitoring circuit, directivity is an important parameter. That is, both the coupled port and the isolated port must be separated with a proper phase shift (e.g. 90°). In fact, Directivity = Isolation – Coupling factor in dB by (4-13) ~ (4-15), and a finite isolation is the reason for limited directivity. Power detector circuits measure the reflected power by measuring the output of a bi-directional coupler at the coupled port. This output can be affected by the coupling factor, and the relative amplitude / phase difference between the reflected signal and signal present due to directivity make very complicated signals in the bi-directional coupler. Thus, it is hard to measure the pure power component from the coupler. The high accuracy of power measurement circuits cannot be obtained without a high directivity coupler.

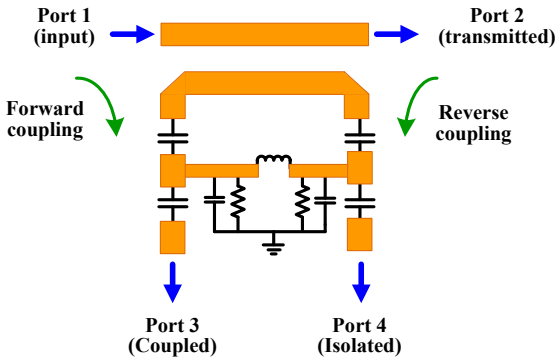

Figure 4-20. A schematic of the proposed coupler having a high directivity

In the coupler design of the automatic matching and tuning unit, there are some critical constraints: a main signal line carrying high power RF signals, a small size to fit a RF coil dimension, and a good coupled signal generation at the coupled port. Since the operating frequency is 300MHz at 7T, λ/4 wavelength for a coupler design is about 25cm. it is not allowed in designing of RF coils because of too long length and radiation issues. To meet these constraints, the fundamental concepts have been modified and a new coupler with lumped elements has been proposed and designed without affecting a main signal line but with high directivity as shown in Figure 4-20. This coupler is adapted to monitor the RF power resulting from the RF coil's impedance mismatch condition.

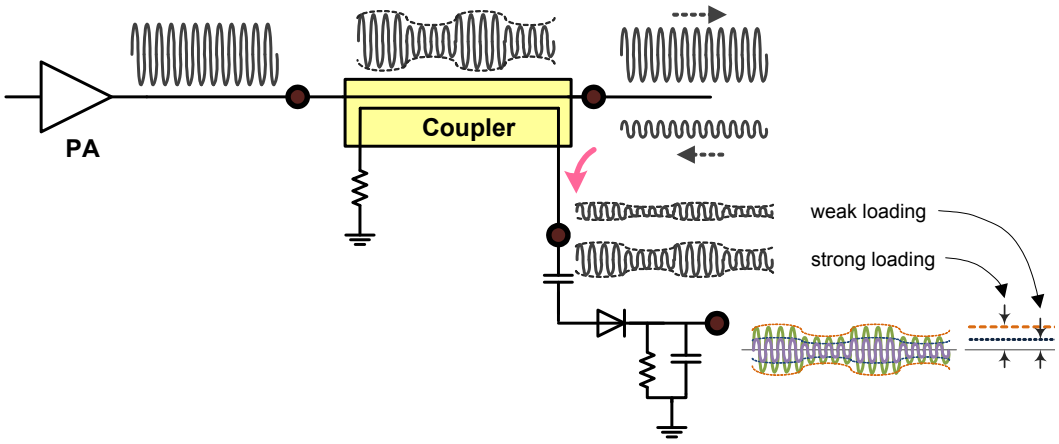

Figure 4-21. The concept of the RF power monitoring

As a result, the coupled output of this coupler is connected to the input of the aforementioned power measurement circuit and then the DC voltage output is generated according to the coupled RF power level depending on the loading condition as seen in Figure 4-21. That is, a heavy load condition makes voltage output higher.

4.7 Hardware design

The fully electric controlled stand-alone system for automatic tuning and matching of the RF coil is implemented. As shown in Figure 4-22, this system consists of the RF coupler, the RF switch and power detector, the capacitor array bank with PIN diodes, and the FPGA as well as the RF coil based on the TEM structure. In the overall operation, there are two steps: the first step is automatic tune/match procedure with the moderate power level, less than 20dBm, and the second step is the same with a normal MRI scanner operation with the high power (up to 1kW) to take MR images. In the first step, the output of RF power detector represents the reflected power level through the RF coupler for the power monitoring circuit at the input of the RF coil. From this information, the main control and decision block decides the optimum condition that is the impedance is matched to 50Ω, and the frequency is tuned to the Larmor frequency,

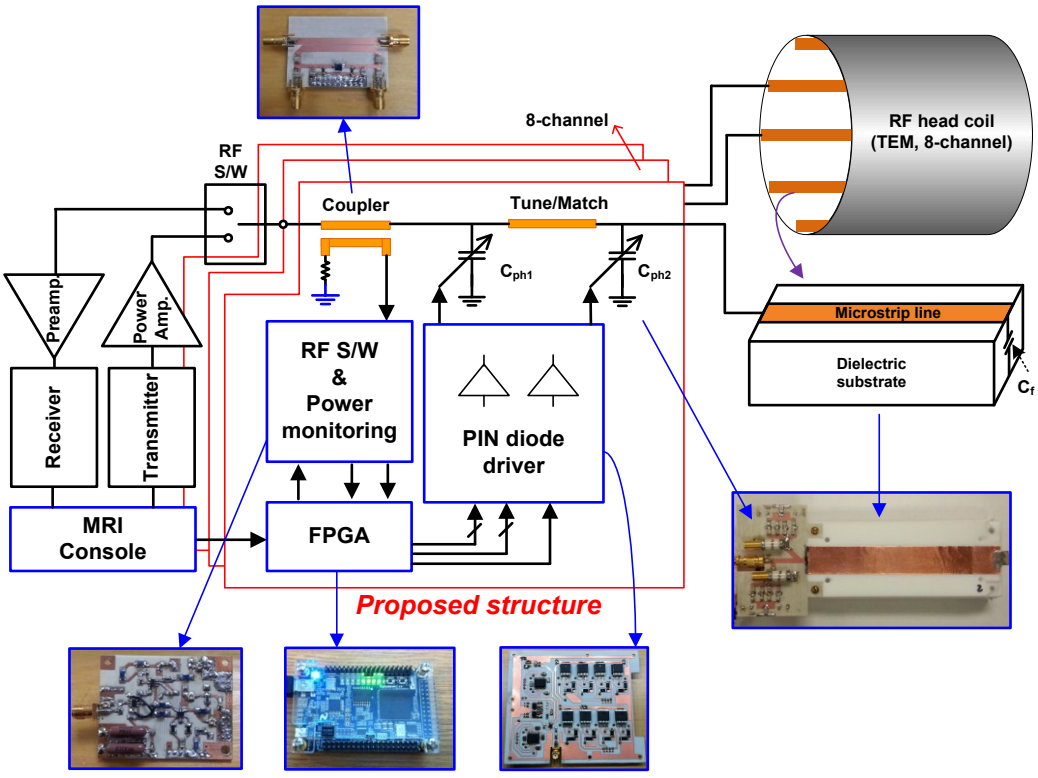

Figure 4-22. Hardware system of the automatic tuning and matching for RF coil.

regardless of the load (patient) conditions. The capacitor-arrays with PIN diodes are built with the microstrip Pi matching network, and the FPGA installed the main algorithm electrically drives PIN diodes to turn on or off through PIN diode driver circuits during searching the optimum impedance matching/tuning condition. Once the FPGA keeps the final results, the RF switch turns off all circuits except for the essential part to drive PIN diodes. The purpose of this step is to protect the circuitry operated with the low power domain. As a result, this system automatically works for the impedance matching and tuning, thus the time-consuming manual re-tuning/matching is not required.

4.7.1 Single TEM coil element with digitally controlled capacitor array

Figure 4-23 (a) shows the RF coil element based on the TEM structure. The copper tape is on the low loss Teflon (height of 1.9cm and length of 14cm), and two capacitor arrays are at the ends of the Pi matching network to satisfy the tuning of the resonance frequency and the matching of the impedance. Two main trimmer capacitors (NMAJ40HV by Voltronics) and four branches to adjust capacitances from a basis of the main trimmer capacitor values were implemented in the tuning and the matching side, respectively. Each branch consists of capacitor with the small capacitance (0.7pF ~ 3.5pF) and the PIN diode (MA4P7470F by MACOM). In test bench, the single element was initially matched to 50Ω and tuned at the Larmor frequency (f=297.2MHz) for 7T (red-colored solid line) as illustrated in Figure 4-24 (a), and re-matching and tuning were conducted well (green-colored dotted line) after a sample was loaded (blue-colored solid line) as seen in Figure 4-23 (b). Figure 4-23 (c) shows the cover range when the capacitor array is digitally contolled by PIN diode drivers. Total 8-branches (each capacitor array

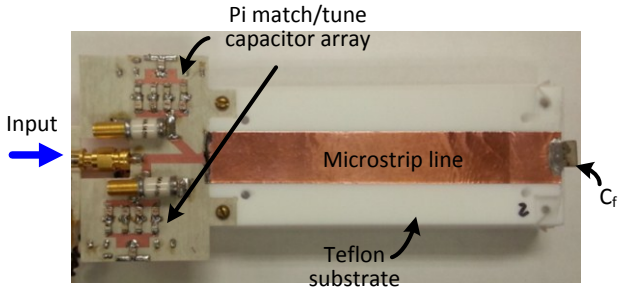

Figure 4-23. Single TEM coil element.

has 4 brances) generate 256 different states depending on capacitnaces installed branches (usually 0.7pF ~ 3.5pF in each branch). The red-colored dot presents the initial tune/match condition, and the blue-colored dot indicates the result of the loading effect by a phamtom. The combination between two main trimmer capacitances and small capacitances in branches should be preset in the test bench to cover the proper ranges.

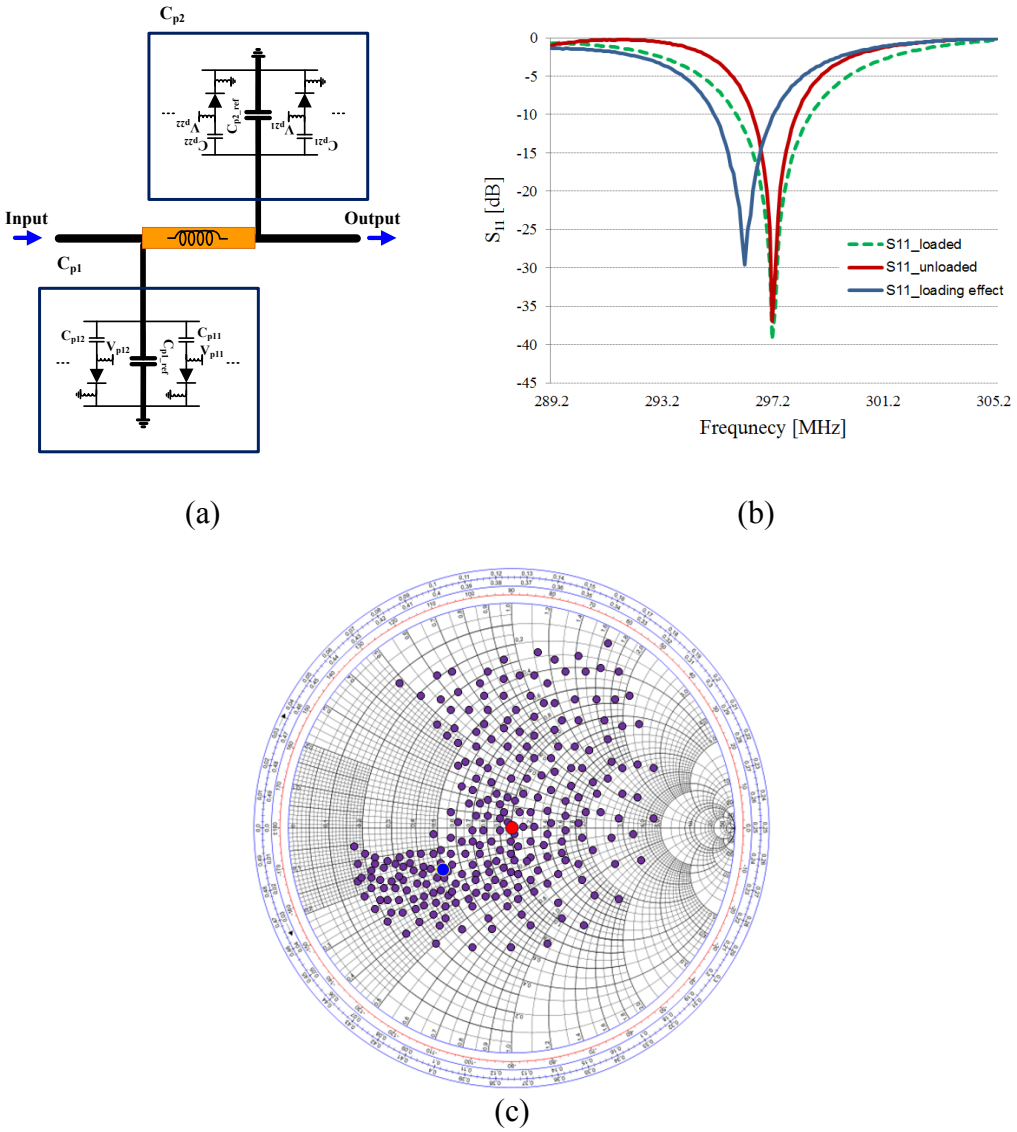

(a) (b)

(c)

Figure 4-24. (a) Pi matching with digitally controlled capacitor array, (b) measured S_{11} in test bench, and (c) digitally controlled matching cover range on the Smith chart.

4.7.2 RF coupler

A coupler provides the source information in an automatic controlled RF feedback loop like this automatic tune/match system. Figure 4-25 shows the proposed coupler design schematic using ADS (by Agilent) in (a) and the simulation results with -27dB coupling factor, -59dB isolation, and -32dB directivity in (b) around the Larmor frequency (f=297.2MHz) for 7T. Microstrip lines have 50Ω characteristic impedance and the length of coupled lines is 35mm. In Figure 4-25 (c), the manufactured coupler is shown, and the measured results of this coupler are presented in (d). Coupling factors between the simulation and measurement are conformable, but the isolation value in the measurement is limited to -47dB resulting in -20dB directivity. This directivity is not bad but it shows the limitation of small size coupler compared with the usual λ/4 length.

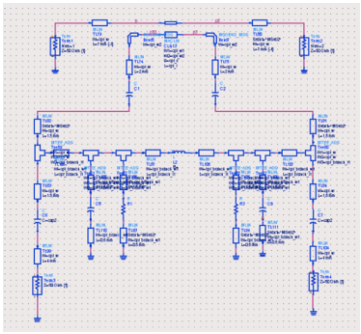

(a)

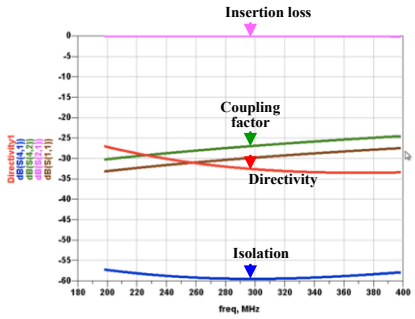

(b)

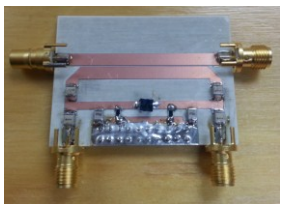

(c)

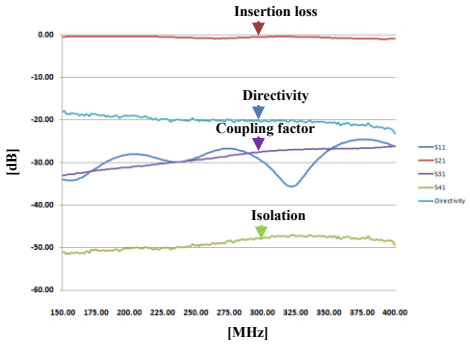

(d)

Figure 4-25. High directivity coupler design and results: (a) coupler schematic by ADS (b) simulation results (c) manufactured coupler and (d) measured results

4.7.3 PIN diode driver and level conversion circuit

To effectively drive PIN diodes, a level converter to generate dual high voltages and current driving amplifier are required. As shown in Figure 4-26 (a), TTL level control signals from FPGA are split into positive and negative voltages in the level converter, and its signals are amplified in the PIN driver amplifier. MAX234 (by Maxim) with 5V single power and ±7V~±9V dual output voltages has been chosen for the level converter, and OPA552 (by Texas Instruments) with high voltage (±30) and high current (200mA) capability was used for the PIN diode driver. Figure 4-26 shows the board of 8-branches PIN diode drivers with the level converting interface circuits. Since such board is for single channel of the multi-channel, total 8 boards are required for 8-channel volume RF head coil. As a results, TTL outputs from FPGA were first converted to ±7V ~ ±9V dual

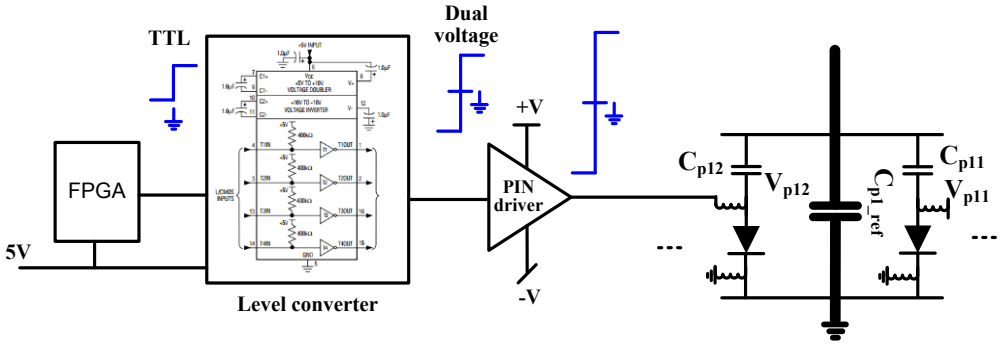

(a)

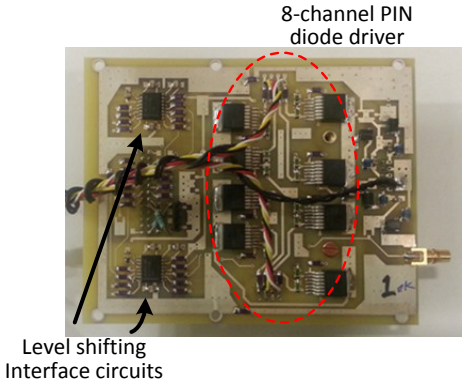

(b)

Figure 4-26. (a) PIN diode driving path from FPGA to PIN driver through level converter and (b) the board of 8-branches PIN diode drivers with level converter circuits.

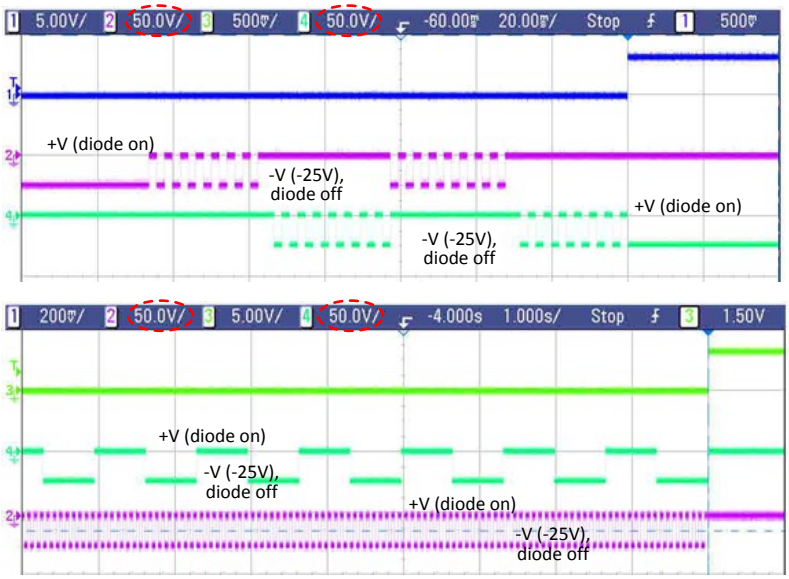

Figure 4-27. The measured outputs of the PIN diode drivers.

output voltages with a single 5V power supply and then amplified to about ±25V with high current (up to 200mA) capability to turn on or off PIN diodes. In case of the forward bias, each PIN diode needs at least 20mA to be turned on. In case of the reverse bias condition to turn off the PIN diode, the reverse voltage should keep the proper voltage level to prevent the RF leakages through PIN diode. It depends on current driving capability of the PIN diode driver. The driver amplifier (OPA552) can drive currents up to 200mA resulting in providing enough current amount to keep the negative voltage during the reverse bias condition. Figure 4-27 shows the experimentally measured data from the board of the PIN diode drivers with the test bench condition (about 45dBm RF source) discussed the following section of 4.8. When the PIN diodes are turned on, the forward bias voltages are applied with about 0.7V ~ 1V. It makes sure that the PIN diodes are turned on properly. When the PIN diodes are turned off, the reverse bias voltages are applied with about -25V. It also makes sure that the PIN diodes maintain the reverse condition to turn them off constantly.

4.7.4 RF power detection circuit

A board of the RF power detection circuit is shown in Figure 4-28 (a), and its measured output voltage is also shown in (b) according to the input RF power of dBm unit. This result is comparable to the specification of the power detector (LTC5507 by Linear technology). A RF switch is placed in the input of this circuit board to switch the RF signal path. This RF switch (HMC545 by Hittite microwave corporation) allows the input RF power with up to 34dBm, 5V operation, and its switching time is in the nano-second scale. Thus, it can be used for this project. The coupled RF signals flow into the RF detector IC during the automatic tuning and matching function. After this function, the RF switch changes the RF signal path to the ground through 50Ω resistor made by two high power 100Ω resistors in parallel. This RF signal switching prevents the damage of circuits operated in the low power domain.

This circuit board generate the important data to be used in the main control and decision block, but it is very weak and sensitive to the RF interference, e.g. the radiation effect by the RF coil.

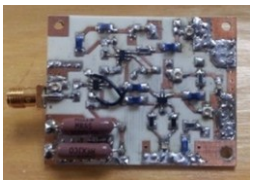

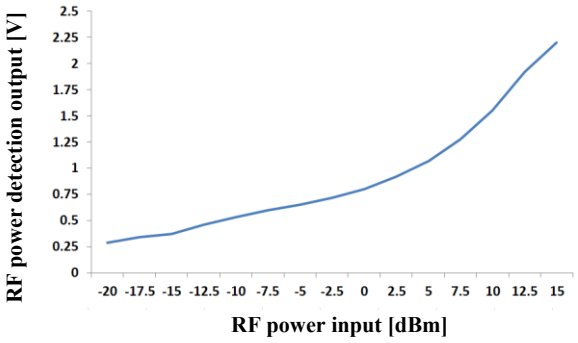

(a) (b)

Figure 4-28. (a) A circuit board containing RF power detector, RF switch, and driving circuits. (b) the measured output of the RF power detection circuit

4.7.5 Main control unit

The main automatic tuning and matching algorithm was implemented with the FPGA core (Cyclone 4 series by Altera) using Verilog HDL (Hardware Description Language). As illustrated in Figure 4-29, the 12 bit ADC (National Semiconductor) converts the sampled RF reflection power (alternating analog signals) into 12bit digital bits in front of the FPGA. The main clock of 50MHz is supplied by the external oscillator on the board. In the Auto T/M core block, the PIN diode switching control signals are generated, and then its corresponding RF power signals are sampled with the multiple sampling as following time diagram in Figure 4-30. The interval between RF pulse packets is 2ms, and multi-sampler samples the reflected power level generated by the RF power measurement circuit after PIN diode switching. The PIN diodes are switched just after the RF pulse pocket to eliminate the influence of RF signals with high power. The main algorithm for automatic matching and tuning basically follows the aforementioned concept in Figure 4-6. Since there is some design issues featured in the following section, this concept can be modified to insure the reliable results. There are 4 branches of the PIN diodes and capacitors for the tuning or matching capacitor array. Therefore, total 256 states can be generated for one iteration. Figure 4-31 (a) and (b) shows the simulation

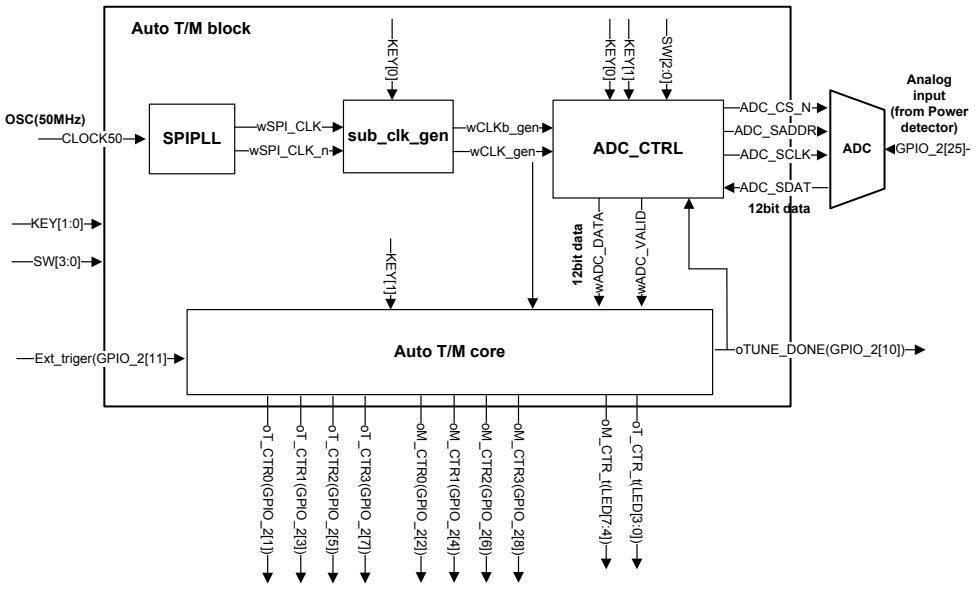

Figure 4-29. System diagram for the FPGA design.

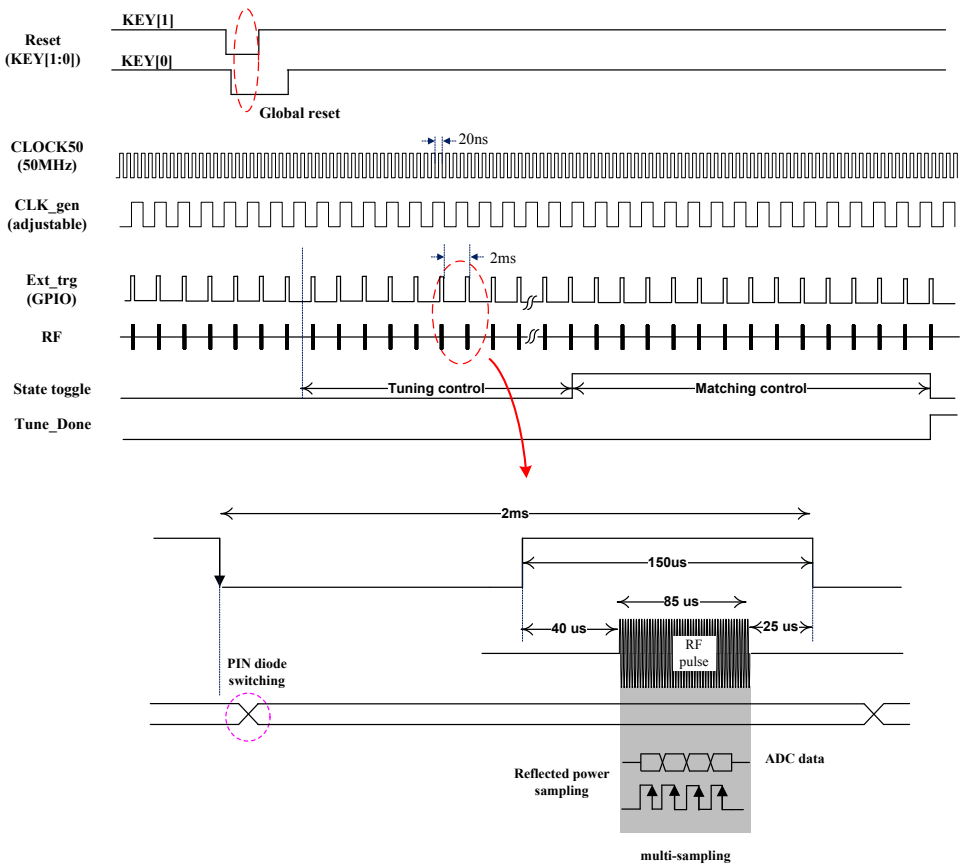

Figure 4-30. Time diagram of the entire system and data sampling.

results by ModelSim and the experimentally measured results by Oscilloscope, respectively. The experimental results show that this systems follows the simulation results well, and all PIN didoes in the capacitor arrays are turned on or off without distortion or broken signals. Since these experiments are performed with the following test bench condition, all functions of the FPGA and drivers work correctly under the practical condition of MRI systems. Both results are also comparable with the desired timing diagram in Figure 4-30.

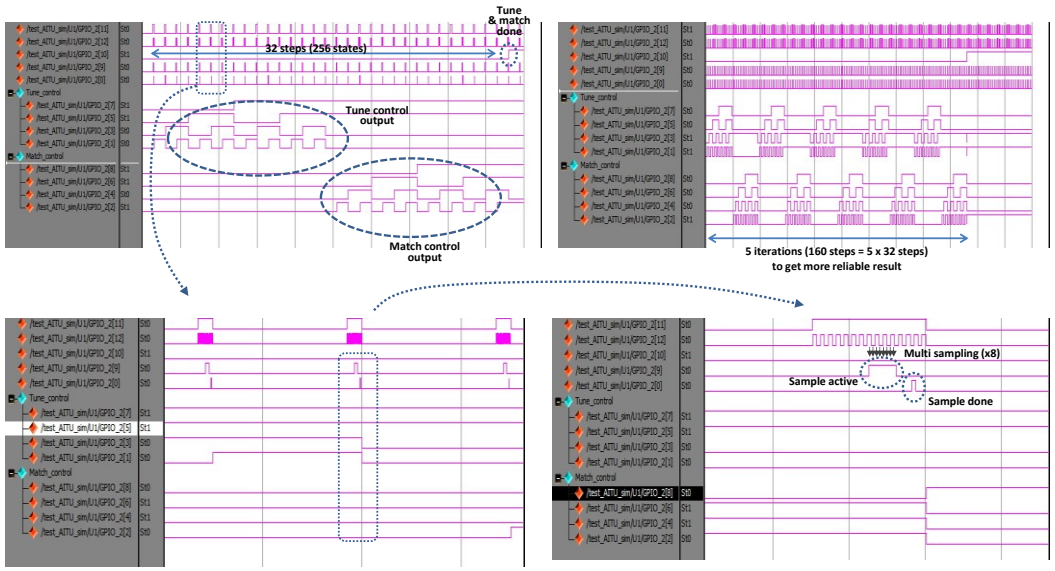

(a)

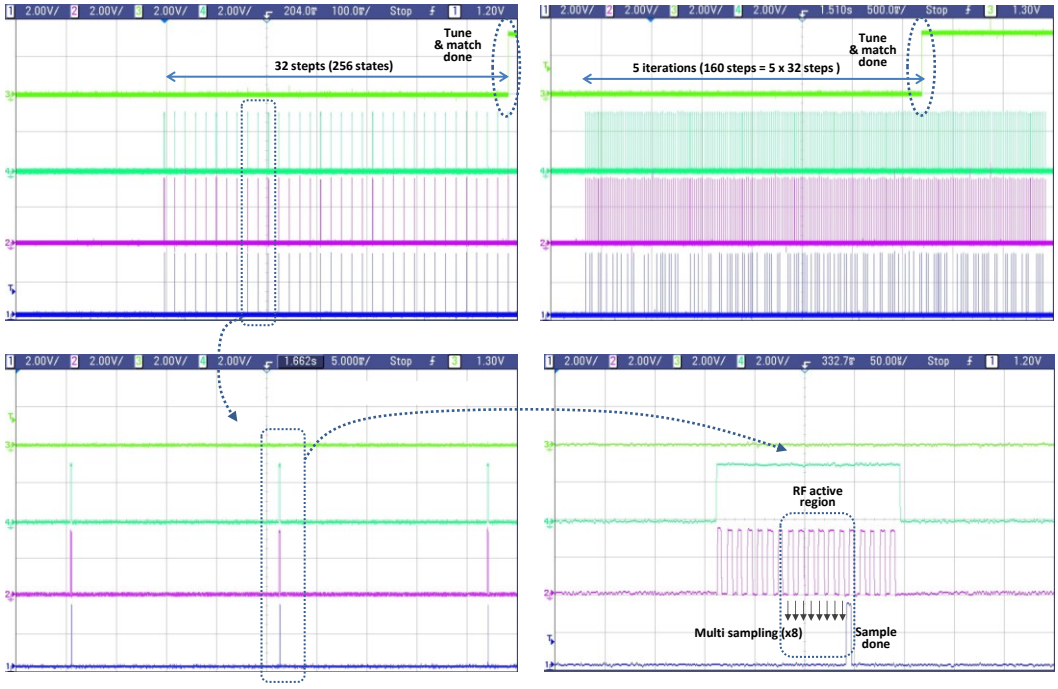

(b)

Figure 4-31. (a) FPGA simulation (by ModelSim) and (b) Measured results (by oscilloscope)

4.8 Test bench condition and experimental results

Before applying the practical MRI system, the test bench is necessary to verify the system's performance with high power range (~kW) and the expected radiation influence by the resonator of the RF coil. MRI system is a high price equipment and thus limits the user's operation range. Therefore, the same condition except for a strong magnetic surroundings is required in the test bench when a new device to be installed an existing MRI system is developed. The use of un-blank signal (TTL level gating signal to active or inactive RF pulse) is only way to communicated with a MRI console, and this signal required building a stand-along automatic running device synchronized with a main MRI control line. Figure 4-32 (a) show the measured RF un-blank signal and RF signal from Siemens MAGNETOM 7T machine, and Figure 4-32 (b) is the reproduced un-blank signal and RF signal using the inLAB power amplifier unit as shown in Figure 4-33. From this test bench setup, the same condition which includes an electrical connectivity of MRI system has been prepared. In the inLAB test bench, the interval between packets of RF pulses is 2ms to build the low duty ratio, and RF signals have up to about 45dBm.

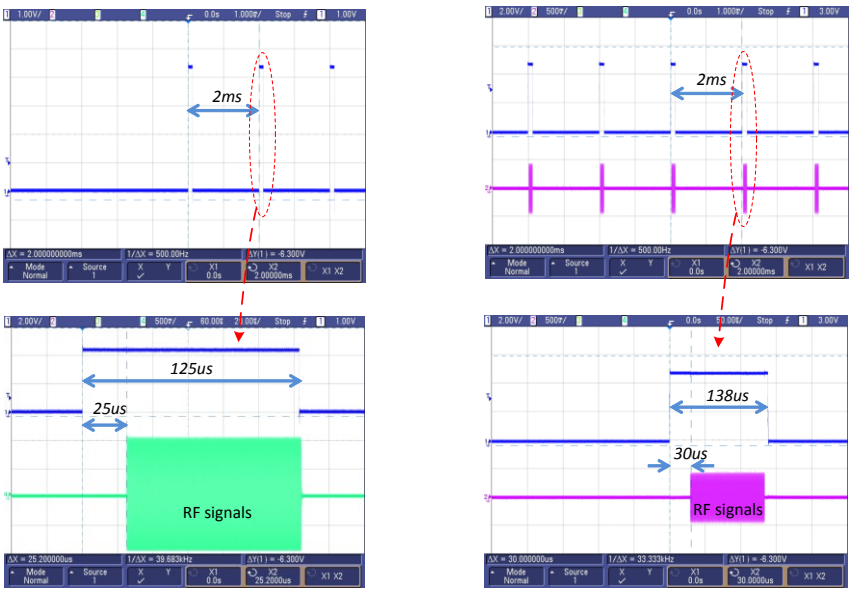

(a) (b)

Figure 4-32. Un-blank signal and RF pule: (a) at Siemens MAGNETOM 7T and (b) at the test bench

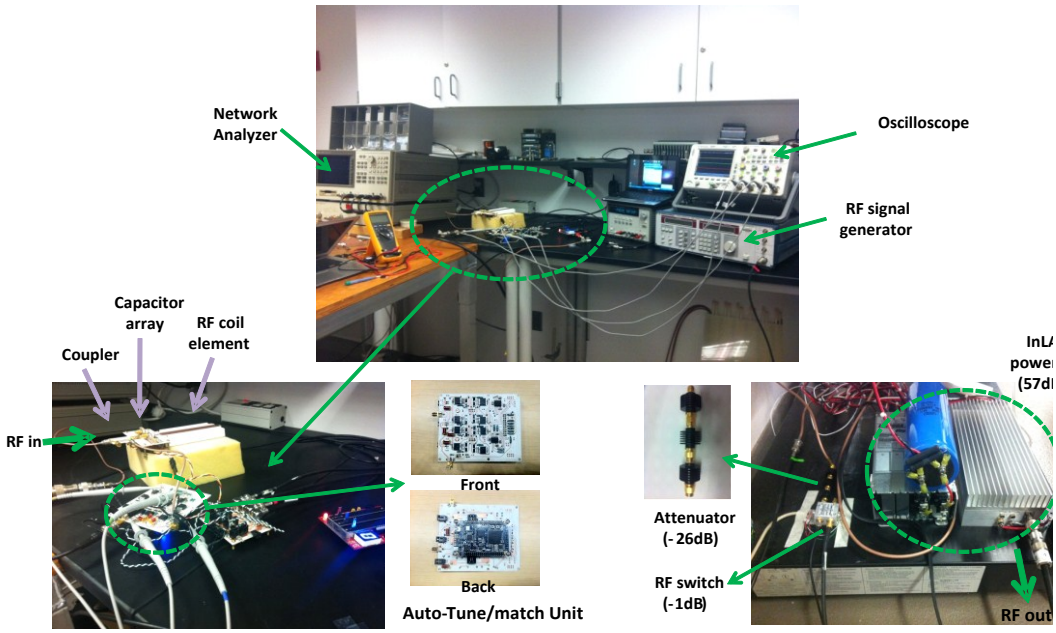

Figure 4-33. Test bench setup

The RF signal generator which can generate RF signals up to 19dBm is connected to power amplifier which amplifies the input signal with the gain of 57dBm. The attenuator of -26dBm is placed between them. The connectors and cables has about -5dB loss. In the first step, the practical RF power entering the RF coil element is about 0 ~ 20dBm (≈ $6V_{pp}$) to find the best impedance and frequency tuning condition with the automatic tune/match unit, and then the systems is tested with the RF signal with high power (around 40dBm ~ 45dBm).

Figure 4-34 shows the successfully measured automatic tuning and matching results with the inLAB test bench. The 42dBm RF source is utilized, and the coupler with 27dB coupling factor offers the sampled RF signal. The top windows show the reflected power monitoring signals from the initial tune/match condition to the automatic tune/match function after phantom loading. In the middle of this test, the phantom is loaded, and the varying output of the power detecting circuit is shown in the center of Figure 4-34. The left window of the bottom is the PIN diode control signals, and the right window is the

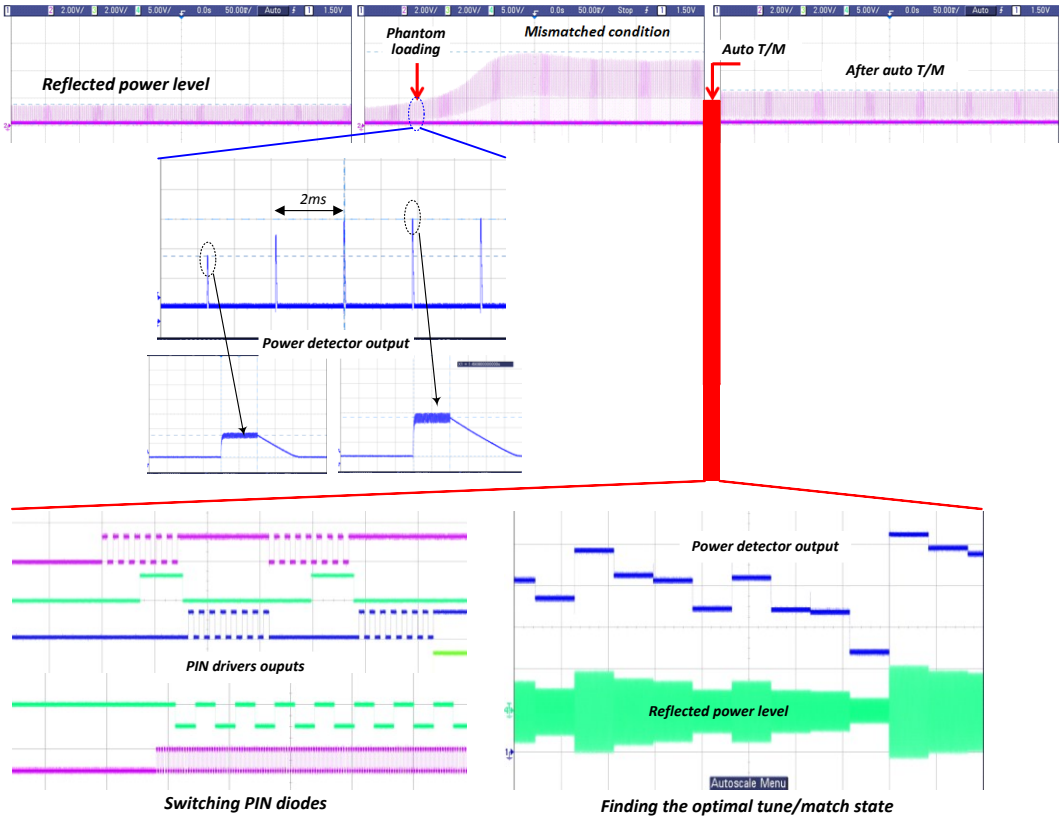

Figure 4-34. Test bench results of fully automatic tuning and matching.

zoomed reflected power and its power detector's DC output, simultaneously. As a result, the function of automatic tuning and matching for the RF coil has been successfully fulfilled.

4.9 Single channel verification

Figure 4-35 shows the automatic tuning and matching results of single element from experimental setup of 7T MRI scanner (f=297.2MHz, Siemens Magnetom 7T) with a cylindrical phantom filled 8 liter sucrose/saline (ε_r=58.1 and σ=0.539 S/m). A portable network analyzer was utilized to check the impedance matching inside the RF shielded room. This experimental results confirm that the proposed system returns the reflection coefficient (S_{11}) to the initial tuned/matched condition to avoid the loading (body) effect after running the automatic tune and match function. Figure 4-36 (a) shows the improvement of the RF penetration in MR images by the impedance matching and tuning. By the preliminary results using this single channel element installed the automatic tune/match unit, SNR is enhanced about 20% (combined transmitting and receiving parts) in the top side and 24% in the bottom side, respectively, as shown in Figure 4-36 (b") and (c"), and the penetration depth is also increased in B_1^+ map(μT/sqrtW) of Figure 4-36 (c') to (c"). For the fully automatic stand-alone system operation, the RF un-blank signal from the MR console is used to trigger off the automatic tune/match function. The total running time is less than one second to get the successful impedance tuning/matching condition.

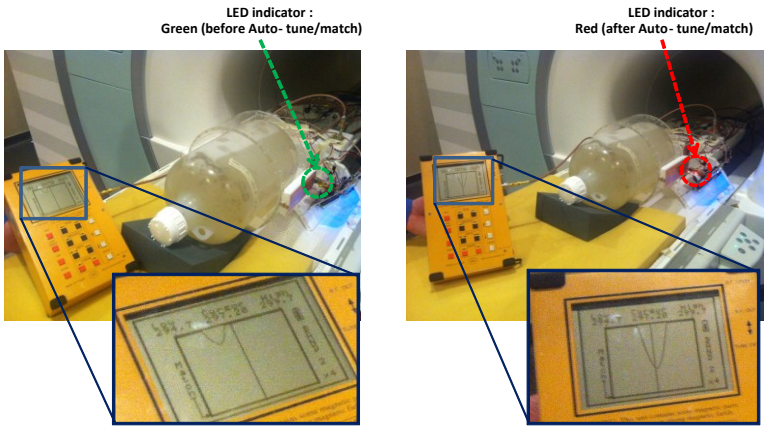

Figure 4-35. Experimental set-up with single RF coil element in 7T and the results: (a) before auto-tune/match (b) and after auto-tune/match.

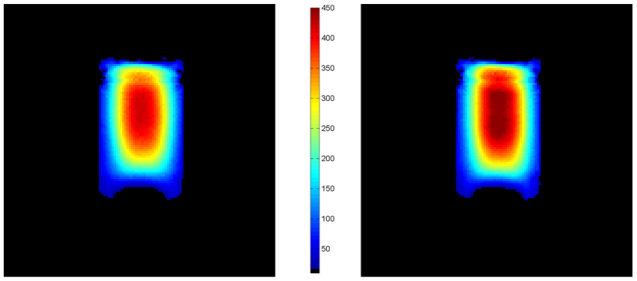

(a’) (a’’)

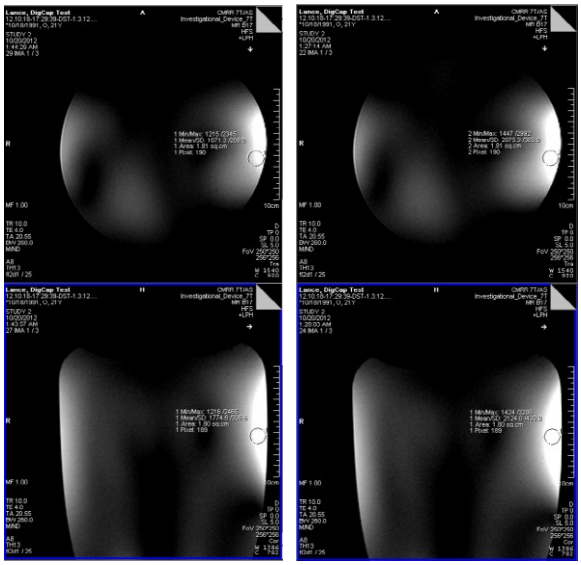

(b’) (b’’)

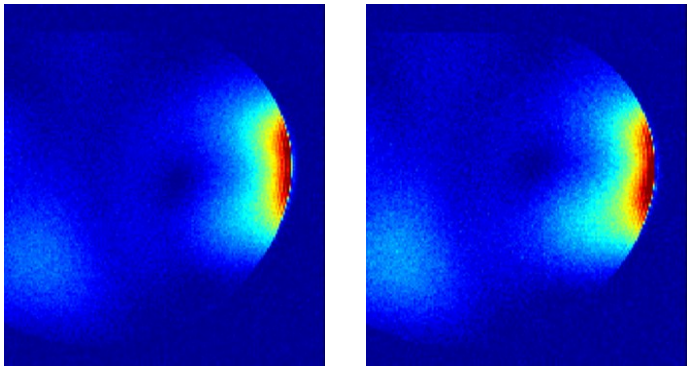

(c’) (c’’)

Figure 4-36. Experimental MR image results of the slices in the central region of with a cylindrical phantom; (a’), (b’), and (c’) are before auto-tune/match and (a”), (b”), and (c”) are after auto-tune/match.

4.10 8-channel RF head coil at 7T

The 8-channel RF head coil with the automatic tuning and matching function is presented in Figure 4-37. It consists of four parts: the RF coil based on the TEM structure, the electrically controlled capacitor arrays with the PIN diodes, the power monitoring circuit and the main control board containing the PIN diode drivers. First, the RF coil part has been built with the copper tape on the low loss Teflon (height of 1.9cm and length of 14cm) and, eight elements attached to a cylindrical shell with 25.4cm in diameter. Second, capacitor arrays have two main trimmer capacitors (NMAJ40HV by Voltronics) and microstrip Pi matching network. Four branches to adjust capacitances from a basis of the main capacitor values were implemented at the tuning and matching side, respectively. Each branch consists of one capacitor with small capacitance and one PIN diode (MA4P7470F by MACOM). The combination of capacitances controlled by PIN diodes switching usually covers the range of 1~7pF to correct the loading (body) effect by the

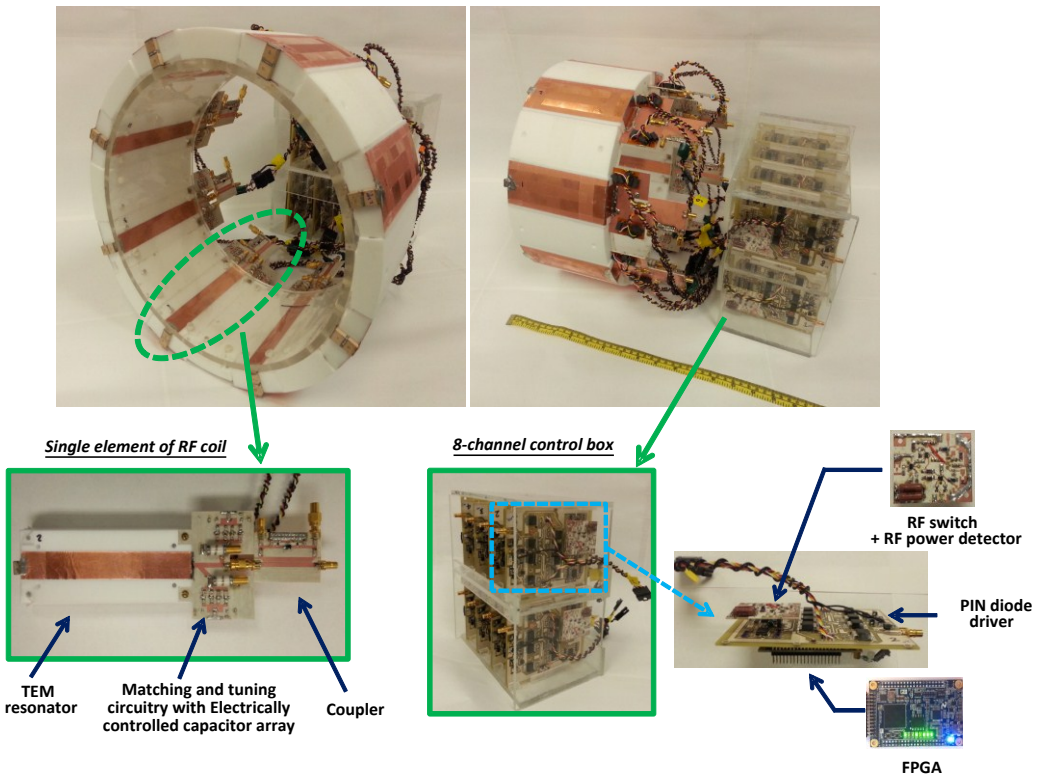

Figure 4-37. 8-channel RF head coil with automatic tuning and matching units.

results of the aforementioned test bench experiments. Each element combined the RF coil and the capacitor arrays was initially tuned to 297.2MHz for 7T and matched to the power amplifier with 50Ω through coaxial cable. Third, RF couplers, RF switch, and the power detection circuit are the components for the power monitoring circuit. The properties of the RF coupler have the coupling factor of -27dB, the isolation of -45dB, and the directivity of 18dB. High directivity of RF coupler is necessary to get the reflected power by loading variations. RF power detector (LTC5507 by Linear) based on the Schottky diode's peak detector and buffer was used to measure the RF power of the head coil, and RF switch changes the direction of the coupled RF power signal path to the ground after the auto-tune/match function to protect circuits operated by the low power domain during high power operation. Fourth, the main control block consists of the PIN diode drivers, the level shifting interface circuits and the FPGA (Field Programmable Gate Array). The automatic tune/match algorithm has been run in the FPGA using the real-time output of the power monitoring circuit and then it switches the PIN diodes by the output of the PIN diode drivers. The interface circuits were to generate positive and negative voltage from TTL or CMOS level of FPGA to support PIN diode drivers. For fully automatic stand-alone system operation, the RF un-blank signal from the MR console is used to trigger off the automatic tune/match function.

In the test-bench, the RF function generator, the network analyzer and the cylindrical 8L bottle filled with sucrose/saline solution (ε_r = 58.1and σ = 0.539 S/m) were used to measure the experimental scattering parameters as shown in Figure 4-38. The scattering parameters of each channel were measured in three states: the initial tuned condition (no the bottle present), after the phantom is loaded and after the auto-tune/match function corrected the change by the phantom loading. Table 4-2 shows the RF coil characteristics and performances of each channel. Experimental results demonstrate about 1% power loss (-20dB in S_{11}) or less and the improvement about 4~21% in the power delivered to the RF coil after the automatic tuning and matching correcting the loading (body) effect.

The MR image performance was evaluated using the Gradient Recalled Echo (GRE) pulse sequence (resolution= 1×1mm, repetition time=150ms, echo time=6 ms, slice thickness = 5mm) to acquire the slices in Figure 4-39 and Figure 4-40. Figure 4-39 shows

the experimental set-up of 7T MRI scanner (f=297.2MHz, Siemens Magnetom 7T) and the performance of each channel.

Figure 4-40 shows MR images with the resolution phantom after automatically tuned and matched function. This function needs less than 550ms per channel and is synchronized with MRI console which provides the control signal of RF pulses.

Finally, These results are beyond comparison with the manual tuning and matching adjustments that consumes a few minutes per channel.

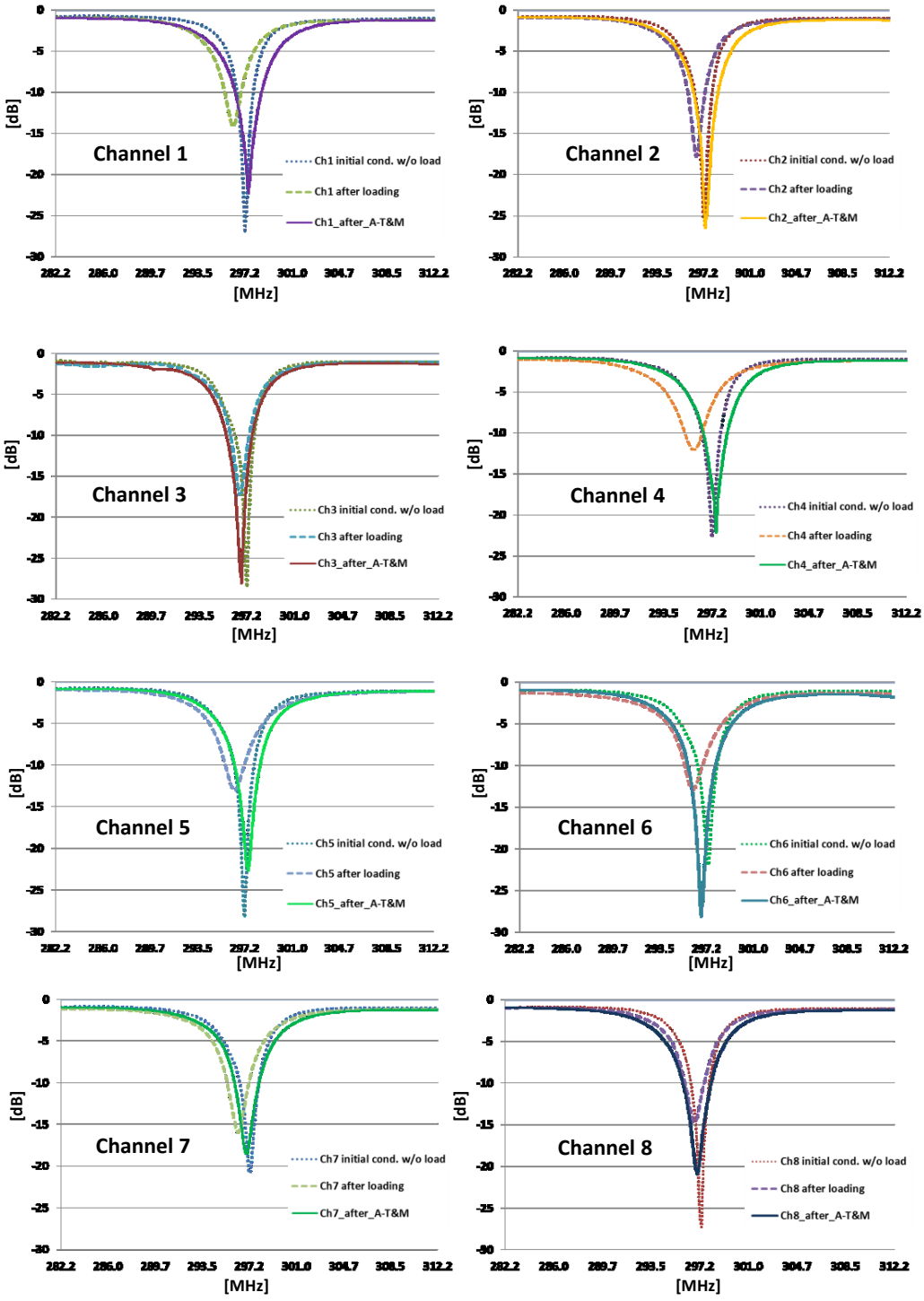

Figure 4-38. Experimental S-parameters (reflection coefficients): the initial tuned conditions without a phantom, after a phantom loading, and after the automatic tune and match at each channel.

Table 4-2. RF coil element characteristics and performances.

Channel	Initial Cond. w/o load	After loading	Loading effect		After Auto-T&M	Improvement by A-T&M	
	S11 [dB]	S11 [dB]	Δ S11 [dB]	Power loss	S11 [dB]	Δ S11 [dB]	Power
1	-27.0	-7.9	19.1	16%	-19.3	11.4	15%
2	-25.3	-11.1	14.2	8%	-22.3	11.2	8%
3	-28.4	-11.6	16.8	7%	-25.6	14.0	7%
4	-22.7	-6.4	16.3	23%	-18.2	11.8	21%
5	-28.2	-9.9	18.3	10%	-19.3	9.4	9%
6	-21.1	-8.4	12.7	14%	-23.7	15.3	14%
7	-20.7	-9.8	10.8	10%	-17.2	7.3	8%
8	-25.7	-12.7	13.0	5%	-19.6	6.9	4%

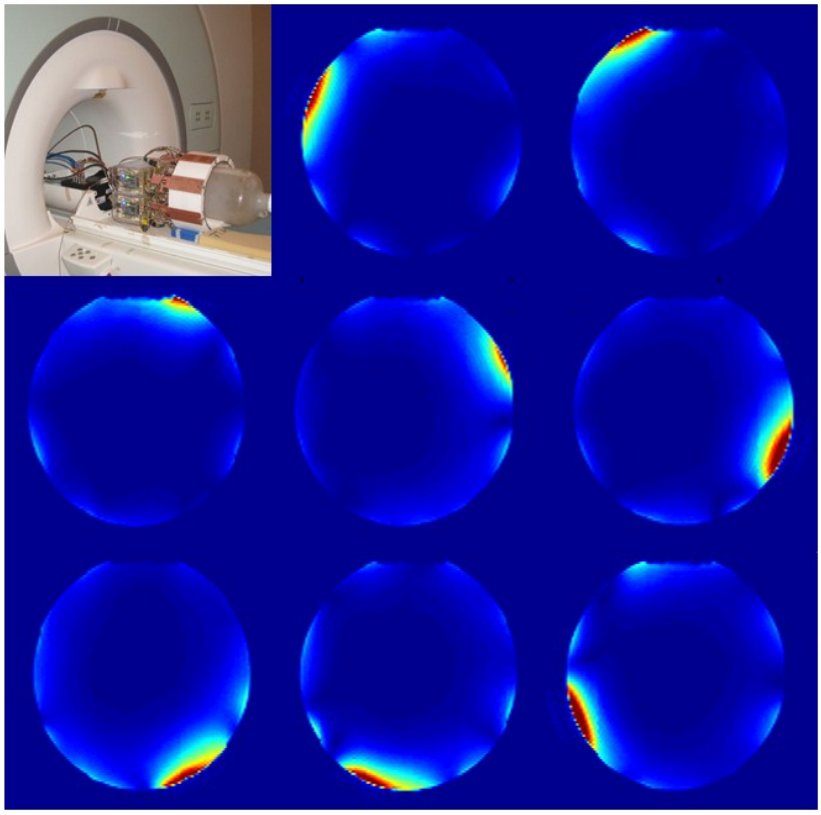

Figure 4-39. MR experimental set-up and low flip angle gradient recalled echo images of each channel of the automatically tuned and matched 8-channel RF coil.

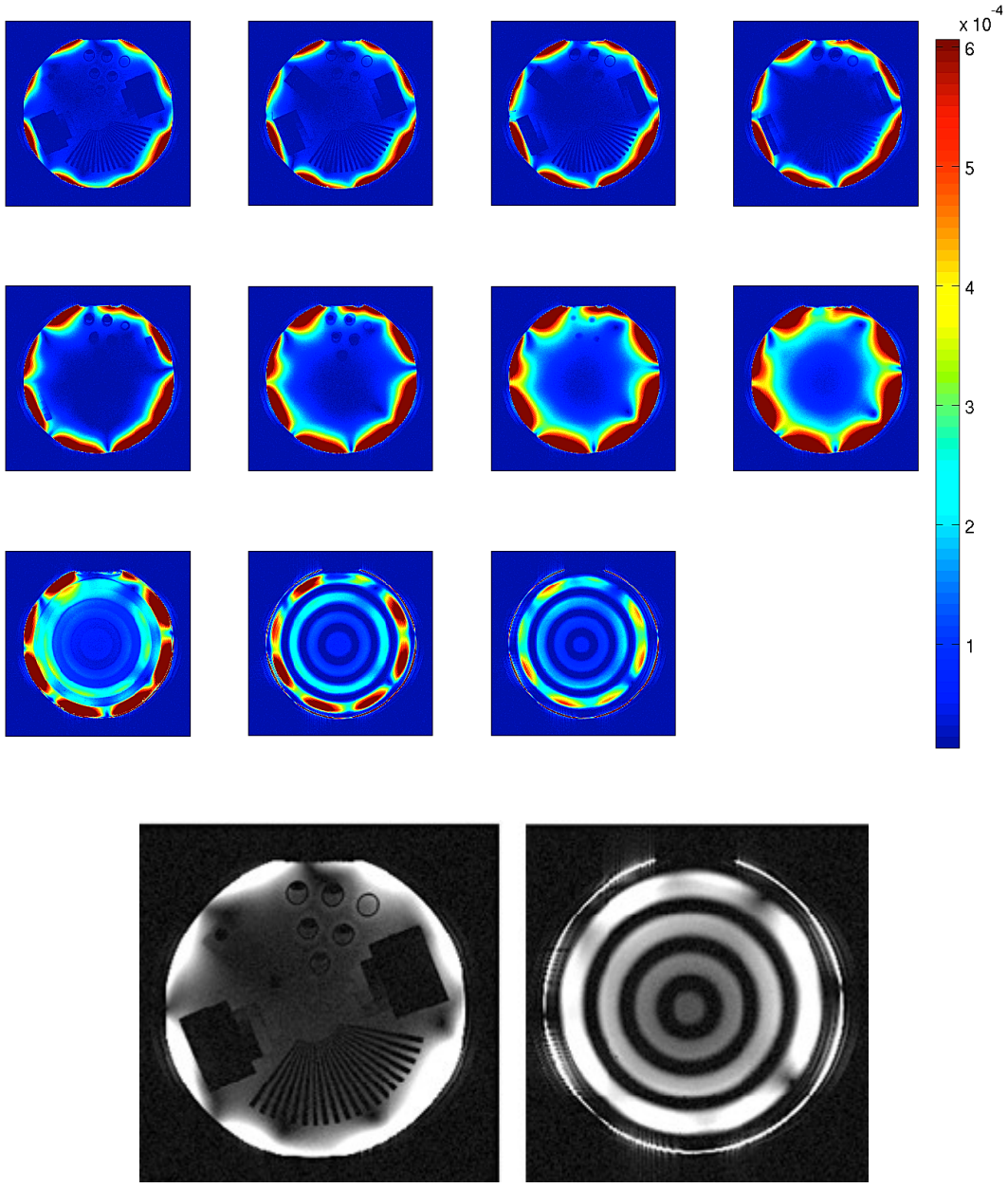

Figure 4-40. MR images of a water filled acrylic resolution phantom in the auto-tuned/matched 8-channel coil acquired with a low flip angle gradient recalled echo pulse sequence and the selected MR images (in the bottom)

4.11 Design issues of RF/electronic circuits in the RF coil

This section discusses the design issues / challenges which occur when RF/electronic circuits are applied in the RF coil design and their effects in MR images. A significantly important point is the coexistence of both the very high RF signal power domain and the low level power domain of the normal electronic circuits to drive the electronic devices in the automatic tuning and matching unit to support the RF coils. For example, the RF source with up to 1kW ($\approx 316V_{peak}$) is company with two different low power domains: a 5V for operating some RF/electronic circuits (such as RF power switch, power detector, level shifting interface circuits, driving circuits of the control signals, and FPGA) and ±20V ~ ±30V for operating PIN diode drivers in the project of this dissertation as illustrated in Figure 4-41. One of the most difficult considerations regarding a RF power configuration emerges. This concept is called 'RF grounding' or 'ground loop'. When ground loops are created, the current flow in the ground of circuits is very unpredictable, and it makes the RF grounding problem [67,68]. Since the RF coil system is a resonating

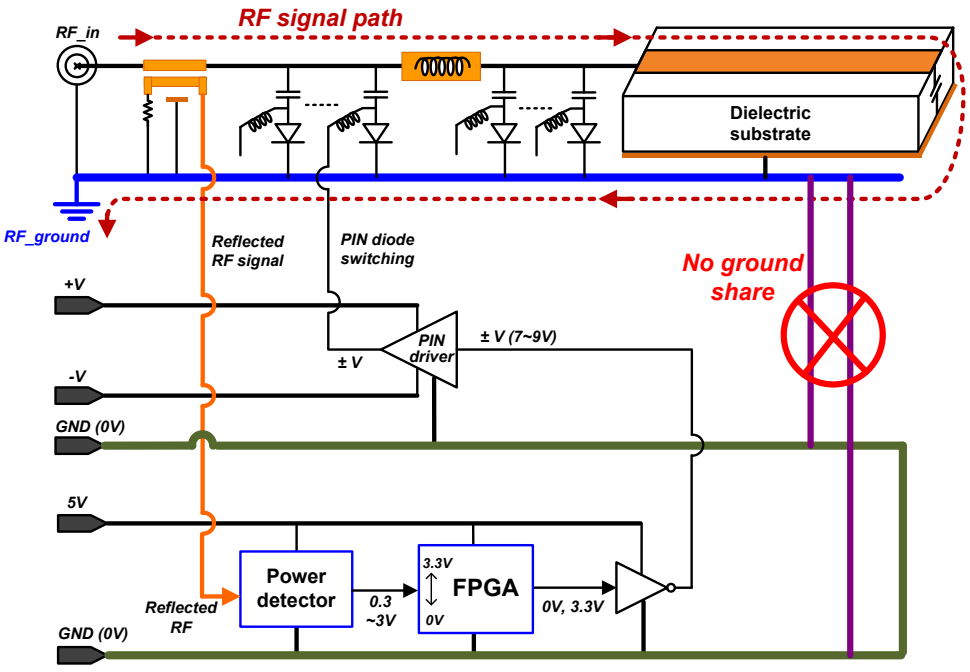

Figure 4-41. An example of the effects by the electronic devices: (a) the condition of FPGA is turned on and (b) turned off.

circuit and the high power current flows into the ground plane directly, the formation and isolation of the ground loops is very important. Consequently, the RF signals entering the RF coil must go back to the RF ground. As shown in Figure 4-41, all ground sharing points should be eliminated. If any one is present, it brings up critical problems. Figure 4-42 shows some examples occurred in this study (RF source power of 42dBm); (a') presents the corrupted output signals of the power monitoring circuit. These signals cannot offer the proper DC level of the reflected RF power. (a") shows the decent outputs which keep the constant DC level during the multi-sampling time of the reflected RF power after all RF ground loops are removed. (b') and (b") are also the corrupted signals of the FPGA due to high RF power. (b') and (b") came under 17dBm and 42dBm of the RF input sources, respectively.

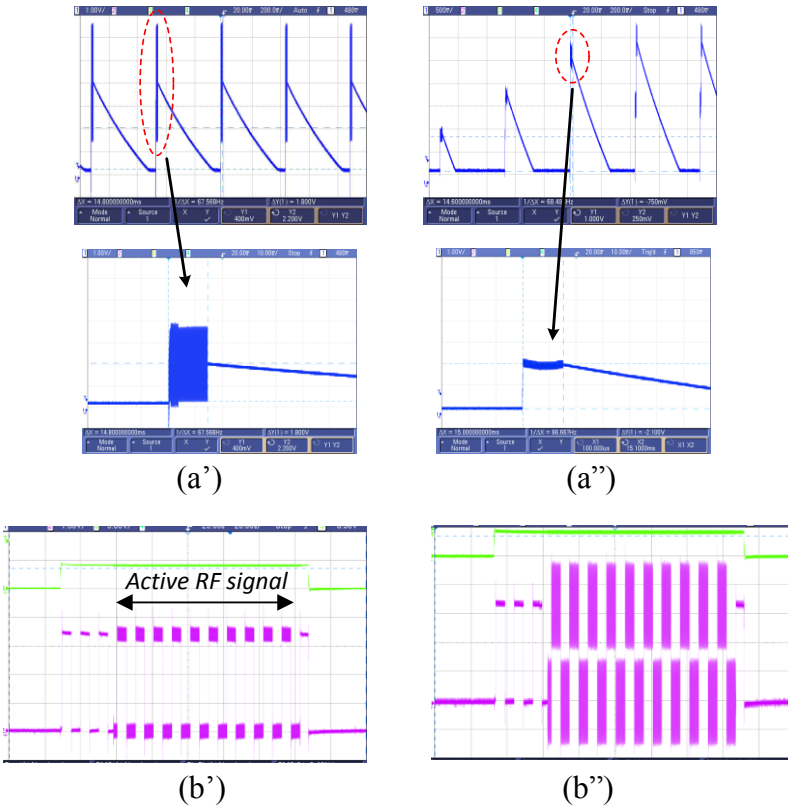

Figure 4-42. Some examples of the RF grounding problems: (a'), (b'), and (b"); the corrupted outputs. (a"); the decent outputs

Another issue is the radiation effect by the RF coil. If the RF radiation of the RF coil is large enough to affect the electronic circuits, it causes the similar results to the RF grounding problem. Thus, the output signals of the electronic circuits may include the component of the RF signal. One experiment is performed to check this effect. Around 40dBm RF signals drive the RF coil, and Oscilloscope checks the output of the RF power measurement circuit without any connection between the RF coil and the RF power measurement circuit. This set-up implies that only the radiation of the RF coil makes the output of this experimental set-up. Table 4-3 shows the measured output versus the distance between the RF coil and the RF power measuring circuit. In comparison with the result of Figure 4-28 (b), the distance in order to avoid the radiation effect of the RF coil needs at least 20cm.

Table 4-3. The experimentally measured radiation effects of the RF coil.

Distance	V_{out} [mV]
Just beside	396
5 cm	337
10 cm	312
15 cm	297
20 cm	274
25 cm	262

The last issue discussed in this section is the RF interference in MR images. When the FPGA is active with an empty coil, it makes a noise pattern compared to the result of an inactive FPGA condition in the frequency domain as shown in Figure 4-43. Since other conditions are identical, it makes sure that the FPGA operation affects the MR images . Although some electronic devices cause the noise pattern of RF interferences, it is difficult to analyze the reason and find alternative products.

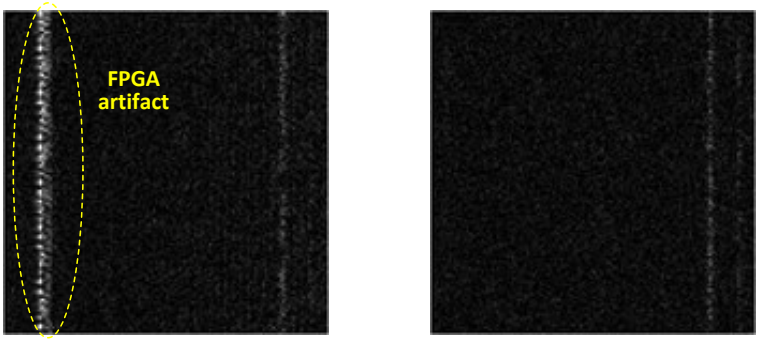

(a) (b)

Figure 4-43. RF interference in MR images: (a) FPGA active and (b) FPGA inactive

Chapter 5. **RF coil design with the improved B_1 field uniformity**

5.1 Overview

MR images from higher field systems show an improved spatial resolution and a higher SNR, but because of the higher frequency of excitation (approximately 300 MHz for 7T, 400 MHz for 9.4T, and 470 MHz for 11T, respectively), the coil design has moved from the standard birdcage coils to the microstrip transmission line design, the TEM coil. Multi-channel transceiver coils have become a popular means for the signal transmission and reception in these high magnetic fields. The multi-channel volume coil comprises of an array of the transmission line elements that are mutually decoupled and operated as independent coil elements. An object of the RF coils is to generate magnetic fields in the sample. Due to the polarity established by the static magnetic field and the properties of quantum mechanical "spin" in MRI, the alternating magnetic field produced by the RF coil is further divided into two oppositely rotating sub-components dubbed B_1^+ for the magnetic transmission field and B_1^- for the magnetic reception field.

With the higher frequencies, generating homogeneous magnetic fields is hampered by the decreased RF penetration in the human body, and RF interference patterns due to the wavelengths become significantly shorter than the anatomic dimension at these field strength in a tissue containing plenty of water. The higher frequency results in increasing tissue conductivity and decreasing permittivity. It drives the complexity of the interactions between the B_1 field distribution and the human body, causing the B1 field non-uniformity to the transmission as well as the reception. Basically, the main reason of developing a birdcage coil as volume coil is the homogeneous B_1 field distribution at low frequencies. The TEM coil also is designed to produce the homogeneous B_1 field at high frequency as well as low frequency.

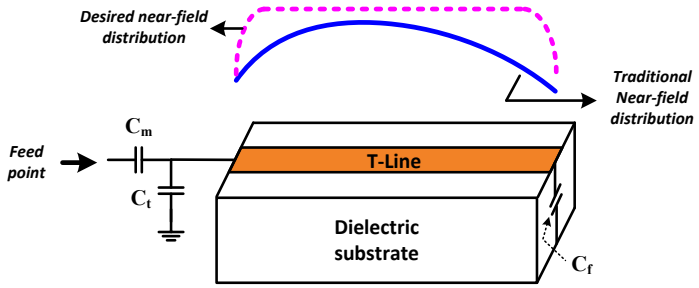

Figure 5-1. The RF transmission line coil element and its natural B1 field profile (solid line) and desired field distribution (dotted-line).

Continuously, various techniques have been used to mitigate this inhomogeneity, and the techniques used so far are termed "RF or $B_1^{\pm}$ shimming." Manipulating the amplitude and phase control of RF pulse results in improving homogeneity MR image, but it needs a complex system configuration and the change of existing MR hardware system. First of all, since the strength of different fields increases the complexity to analyze the phase difference, the magnetic field generation by RF coils should be homogenous priory, and then the propagation delay with different phase degrees can be considered.

In respect of the TEM coil manipulation, several methods based on alternating impedance, repeating thick and thin conductor sections, are under investigation to reduce these inhomogeneity, but particular patterns are generated in the near-fields by repeating sections.

To avoid non-uniform RF magnetic fields, the RF 8-channel head coil with the modified double trapezoid-like conductor shape based on TEM coil is proposed and investigated in a 7T MRI scanner. The simulation and experimental results from comparing traditional and proposed 8-channel head volume coil demonstrate the proposed head TEM coil has improved its strength and flattened the profile of near-field B_1^{+}.

The microstrip transmission line is used as an open circuit λ/2 resonator with its ends terminated capacitors as shown in Figure 5-1. These capacitors shorten the physical length of the half-wavelength line and also permit the tuning and matching of the

resonator to the desired frequency. A capacitively terminated microstrip transmission line produces a standing wave with a current distribution peaking at the center of the conductor line inherently. The B_1^+ field generated by RF resonators may also gradually weaken away from the RF feed point (see solid line of Figure 5-1). Together, these effects can result in abrupt non-uniformity at the ends of the conductor in the microstrip transmission line resonator. By varying impedance along the line, the current density is controlled to obtain the desired magnetic near-field profile like the dotted-line in Figure 5-1.

5.2 Properties of B_1 at ultra-high field

5.2.1 B_1 field

The local magnetic field B_1 produced by RF coils can be expressed by

$$B_1 = \mathrm{x}B_{1x} + yB_{1y} + zB_{1z} \tag{5-1}$$

where B_{1x} and B_{1y} are complex magnitudes of the X- and Y- direction RF magnetic fields. The main static magnetic field is in the Z direction, so the z direction component of the RF field, B_{1z}, is a negligible part. By electromagnetic theory and the basic NMR physics [82-85], the transverse magnetic field B1 is divided into two parts, B_1^+ and B_1^-, with a circularly polarized component and given by

$$B_1{}^+ = (\mathrm{x} + \mathrm{jy})\frac{B_1}{\sqrt{2}} = \frac{1}{\sqrt{2}}(B_{1x} + jB_{1y}) \tag{5-2}$$

$$B_1{}^- = (\mathrm{x} - \mathrm{jy})\frac{B_1}{\sqrt{2}} = \frac{1}{\sqrt{2}}(B_{1x} - jB_{1y})^* \tag{5-3}$$

where the asterisk denotes a complex conjugate operation. B_1^+ is a positive circularly polarized magnetic field component, and this is responsible for exciting the protons and thus induces a flip angle toward the transverse plane, XY plane. Due to complex values, it has amplitudes and phases, and the imaginary part has out of phase with 90 degree. B_1^+ field is referred to RF transmit field because it rotates in the same direction of the proton's angular magnetic momentum. Therefore, it is a positive circularly polarized component. On the contrary, B1- is a negative circularly polarized magnetic field

component that has an opposite-rotation compared to the B_1^+ field. The B_1^- component can be measured in the RF coil rather than B_1^+ field in the RF relaxation period.

5.2.2 B_1 field inhomogeneity

RF effect, i.e. a shorter wavelength issue, is an inherent property of high frequency operation, and it is a very tricky problem technically. A major source of B_1 field inhomogeneity is different phases and the amplitude resulting from a short wavelength which can reach the dimension of the object, as shown in Figure 5-2 (a). Even if every point in the resonator of the multi-channel RF coil has the same power level, B1 transmitted field distribution at a short wavelength can be a constructive and destructive interference. In other words, different phases (θ_1, θ_2, θ_3) and amplitudes ($M(\theta_1)$, $M(\theta_2)$, $M(\theta_3)$) build bright or dark spots depending on the interferences overlapped signals as seen in Figure 5-2 (b). If the transmitted RF signals arrive at a voxel inside the object with the in-phase condition, the summation of these RF signals makes the maximum

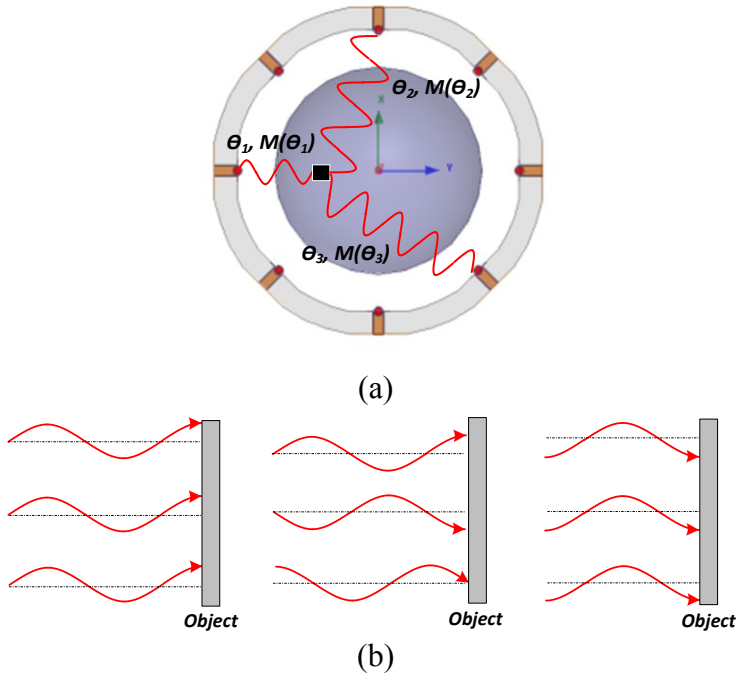

Figure 5-2. (a) Electromagnetic interference in the object with different phases and magnitudes and (b) different phases make non-equal magnitude according to location (left: maximum, center: mediocre, right: minimum magnitude).

intensity, the brightest spot. The RF signals with out of phase, however, are cancelled out, causing the darkest spot in MR image. When the Figure 3-4 is referred again to present the short wave effect, this wave effect makes a standing wave pattern with constructive and destructive interference within the object. At low frequencies, the signals do not change significantly over the interest region. In the contrary, the phase of signals significantly varies at high frequencies.

By the reference [86,87], MR signal intensity, $S_{(r)}$ is given by

$$S_{(r)} \propto \left| sin^3 \alpha_{(r)} \right| \tag{5-4}$$

$$\alpha_{(r)} \propto B_1^+(r) \int_t f(t)dt \tag{5-5}$$

where r is a position vector, α is a flip angle of the RF pulse applied (e.g. spin echo pulse sequence), and t is the time duration of RF pulse. The flip angle depends on the magnitude of RF transmitted pulse related to the RF power (i.e. energy). Thus, the B_1 field generated by RF coils directly affects the spatial uniformity of MR image. For example, when θ = 90°, the maximum signal intensity can be measured in RF coils.

5.2.3 Reciprocity of B1 field

In the last 5.2.1, B1 field is reviewed with the decomposed components; B_1^+ and B_1^-, associated with RF transmission and reception respectively. By Ampere's law in (5-6), RF transmit coil's magnetic field generation can be explained. the current enclosed by that path creates a magnetic field as expressed by

$$\frac{1}{\mu_0} \oint_C \mathrm{B} \cdot \mathrm{d}l = \int_S \mathrm{J} \cdot \mathrm{ds} \tag{5-6}$$

therefore, the uniform current distribution, J, can generate a uniform magnetic field B1 at the desired Larmor frequency of the protons. Following RF transmission (excitation), since the protons have the intrinsic angular momentum, spins cannot instantly realign with the main magnetic field (B_0), but begin to rotate clockwise in the XY direction. This

precession creates a magnetic field that induces electric field resulting in creating voltage ($V_{in\ coil}$) in RF receiving coil by Maxwell-Faraday equation

$$V_{in\ coil} \propto \oint_c E \cdot dl = -\int_S \frac{dB}{dt} ds \tag{5-7}$$

By reciprocity, the magnitude of the voltage induced in the RF receiver coil by protons is proportional to the magnitude of the particular magnetic field B_1 component produced by the RF transmitting power. From the previous part 5.2.1, the voltage induced on the transverse magnetization (XY plane) is proportional to the vector representing the polarization of the field that the RF coil transmits and the conjugate of a polarization vector that represents a field perfectly received by the protons.

Consequently, the spatial distribution sensitivity of RF coils is a linear function of the magnetic field B_1 generated by a current density flowing in the RF coil, thus homogenous MR images cannot be obtained without uniform B_1 field generation.

There is, however, one thing to be noted that MR signal received from the excited protons is completely uncorrelated to the process of exciting the protons because different sources generating electromagnetic field are used in RF transmission and reception part, respectively [87].

5.2.4 RF penetration

By the electromagnetic property, dielectric constant (ε_r) and conductivity (σ) are functions of frequency. As frequency increases in the sample, the relative permittivity of the tissue decreases, and the conductivity increases. The decrease in permittivity counteracts the reduction of wavelength in the sample and the effect is small. The increase in the conductivity, however, poses a major problem as SAR values are directly related to the conductivity of tissues. In a sample, penetration depth (δ) defined as the distance along the direction of propagation where the fields are attenuated to 1/e times their initial value. As RF wave penetration depths in tissues decrease, consequently a homogeneous RF coil can no longer generate a uniform B_1^+ field (transmit RF magnetic

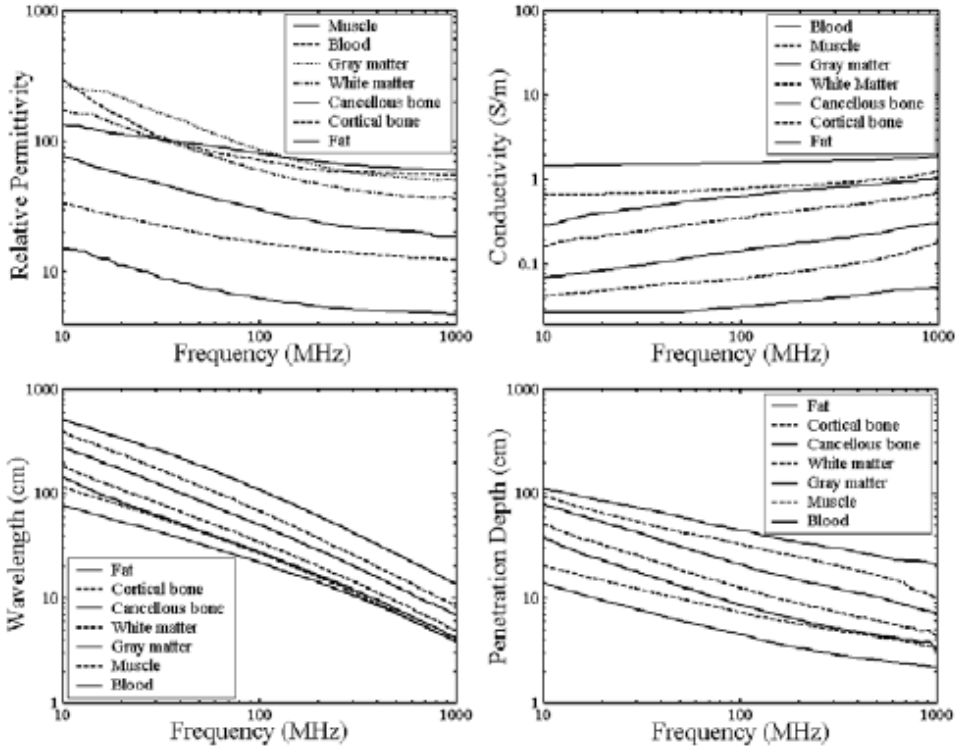

Figure 5-3. Relative permittivity, conductivity, wavelength and penetration depths as a functions of different tissues. (image captured from [2]

field component) in the head at higher magnetic field strength. Hence, more RF power is required to attain the same flip angles in an imaging protocol than it is at low fields, which leads to greater RF fields deposited in the tissue. Figure 5-3 shows some graphs containing the values of permittivity, conductivity, wavelength, and penetration depth up to 1 GHz according to different tissue types that is published by by Gabriel [2].

5.3 Previous approaches for B1 homogeneity

5.3.1 Resonator shapes

Recently, some papers have been published from hardware or physical manipulation to correct the RF field inhomogeneity [93-96]. Figure 5-4 shows previous approaches to the stepped or alternating impedance resonator shapes. The left side presents the current density on surface of the resonators, and the right side shows the magnetic field (H-field) results with previous approached structures using EM simulator, HFSS (by Ansys). As the aforementioned principle (referred to equations 5-6 and 5-7) of generating uniform magnetic field locally, the different shapes adjusting current density on the resonator's conductor are periodically utilized to create homogenous B_1 field. Stepped impedance resonators have been found to be advantageous when designing microwave filters. The microstrip transmission line has advantages to build the stepped impedance resonator because the control of current density is simple with the reduction or expansion of circuit size. Therefore, the stepped impedance resonator is composed of alternating narrows and

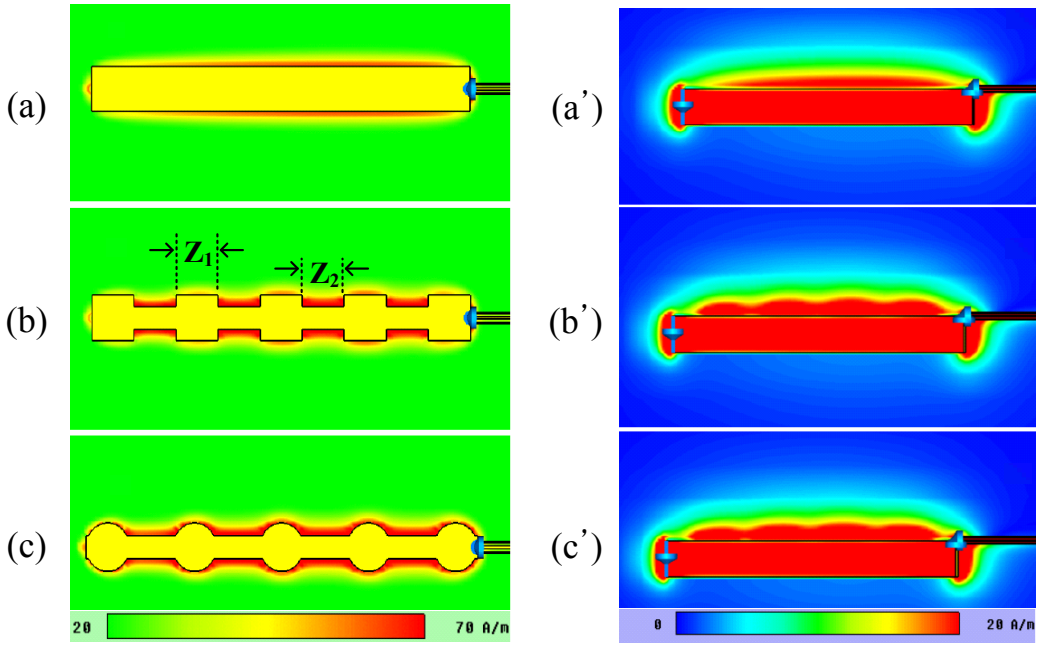

Figure 5-4. Previous approaches: (a) traditional microstrip line resonator, (b) stepped impedance resonator, and (c) alternating impedance microstrip resonator.

wide signal line sections where the narrow sections of the line are much greater in impedance than the wide sections of the line, $Z_2 >> Z_1$, as seen in Figure 5-4 (b). In the same manner, the third one, (c), is the alternating impedance resonator with circular elements across the coil axis.

When compared to a traditional microstrip line, the stepped and alternating impedance resonator leads to the high impedance section. It has greater current density along the outer edges of the narrow conductor section of line than it does along those of the wide section line for the same amount of total current. In other words, the current per unit length is the same in the narrow and wide sections of the stepped impedance resonator, but the narrow section has a much higher current density. By alternating sections of high- and low-characteristic impedance lines, the current density along the length of the line can be modulated. Although these approaches compensate the concave shape resulting from the shorter wavelength issue (RF effect), a drawback is that particular patterns are left in the near magnetic field affecting the flip angle of protons toward transverse plane (XY plane). Namely, these patterns bring inhomogeneity in MR images.

5.3.2 Multi-channel with phases and amplitude

The popular RF shimming methods are the adjustment and control of the phase and amplitude generated by individual RF coil element in the multi-channel RF coil as shown in Figure 5-5. By controlling the phase and amplitude, the inhomogeneity within the object can be compensated and corrected. RF pulse transmission from a set of coils utilizing multi-channel techniques is a process of development. Individual channel is used to transmit an independent RF pulse [101]. When combined, the pulses from the different channels give a result equivalent to longer and far more complex RF pulses. These variable phases and amplitudes methods that manipulate the B_1^+ field such as transmit SENSE have been seen as possible solutions for achieving uniform or specific B_1 field distributions [93]. In multi-element volume experiments, B_1^+ phase shimming can be performed by determining a set of transmit phases that will increase the B_1^+ phase coherence at a location in the object. These phases are calculated by averaging the relative transmitting phase of each transmit element over the chosen region of interest. B_1

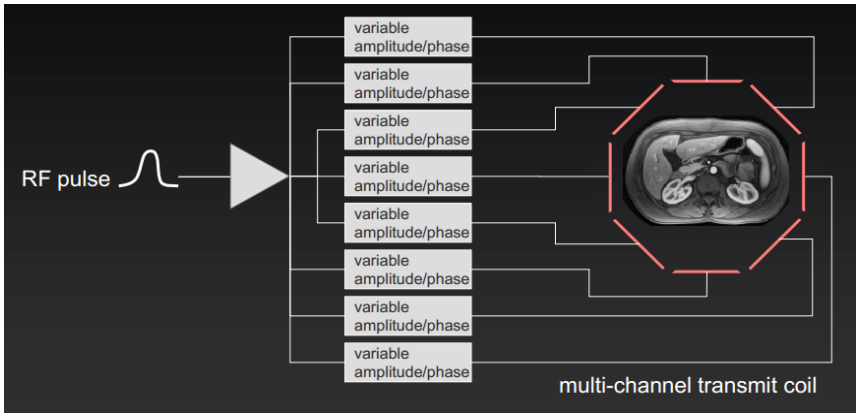

Figure 5-5. RF shimming to generate homogenous MR image with multi-channel optimized amplitudes and phases. (image captured from [91])

shimming is performed by subtracting these phases from each corresponding transmit elements having initial drive phase through the means of computer-controlled-phase-shifters for subsequent acquisitions during RF transmitting with all elements simultaneously. In most cases, this location is the center of the object. However, there are cases that the coils can't be physically centered on the desired location (heart, kidneys, etc.), and shimming needs to be performed at off-center positions. This technique requires additional hardware to produce the necessary driving signals, as independent transmit channels, power dividers, phase shifters, and attenuators.

5.4 Electromagnetic model and simulation

Electromagnetic simulator HFSS (by Ansys) based on the finite element method (FEM) is utilized to evaluate and analyze the proposed trapezoid-like resonator equipped with single element and multi-channel volume coil.

5.4.1 Single element model

For EM simulation model, the single trapezoid-like element is designed for 7T (f = 297.2MHz) and head images, and Teflon (ε_r=2.1 and dielectric loss tangent = 0.0002) is used for dielectric substrates. The dimensions of the substrate are 2cm (height), 5cm (width), and 16cm (length), respectively as seen in Figure 5-7. The trapezoid-like conductor shape of the resonator is made by copper (thickness = 34µm, 2cm width, and

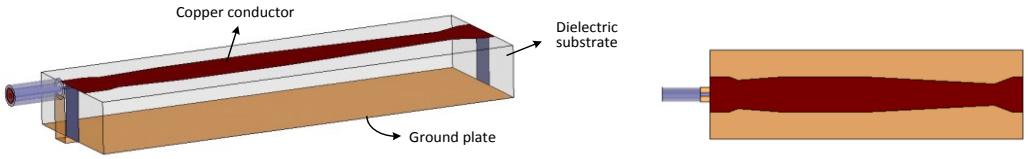

(a) (b)

Figure 5-6. (a) Single element model based on TEM resonator (b) top view of (a)

16cm length). Trapezoidal patterns asymmetrically are both sides concerned feed point resulting in the asymmetric field distribution, which gradually weakens away from the RF feed point. The strength of B_1^+ field, therefore, is proportional to the current flow per unit area in the conductor by Biot-Savert law. The electromagnetic field profiles with single coil elements are illustrated by HFSS simulation (Ansys) in Figure 5-7 and Figure 5-8. The surface current density of the double trapezoidal conductor is almost uniform in Figure 5-7 (c) compared with the traditional (a) and the previous study with stepped

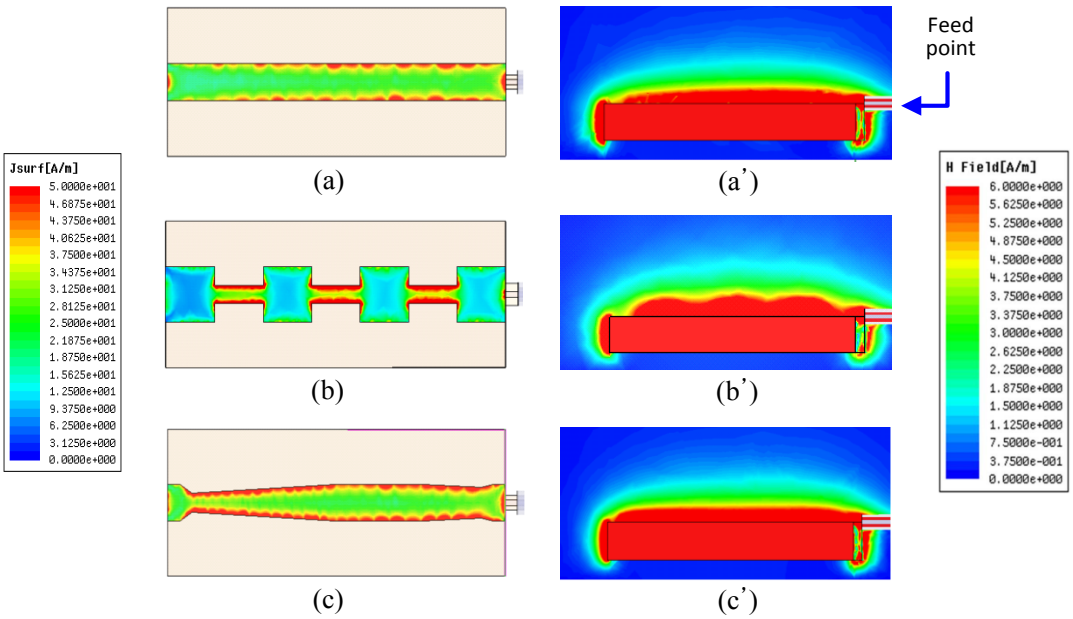

Figure 5-7. EM simulation results of the surface current density distributions and H-field (B_1^+) distributions along the conductor line: (a) the conventional microstrip transmission line resonator, (b) stepped impedance resonator, and (c) the proposed double trapezoid-

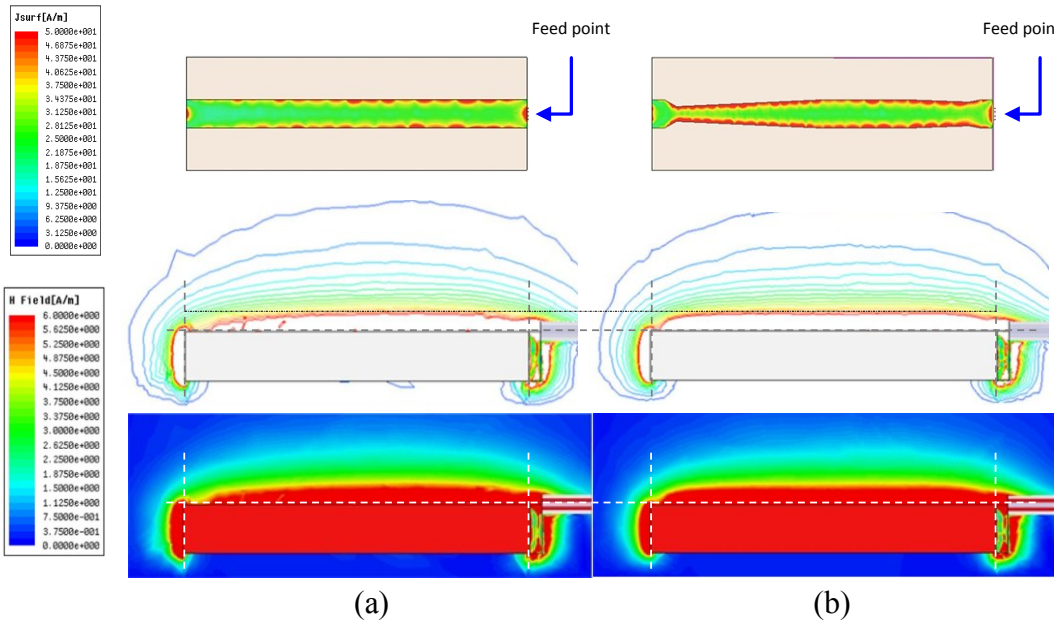

Figure 5-8. Comparisons between the conventional and proposed resonator with surface current density and H-filed (B_1^+) distributions along the conductor line.

impedance (b) shapes. The magnetic transmitted B_1^+ fields are shown in Figure 5-7 (a'), (b'), and (c'). The B_1^+ field profiles are linearly identical to the current density distributions, respectively. The coaxial cable characterized with 50Ω line is connected to the capacitors for matching and tuning. The model is matched to 50Ω at 297.2MHz for 7T MRI. The results of the simulation are able to check whether the current distribution of the traditional microstrip line resonator is uneven, the peak of B_1^+ magnetic field profile is located at the center region, and the fade way along the conducting line can be observed in Figure 5-7 (a').

Figure 5-8 shows the results of B_1^+ field distributions consistent with the surface current density of conductors between the traditional and proposed structure in more detail. The modified conductor shapes like the double-sides trapezoidal pattern in Figure 5-8 (b) generate flat field intensity and gradually compensate a partial diminution point to obtain the constant field intensity by using the inverse proportion between the width of

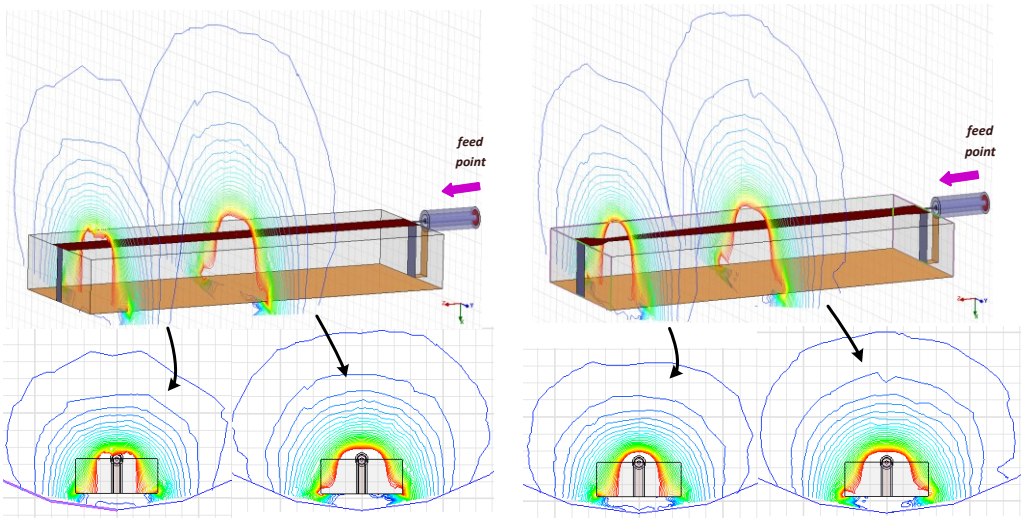

Figure 5-9. Transection views at the center and end side of resonator. (a) traditional single element (b) proposed double-sides trapezoid-like element.

the conductor and field depth. Figure 5-9 ensures benefit from the proposed double-sides trapezoid-like shape of the resonator. Although the signal strength and distributions are almost identical at the center sides, the shape of the traditional resonator has destructive B_1^+ field at the end side resulting from inhomogeneous current distribution along Z direction. At the end transection view, the proposed double-sides trapezoid-like resonator has very similar intensity and distribution with the property at the center side.

5.4.2 Multi-channel volume coil model

Since the characteristics of single element were evaluated, multi-channel volume coil models have been designed and simulated. 8 channels are constructed with individual elements side by side with same parameters of single element, and the diameter of coil is 25cm. Capacitances at the end from the feed points are fixed with 2.2pF to reduce the size of resonator, and matching and tuning capacitances are 4.65pF and 8.2pF, respectively. As seen in Figure 5-10 (a) and (b), the phantom modeled by relative permittivity (ε_r = 58.1) and bulk conductivity (σ = 0.539 Siemens/m) has been loaded, and then tuning capacitor and matching capacitor have been adjusted to tune the frequency at

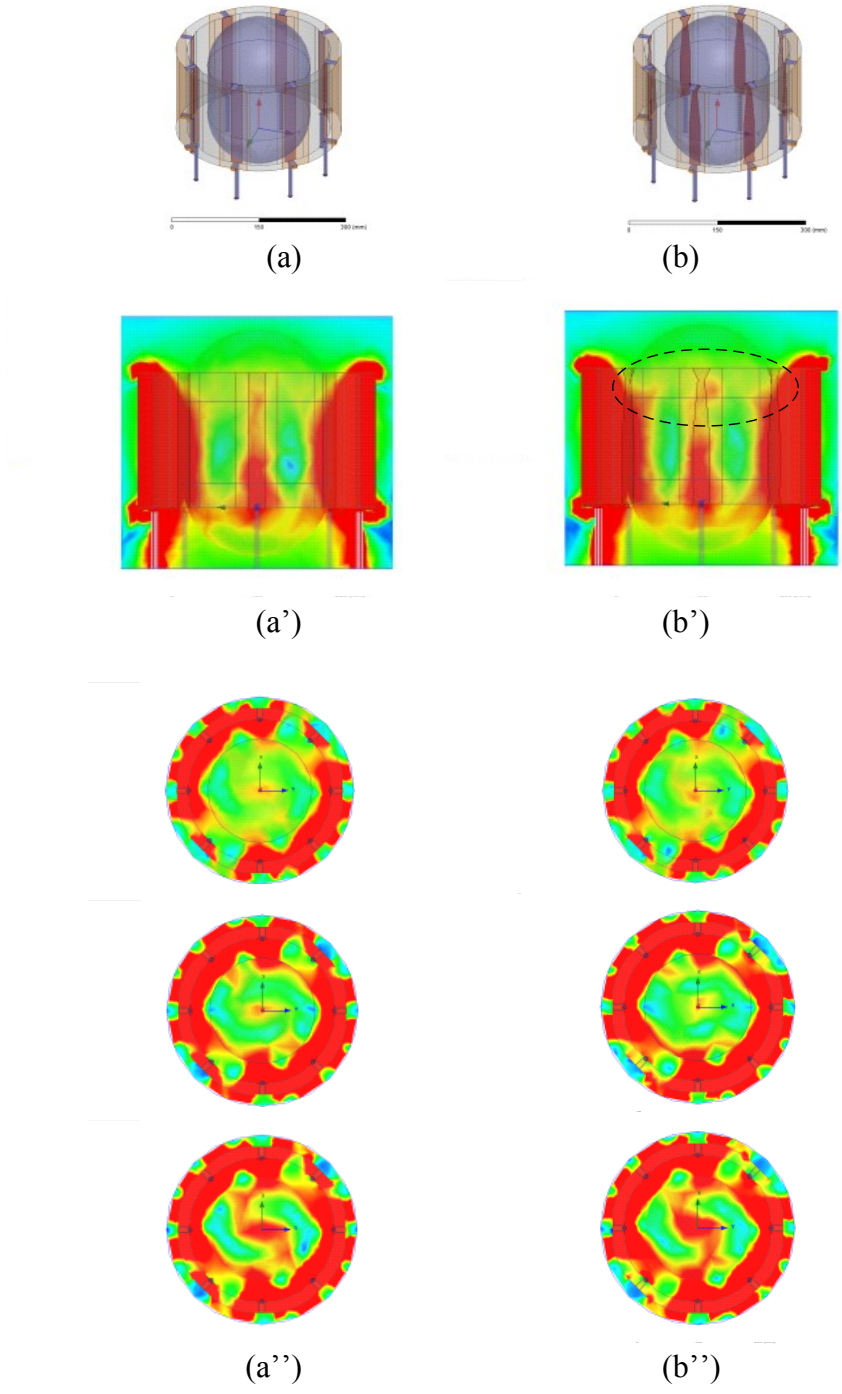

Figure 5-10. Multi-channel volume coil simulations with a phantom: (a) the traditional and (b) double-side trapezoidal resonator.

desired Larmor frequency and matched the impedance to 50Ω coaxial cable. Each element was excited with 45° phase difference. The final capacitances range was from 4.55pF to 4.65pF for matching and from 8.1pF to 8.65pF for tuning, respectively after the phantom was loaded, and matching was done. Figure 5-10 (a') and (b') are vertical plane slice at the center, and (a'') and (b'') are horizontal plane slices, the end, center, front side, sequentially. The improved b_1^+ fields are presented in the dotted-circuit in (b') and the top slice in (b'') resulting in the improved homogeneity.

Another benefit of the double trapezoidal shape resonator is high Q factor and Q_{ratio}

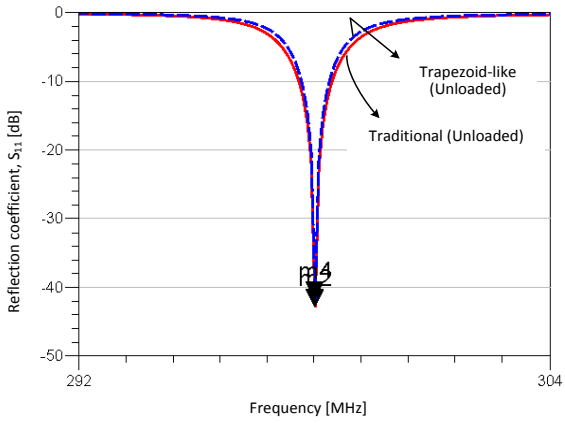

(a)

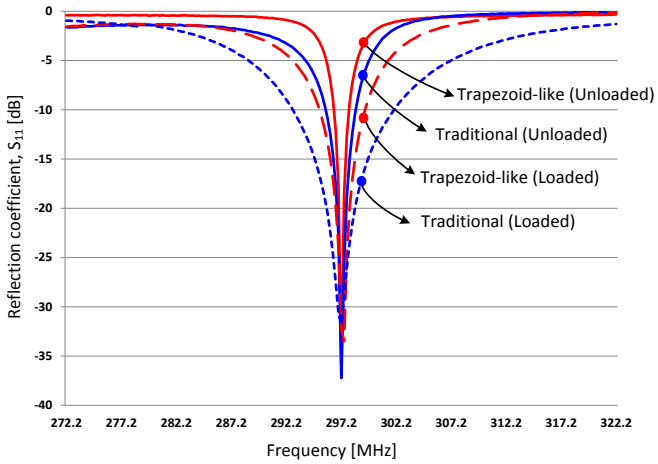

(b)

Figure 5-11. (a) EM simulation and (B) measure reflection coefficient (S_{11}) to compare.

Table 5-1. Comparisons of Q and Q_{ratio}

	Resonator shape	-3dB Bandwidth [MHz]	Q
Unloaded	Trapezoidal	4.6	64.6
	Traditional	10	29.7
Loaded	Trapezoidal	11.7	25.4
	Traditional	15.8	18.8

	Q_{ratio}
Trapezoidal-like shape	**2.54**
Conventional shape	**1.58**

compared with the traditional rectangular shape resonator because the density of the uniform current reduces the impedance bump (mismatch) factor inside the conductor material. As a result, the intrinsic loss of the RF coil can be decreased when the current distribution is controlled. Figure 5-11 show the result of the EM (HFSS) simulation as in (a) and an experimental measured reflection coefficient (S_{11}) as in (b). The result from the simulation to the experimental measured results containing unloaded and loaded cases, respectively. For this experiment, the same dimensions and geometry of the RF coil are used after tuning at 297.2MHz and matching to 50Ω. The phantom for the loading effect is the same one dealt in the next experimental setup part. Increased Q_{ratio} is shown in table 5-1. For Q measurement, the -3dB bandwidth and the center frequency have been measured in each unloaded and loaded condition with a network analyzer and computed Q_{ratio} by the equation in 2-14. As a result, Qratio is enhanced from 1.58 to 2.54, namely, about 60%.

5.5 8-channel head volume coil design with improved B1 field uniformity

Two 8-channel 7T head coils, one conventional design and one trapezoidal design, have been built in Figure 5-12. The coils have the same dimensions and the matching and tuning methods including the same capacitances for the terminating capacitors. Each element comprised of a low loss Teflon substrate (ε_r = 2.2) with height and length of 1.9cm and 16cm respectively. the width of the copper taped conductor was 1.9cm and is cut down to the minimum dimension of 0.9cm on the side away from the coaxial cable and 1.3cm for the side near the coaxial feed. Each element was individually matched to the 50 Ω coaxial cable tuned to 297.2MHz for the Siemens Magnetom 7T MRI. To improve the isolation between adjacent elements, wide strips of copper tape were used to build capacitances between channels. For tuning and matching capacitors, by NMA10 (1~ 10pF, 1000V) Voltronics are used, C-type capacitor (4.4pF, 2500V) by ATC is used for the end-capacitor with fixed value.

5.6 Experimental setup and results at 7T

Experiments were performed with a cylindrical 8 liter phantom filled with a sucrose/saline solution (ε_r = 58.1and σ = 0.539 S/m) that was positioned at the same location for each experiment in the 7T MR system (by Siemens) based on the 90cm bore

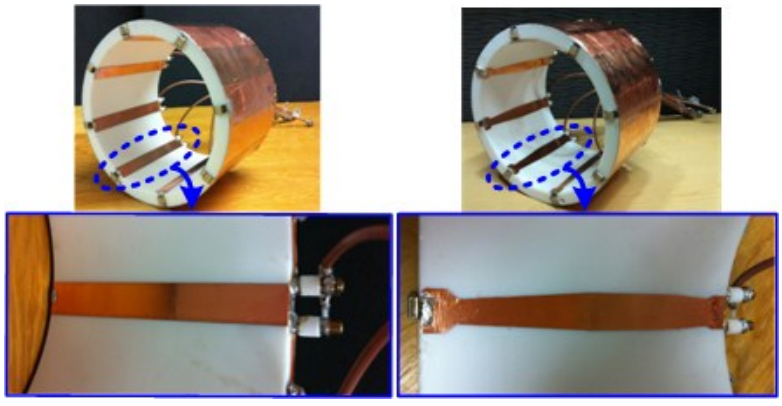

(a) (b)

Figure 5-12. (a) the conventional and (b) the proposed double trapezoid-like 8 channel head coils and individual elements

actively shielded magnet established in the Center for Magnetic Resonance Research (CMRR) University of Minnesota. An 8-liter cylindrical phantom was designed to represent the electrical properties of the head Figure 5-13 (a)). The phantom was chosen to be roughly the same diameter as a human head and long enough to represent the neck. The phantom was designed with the recipe given in ref. [91] and consisted of sucrose (47.6%), distilled water (51.1%), and salt (1.3%). The 8-liter bottle was filled with 5071.7

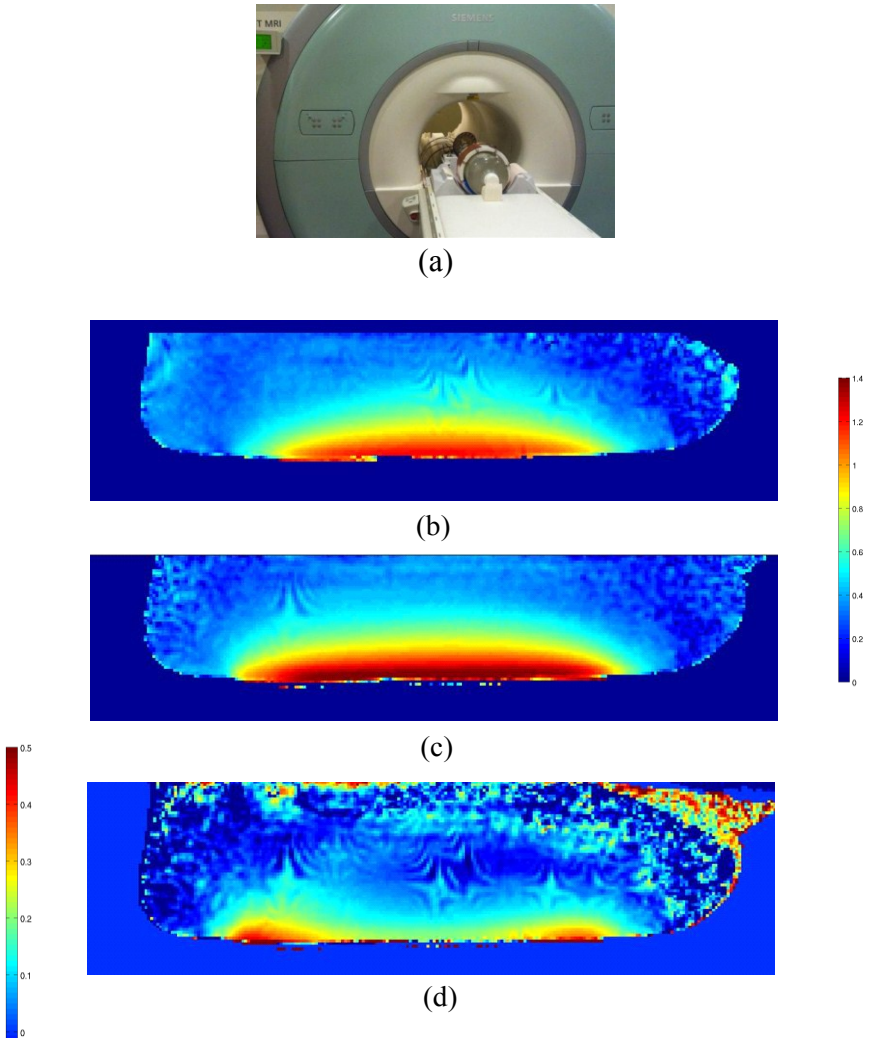

Figure 5-13. Experimental B_1^+ map results (μT/sqrt(W)) along the length of the element; (a) the conventional single element (b) the proposed double trapezoid-like single element and (c) the subtraction from (b) to (a).

g of sucrose, 4717.1 g of water, and 129.1 g of salt to attain the percent volume specifications of the recipe. Each of the eight RF outputs was wired to custom-built Transmit/Receive (T/R) switches allowing for both transmitting and receiving operations. For final image reconstruction, images from each receiving element were simply combined as the root of the sum of squares. B_1^+ mapping and B_1^+ shimming calculations were performed in Matlab software. In phantom experiments, incremental geometric phase sets were used for B1 + mapping and the neighboring elements drive phases were incremented by 45 degrees.

Figure 5-13 (a) shows the experimental setup in Siemens Magnetom 7T MRI, and Figure 5-13 (b)-(d) presents the penetration depth and width of the B_1^+ map inside a cylindrical phantom along the line (sagittal plane) from experimental results. The microstrip transmission line element at the resonance inherently generates a B_1^+ profile with the field peaking at the center of the line, and the strength of the magnetic field strength falls off sharply at the edges of the coil compared to the middle of the resonant element in Figure 5-13 (b). On the other hand, compared to the traditional conductor of resonator, the proposed double trapezoidal shape has a more uniform field distribution with higher intensity because of the balanced resonant circuit parameters and higher current density (Figure 5-13 (c)). Figure 5-13 (d) shows the subtraction results from (c) to (b). It means that the proposed double trapezoidal coil element has about 35% and 25% higher B_1^+ field at the capacitive terminated region and feed point region, respectively as well as about 13% improved at the center. In Figure 5-14 (a) and (c), the B_1^+ field distribution and intensity of the proposed coil structure in the transverse planes are also stronger than the standard coil element compared to Figure 5-14 (b) and (d) around the center and ending regions, respectively. Figure 5-14 (e) shows B_1^+ map using the proposed double trapezoidal conductor shape 8-channel head coil performed with high symmetry and isolation (< -17dB) with adjacent channels.

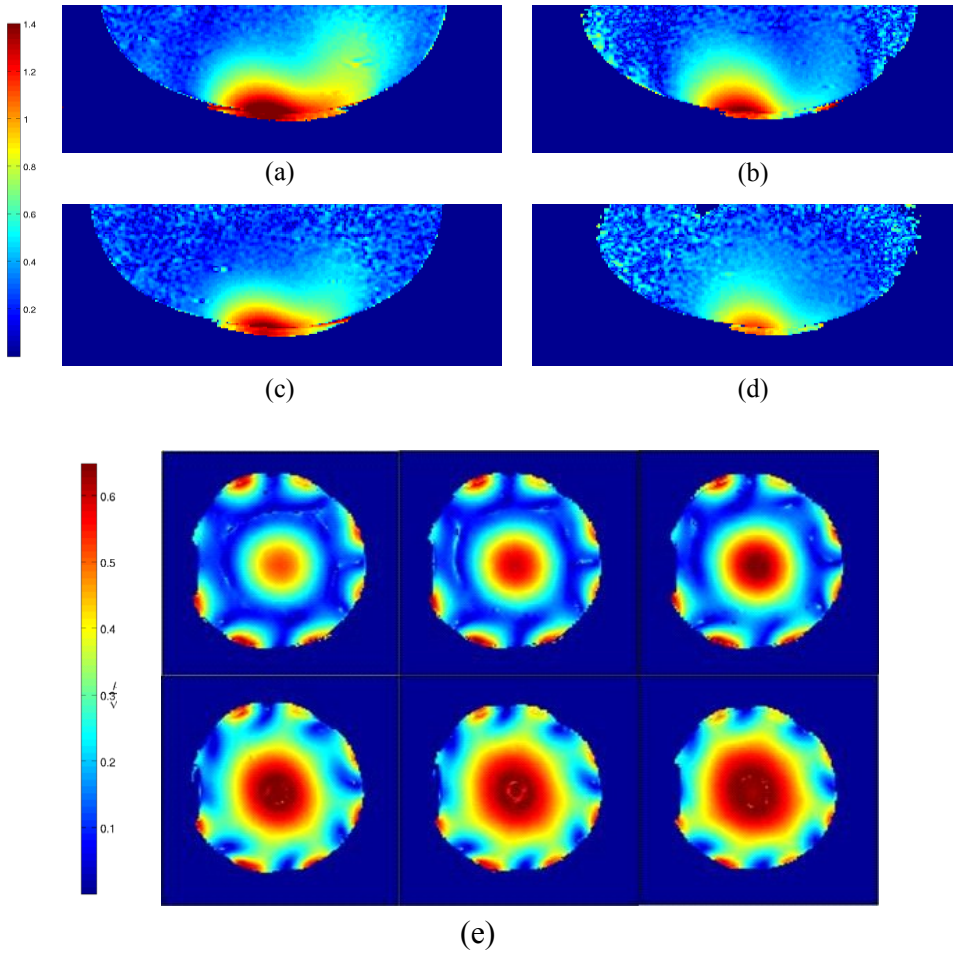

Figure 5-14. Experimental B_1^+ map results (μT/sqrt(W)) in a cylindrical phantom for a planes perpendicular to the length of the element. The central slices for (a) the proposed (b) conventional single coil element, and an end region slices for (c) the proposed (d) conventional single coil element, and (e) the transverse plane.

Chapter 6. **Conclusions**

The main contribution of the project in this dissertation is that the design of the RF coil with the automatic tuning and matching function has been successfully constructed and evaluated.

This dissertation presents two major parts:

The first part introduces the fully electric controlled stand-alone system for the automatic tuning and matching of the RF coil based on the TEM structure at 7T MRI systems. A number of challenges arose while studying and designing the RF/electronic circuits to develop the automatic impedance matching and frequency tuning unit containing a real-time RF power measuring circuit, capacitor arrays with PIN diode switches, PIN diode switching drivers, and the main control and decision circuits implemented in FPGA. Among many difficulties, it took time and effort to figure out RF grounding problems, RF radiation effects, and the limitation of the traditional L match network. A single element of the RF coil was designed to solve these problems. Successful development of single element with the automatic tuning and matching function has motivated me to develop 8-channel volume RF head coil. The 8-channel RF head coil has been successfully built and tested. The fully automatic tuning and matching RF coil offers the feasibility of overcoming the existing method, time-consuming manual tuning and matching. In fact, the proposed system is incomparably better than the manual process because the results of the proposed automatic tuning and matching unit gives fast operation, accurate impedance matching / frequency tuning resulting in the high power efficiency. Applications of this method can be a breakthrough for the current and future clinical RF coil performance.

In the second part, a TEM-based RF head coil with double trapezoidal microstrip conductor shape is introduced to generate the uniform B_1^+ field along the length of the resonator. By simulations and experiments, the proposed head coil demonstrates the improved B_1^+ field uniformity along the RF signal conductor and the compensation of the field deterioration at the ends of coil. This technique can be a strong candidate for RF shimming, and it provides high quality MR images without locally anomalous contrast.

Bibliography

(1) Marzola, P., F. Osculati, et al. (2003). "High field MRI in preclinical research." Eur J Radiol 48(2): 165-170.
(2) Berliner, P.-M. R. a. L. (2006). Ultra High Field Magnetic Resonance Imaging, Springer.
(3) Duyn, J. H. (2012). "The future of ultra-high field MRI and fMRI for study of the human brain." Neuroimage 62(2): 1241-1248.
(4) Schick, F. (2005). "Whole-body MRI at high field: technical limits and clinical potential." European radiology 15(5): 946-959.
(5) Blamire, A. M. (2008). "The technology of MRI: the next 10 years?" Br J Radiol 81(968): 601-617.
(6) Dai, J. (2006). Opportunities and Challenges of MRI in the Developing World ISMRM: 2.
(7) Wada, H., M. Sekino, et al. (2010). "Prospect of High-Field MRI." Applied Superconductivity, IEEE Transactions on 20(3): 115-122.
(8) Webb, A. G. and C. M. Collins (2010). "Parallel transmit and receive technology in high-field magnetic resonance neuroimaging." Int. J. Imaging Syst. Technol. 20(1): 2-13.
(9) Ying, L. and L. Zhi-Pei (2010). "Parallel MRI Using Phased Array Coils." Signal Processing Magazine, IEEE 27(4): 90-98.
(10) Sung-Min, S., J. T. Vaughan, et al. (2011). Auto-tuning of the RF transmission line coil for high-fields magnetic resonance imaging (MRI) systems. Microwave Symposium Digest (MTT), 2011 IEEE MTT-S International.
(11) G. Scott, K. Y. (2005). Wireless Transponders for RF Coils: Systems Issues. ISMRM.
(12) Long-Sheng, F., S. S. H. Hsu, et al. (2007). Miniaturization of Magnetic Resonance Microsystem Components for 3D Cell Imaging. Solid-State Circuits Conference, 2007. ISSCC 2007. Digest of Technical Papers. IEEE International.
(13) Possanzini, C. dStream architecture. available in http://www.healthcare.philips.com
(14) M. Pavan, a. K. P. P. (2010). A MODULAR AUTOMATIC MATCHING NETWORK SYSTEM. ISMRM: 647.
(15) Mark A. Brown, R. C. S. (2010). MRI: Basic Principles and Applications, Wiley-Blackwell.
(16) Bushong, S. C. (2003). Magnetic Resonance Imaging: Physical and Biological Principles, Mosby.
(17) Graaf, R. A. d. (2007). In Vivo NMR Spectroscopy: Principles and Techniques, Wiley-Interscience.
(18) Purcell, E. M., H. C. Torrey, et al. (1946). "Resonance Absorption by Nuclear Magnetic Moments in a Solid." Physical Review 69(1-2): 37-38.
(19) Bloch, F. (1946). "Nuclear Induction." Physical Review 70(7-8): 460-474.
(20) Ray Hashman Hashemi, W. G. B. a. C. J. L. (2010). MRI: The Basics, Lippincott Williams & Wilkins.
(21) Vaughan, J. T.,Griffiths. V. a. J. R. (2012). RF Coils for MRI, Wiley.
(22) Adriany, G., E. J. Auerbach, et al. (2010). "A 32-channel lattice transmission line array for parallel transmit and receive MRI at 7 tesla." Magn Reson Med 63(6): 1478-1485.
(23) MR Field Notes. Vol. 1, No. 2 Spring 2005
(24) Atlas, Scott W (2008). Magnetic Resonance Imaging of the Brain and Spine, Lippincott Williams & Wilkins.
(25) Hayes, C. E. (1987). RADIO FREQUENCY FIELD COIL FOR NMR. 4,692,705, USA, General Electric Company.

(26) Hayes, C. E. (2007). Birdcage Resonators: Highly Homogeneous Radiofrequency Coils for Magnetic Resonance. eMagRes, John Wiley & Sons, Ltd.
(27) John Thomas Vaughan, J. (1999). Radio frequency volume coils for imaging and spectroscopy. 5,886,596, USA.
(28) Vaughan, J. T., G. Adriany, et al. (2004). "Efficient high-frequency body coil for high-field MRI." Magn Reson Med 52(4): 851-859.
(29) Vaughan, J. T., G. Adriany, et al. (2002). "Detunable transverse electromagnetic (TEM) volume coil for high-field NMR." Magnetic Resonance in Medicine 47(5): 990-1000.
(30) Vaughan, J. T., C. Snyder, et al. (2006). Current and Future Trends in Magnetic Resonance Imaging (MRI). Microwave Symposium Digest, 2006. IEEE MTT-S International.
(31) Hoult, D. I. and R. E. Richards (1976). "The signal-to-noise ratio of the nuclear magnetic resonance experiment." Journal of Magnetic Resonance (1969) 24(1): 71-85.
(32) Hayes, C. E. (2011). What is an RF coil? ISMRM.
(33) El-Sharkawy, A. M., D. Qian, et al. (2012). "A multichannel, real-time MRI RF power monitor for independent SAR determination." Med Phys 39(5): 2334-2341.
(34) Kuperman, Vadim (2000). Magnetic Resonance Imaging: Physical Principles and Applications, Academic Press.
(35) Hayes, C. E. (2009). "The development of the birdcage resonator: a historical perspective." NMR in Biomedicine 22(9): 908-918.
(36) R. Venook, G. G., B. Hu, G. Scott (2003). Automatic Varactor Tuning of Interventional RF Receiver Coils. ISMRM: 686.
(37) Pozar, David M (1990), Microwave Engineering, Addison Wesley.
(38) Ludwig, Reinhold (2008), RF Circuit Design: Theory & Applications, Prentice Hall.
(39) Fujita, H. (2007). "New horizons in MR technology: RF coil designs and trends." Magn Reson Med Sci 6(1): 29-42.
(40) Barberi, E. A., J. S. Gati, et al. (2000). "A transmit-only/receive-only (TORO) RF system for high-field MRI/MRS applications." Magnetic Resonance in Medicine 43(2): 284-289.
(41) Magin, R. L., A. G. Webb, et al. (1997). "Miniature magnetic resonance machines." Spectrum, IEEE 34(10): 51-61.
(42) Gu, Q. and A. S. Morris (2013). "A New Method for Matching Network Adaptive Control." Microwave Theory and Techniques, IEEE Transactions on 61(1): 587-595.
(43) Zhang, X., K. Ugurbil, et al. (2003). "A microstrip transmission line volume coil for human head MR imaging at 4T." J Magn Reson 161(2): 242-251.
(44) Omar, A., R. Caverly, et al. (2011). "A Microwave Engineer's View of MRI." Microwave Magazine, IEEE 12(3): 78-86.
(45) de Alejo, R. P., C. Garrido, et al. (2004). "Automatic tuning and matching of a small multifrequency saddle coil at 4.7 T." Magn Reson Med 51(4): 869-873.
(46) Fanfan, M., A. van Bezooijen, et al. (2006). A Mismatch Detector for Adaptive Antenna Impedance Matching. Microwave Conference, 2006. 36th European.
(47) Hang, S., J. T. Aberle, et al. (2010). "A Mixed-Signal Matching State Search Based Adaptive Antenna Tuning IC." Microwave and Wireless Components Letters, IEEE 20(10): 581-583.
(48) Venook, R. D., B. A. Hargreaves, et al. (2005). "Automatic tuning of flexible interventional RF receiver coils." Magn Reson Med 54(4): 983-993.
(49) Regatte, R. R. and M. E. Schweitzer (2007). "Ultra-high-field MRI of the musculoskeletal system at 7.0T." J Magn Reson Imaging 25(2): 262-269.
(50) Marinus T. Vlaardingerbroek, J. A. B. (2004). Magnetic Resonance Imaging, Springer.

(51) Avdievich, N. I. and H. P. Hetherington (2009). "High-field head radiofrequency volume coils using transverse electromagnetic (TEM) and phased array technologies." NMR Biomed 22(9): 960-974.
(52) Sadeghzadeh, R. A. and N. J. McEwan (1994). "Prediction of head proximity effect on antenna impedance using spherical wave expansions." Electronics Letters 30(17): 1365-1366.
(53) Whitaker, J. (1996). The Electronics Handbook, CRC-Press.
(54) de Mingo, J., A. Valdovinos, et al. (2004). "An RF electronically controlled impedance tuning network design and its application to an antenna input impedance automatic matching system." Microwave Theory and Techniques, IEEE Transactions on 52(2): 489-497.
(55) Dongjiang, Q., Z. Yu, et al. (2005). Antenna impedance mismatch measurement and correction for adaptive CDMA transceivers. Microwave Symposium Digest, 2005 IEEE MTT-S International.
(56) Whatley, R. B., Z. Zhen, et al. (2006). "Reconfigurable RF impedance tuner for match control in broadband wireless devices." Antennas and Propagation, IEEE Transactions on 54(2): 470-478.
(57) Sung-Min, S., L. DelaBarre, et al. (2012). Pi-matching technique for RF coil of MRI systems. Microwave Symposium Digest (MTT), 2012 IEEE MTT-S International.
(58) Hwang, F. and D. I. Hoult (1998). "Automatic probe tuning and matching." Magn Reson Med 39(2): 214-222.
(59) (1994). The RF capacitor handbook, American technical ceramics.
(60) Doss, M. M. (1996). A fast adaptive technique for impedance matching networks. Electrotechnical Conference, 1996. MELECON '96., 8th Mediterranean.
(61) B. L. Beck, S. W., W. J. Turner, R. Bashirullah, and T. H. Mareci (2011). High Q Reactive Network for Automatic Impedance Matching ISMRM: 1853.
(62) Avdievich, N. I. and H. P. Hetherington (2009). "High-field head radiofrequency volume coils using transverse electromagnetic (TEM) and phased array technologies." NMR Biomed 22(9): 960-974.
(63) Kaya, A. and E. Y. Yuksel (2007). "Design of a new impedance tuning network by using RC mutator." Microwave and Optical Technology Letters 49(2): 298-302.
(64) Avdievich, N. I. and H. P. Hetherington (2009). "High-field head radiofrequency volume coils using transverse electromagnetic (TEM) and phased array technologies." NMR Biomed 22(9): 960-974.
(65) W.E.Doherty, J. a. R. D. J. (1998) THE PIN DIODE CIRCUIT DESIGNERS' HANDBOOK.
(66) Caverly, R. H. and G. Hiller (1990). "Establishing the minimum reverse bias for a p-i-n diode in a high-power switch." Microwave Theory and Techniques, IEEE Transactions on 38(12): 1938-1943.
(67) Tim Raper and Steve Knauber (1999). Designing for Electromagnetic interferecen (EMI) compliance. Advanced Micro Devices, Inc.
(68) EMI, RFI, and Shielding concepts. MT-095, Tutorial, Analog Devices.
(69) Vaughan, T., M. Garwood, et al. (2001). Volume coils for highest field MRI. Antennas and Propagation Society International Symposium, 2001. IEEE.
(70) Firrao, E. L., A. J. Annema, et al. (2008). "An Automatic Antenna Tuning System Using Only RF Signal Amplitudes." Circuits and Systems II: Express Briefs, IEEE Transactions on 55(9): 833-837.
(71) Nemati, H. M., C. Fager, et al. (2009). "Design of Varactor-Based Tunable Matching Networks for Dynamic Load Modulation of High Power Amplifiers." Microwave Theory and Techniques, IEEE Transactions on 57(5): 1110-1118.
(72) Vaughan, T., L. DelaBarre, et al. (2006). "9.4T human MRI: Preliminary results." Magnetic Resonance in Medicine 56(6): 1274-1282.
(73) Hoult, D. I., D. Foreman, et al. (2008). "Overcoming high-field RF problems with non-magnetic Cartesian feedback transceivers." Magma 21(1-2): 15-29.

(74) Hang, S., B. Bakkaloglu, et al. (2009). A CMOS adaptive antenna-impedance-tuning IC operating in the 850MHz-to-2GHz band. Solid-State Circuits Conference - Digest of Technical Papers, 2009. ISSCC 2009. IEEE International.
(75) C. J. Snyder, L. D., C. Akgun, S. Moeller, G. Adriany, K. Ugurbil, J. T. Vaughan (2006). High-Field Transmission Line Arrays for Transmit and Receive ISMRM: 421.
(76) Chung-Kwang, C., J. A. McDougall, et al. (1997). "RF heating of implanted spinal fusion stimulator during magnetic resonance imaging." Biomedical Engineering, IEEE Transactions on 44(5): 367-373.
(77) Clare, S., M. Alecci, et al. (2001). "Compensating for B1 inhomogeneity using active transmit power modulation." Magnetic resonance imaging 19(10): 1349-1352.
(78) Cohen, M. S., R. M. DuBois, et al. (2000). "Rapid and effective correction of RF inhomogeneity for high field magnetic resonance imaging." Hum Brain Mapp 10(4): 204-211.
(79) Collins, C. M., W. Liu, et al. (2005). "Central brightening due to constructive interference with, without, and despite dielectric resonance." Journal of Magnetic Resonance Imaging 21(2): 192-196.
(80) Collins, C. M. and Z. Wang (2011). "Calculation of radiofrequency electromagnetic fields and their effects in MRI of human subjects." Magnetic Resonance in Medicine 65(5): 1470-1482.
(81) Hoarau, C., N. Corrao, et al. (2008). "Complete Design and Measurement Methodology for a Tunable RF Impedance-Matching Network." Microwave Theory and Techniques, IEEE Transactions on 56(11): 2620-2627.
(82) Barker, G. J., A. Simmons, et al. (1998). "A simple method for investigating the effects of non-uniformity of radiofrequency transmission and radiofrequency reception in MRI." Br J Radiol 71(841): 59-67.
(83) IbIbrahim, T. S., Y. K. Hue, et al. (2009). "Understanding and manipulating the RF fields at high field MRI." NMR Biomed 22(9): 927-936.
(84) Ibrahim, T. S., C. Mitchell, et al. (2005). "Electromagnetic perspective on the operation of RF coils at 1.5-11.7 Tesla." Magn Reson Med 54(3): 683-690.
(85) Keltner, J. R., J. W. Carlson, et al. (1991). "Electromagnetic fields of surface coil in vivo NMR at high frequencies." Magnetic Resonance in Medicine 22(2): 467-480.
(86) Hoult, D. I. (2000). "The principle of reciprocity in signal strength calculations—A mathematical guide." Concepts in Magnetic Resonance 12(4): 173-187.
(87) Irahim, T. S. (2005). "Analytical approach to the MR signal." Magn Reson Med 54(3): 677-682.
(88) Mekle, R., W. van der Zwaag, et al. (2008). "Comparison of three commercially available radio frequency coils for human brain imaging at 3 Tesla." Magma 21(1-2): 53-61.
(89) Bitz, A. K. RF Simulation for Ultra-High Field MR Systems: Coil Design and Safety. available in http://www.cst.com/Content/Events/downloads/euc2012/Talk_3-2-2_CST_EUC_2012.pdf
(90) Ming-Hong, L. and C. Chien-Wen (2011). Human-body effects on the design of card-type UHF RFID tag antennas. Antennas and Propagation (APSURSI), 2011 IEEE International Symposium on.
(91) Morrow, G. (2000). "Progress in MRI magnets." Applied Superconductivity, IEEE Transactions on 10(1): 744-751.
(92) Muftuler, L. T., G. Gulsen, et al. (2002). "Automatic tuned MRI RF coil for multinuclear imaging of small animals at 3T." J Magn Reson 155(1): 39-44.
(93) Akgun, C. E., L. DelaBarre, et al. (2010). Alternating impedance multi-channel transmission line resonators for high field magnetic resonance imaging. Microwave Symposium Digest (MTT), 2010 IEEE MTT-S International.

(94) Akgun, C. E., L. DelaBarre, et al. (2009). Novel multi-channel transmission line coil for high field magnetic resonance imaging. Microwave Symposium Digest, 2009. MTT '09. IEEE MTT-S International.
(95) Sung-Min, S., L. DelaBarre, et al. (2012). RF multi-channel head coil design with improved B1+ Fields uniformity for high field MRI systems. Microwave Symposium Digest (MTT), 2012 IEEE MTT-S International.
(96) Elabyad, I.A (2011), "An Investigation of Alternating Impedance Microstrip Transceiver Coil Arrays for MRI at 7T," Microwave Symposium Digest, 2011 IEEE MTT-S international.
(97) Okoniewski, M. and M. A. Stuchly (1996). "A study of the handset antenna and human body interaction." Microwave Theory and Techniques, IEEE Transactions on 44(10): 1855-1864.
(98) Po, F. C. W., E. De Foucauld, et al. (2008). An vector automatic matching system designed for wireless medical telemetry. Circuits and Systems and TAISA Conference, 2008. NEWCAS-TAISA 2008. 2008 Joint 6th International IEEE Northeast Workshop on.
(99) Rahmat-Samii, Y., L. I. Williams, et al. (1995). "The UCLA bi-polar planar-near-field antenna-measurement and diagnostics range." Antennas and Propagation Magazine, IEEE 37(6): 16-35.
(100) Rehman, M. U., Y. Gao, et al. (2007). Effects of Human Body Interference on the Performance of a GPS Antenna. Antennas and Propagation, 2007. EuCAP 2007. The Second European Conference on.
(101) Sankey, L. and Z. Popovic (2009). Adaptive tuning for handheld transmitters. Microwave Symposium Digest, 2009. MTT '09. IEEE MTT-S International.
(102) Scanlon, W. G., N. E. Evans, et al. (1996). Antenna-body interaction effects in a 418 MHz radio telemeter for infant use. Engineering in Medicine and Biology Society, 1996. Bridging Disciplines for Biomedicine. Proceedings of the 18th Annual International Conference of the IEEE.
(103) U. Katscher, P. Bornert, C. Leussler et al. (2003), "Transmit SENSE," Magnetic Resonance in Medicine, vol. 49, no. 1, pp. 144-150.
(104) Schlyer, D., P. Vaska, et al. (2006). Preliminary Studies of a Simultaneous PET/MRI Scanner Based on the RatCAP Small Animal Tomograph. Nuclear Science Symposium Conference Record, 2006. IEEE.
(105) Silva, A. C. and H. Merkle (2003). "Hardware considerations for functional magnetic resonance imaging." Concepts in Magnetic Resonance Part A 16A(1): 35-49.
(106) Tropp, J. (2002). "Dissipation, resistance, and rational impedance matching for TEM and birdcage resonators." Concepts in Magnetic Resonance 15(2): 177-188.
(107) Tuovinen, T., M. Berg, et al. (2012). Reactive near-field region radiation of planar UWB antennas close to a dispersive tissue model. Antennas and Propagation Conference (LAPC), 2012 Loughborough.
(108) van Bezooijen, A., R. Mahmoudi, et al. (2005). "Adaptive methods to preserve power amplifier linearity under antenna mismatch conditions." Circuits and Systems I: Regular Papers, IEEE Transactions on 52(10): 2101-2108.
(109) Vaughan, J. T., M. Garwood, et al. (2001). "7T vs. 4T: RF power, homogeneity, and signal-to-noise comparison in head images." Magn Reson Med 46(1): 24-30.
(110) Vaughan, J. T., D. N. Haupt, et al. (1995). "RF front end for a 4.1 Tesla clinical NMR spectrometer." Nuclear Science, IEEE Transactions on 42(4): 1333-1337.
(111) Vaughan, J. T., H. P. Hetherington, et al. (1994). "High frequency volume coils for clinical NMR imaging and spectroscopy." Magnetic Resonance in Medicine 32(2): 206-218.
(112) Yang, Q. X., J. Wang, et al. (2002). "Analysis of wave behavior in lossy dielectric samples at high field." Magn Reson Med 47(5): 982-989.